Asymmetric Complementary Interface for Enhanced Directional Adhesion

by

Zhen Yang

A thesis submitted in partial fulfillment of the requirements for the degree of

Master of Science

Department of Mechanical Engineering

University of Alberta

Abstract

Inspired by nature, structured interfaces have been shown to enhance adhesion by trapping crack propagation along the interface. To propagate the trapped crack, more energy input is required externally and therefore the effective fracture toughness is increased. In many applications, directional adhesion is desired where interface separation along different directions requires different fracture energy. One such example is climbing robot: it needs strong adhesion to stick their feet on vertical surfaces and weak adhesion to detach the feet while walking. In this work, we investigate a strategy to attain enhanced and directional adhesion using a complementary interface that contains an asymmetric pattern. In particular, the pattern consists of right triangles separated by flat regions. As the crack propagates from left to right, it travels upwards along the vertical side of the triangle, and then downwards along the hypotenuse; as it propagates from right to left, it travels upwards along the hypotenuse, and then downwards along the vertical side. Finite element analyses were performed in which the length of the crack tip was extended step by step and the energy release rate G was calculated at each crack length. The G values were compared to that of a flat interface to determine the adhesion enhancement. Our result shows that the fracture toughness of the interface is enhanced by approximately four times, compared with the flat control, for crack propagation from left to right, and the enhancement is larger for crack propagation in the opposite direction. In addition, parametric analyses reveal that the adhesion enhancements in the two opposite directions have differ-

ent sensitivities to the changes in the aspect ratio of the triangular pattern. The proposed strategy allows us to achieve enhanced and directional adhesion without modifying the interface chemistry. More importantly, different degree of adhesion asymmetry can be achieved by modulating the aspect ratio of the pattern on the interface, bearing great potential in applications where different levels of adhesion are desired for different purposes.

Contents

List of Tables

List of Figures

Chapter 1

Introduction

Adhesion plays significant roles in numerous fields. There are examples in our everyday lives from clothing such as Velcro[1] to office supplies such as Post-it notes[2], and examples in engineering across multi-scales such as robotics[3], soft electronics[4][5] and bio-mimetic systems[6][7]. Conventionally, pressure-sensitive adhesives (PSAs) [8] have been used to achieve strong adhesion via high viscous dissipation on the interface. On the other hand, PSAs exhibit several drawbacks such as low reversibility and sensitivity to surface roughness. Other types of adhesives available in the market, such as glue, require the modification of the surface chemistry which also exhibits low reversibility and toxicity. To overcome the drawbacks of conventional adhesives, numerous work has focused on the design of surface structure for reversible and enhanced adhesion. Examples include fibrillar surfaces([9]-[10]), micro patterned surfaces ([11][12]) and complementary micro patterned surfaces([13][14]), etc.

One way of introducing strong yet reversible adhesion is inspired from nature by gecko's feet. It was shown by Autumn *et al.*[15] that there are thousands of microscopic angled setae on a gecko's foot (e.g., Tokay gecko). The tip of each seta branches into hundreds of spatula terminals, leading to hierarchy fibrillar structures that conform to and form intimate contact with a wide range of surfaces regardless of their roughness. Relying primarily on van der Waals force, the adhesive strength on the gecko's feet can be as high as $10N/cm^2$ [16]. It is clear that the contact area between a fibrillar surface and a smooth substrate is less than that between two smooth substrates. The

adhesion between the fibrillar surface and the smooth substrate, however, can be enhanced due to several effects. Jagota *et al.*[17] showed that when a crack propagates on a fibrillar interface, the fibrils previously located ahead of the crack tip get unloaded and the strain energy stored in these fibrils is dissipated instead of being released back to the bulk. Later, Hui et al. [18] showed that a crack in a fibrillar structure is blunted when it reaches a fiber, and the concentrated stress field at the crack tip is redistributed into an equal load sharing zone over a characteristic length much larger than the diameter of the fiber. Therefore, the stress concentration at the crack tip is significantly reduced, hindering the crack propagation. Other effects can also contribute to the enhanced adhesion in fibrillar structures, such as the need to re-initiate the crack from fiber to fiber [19], and the effect of large surface-to-volume ratio [20].

Based on the above understanding, numerous bio-inspired fibrillar adhesives have been created and compared with unstructured surfaces. Sitti *et al.*[9] first utilized a pull-off test to measure the adhesion of an interface containing vertical fibrils with nanoscopic tip radius ($\sim$ 200 to 400nm). The achieved adhesive strength was shown similar to that measured from gecko. Later, Aksak *et al.*[10] proposed a theoretical model for adhesion induced by both angled and vertical fibrils, and performed indentation tests to measure the adhesion. The radius of the fibrils was varied from 20 to 30μm, and the height varied from 20 to 50μm. However, the adhesive strength measured from neither angled nor vertical fibrils could exceed that provided by unstructured surfaces. The discrepancy between the above two works was explained by Greiner *et al.* [21] in a systematic study on the effects of fiber diameter, aspect ratio and preload. Their work showed that the adhesion provided by polydimethylsiloxane (PDMS) fibrils is size-dependent, i.e., only the finest fibrils (5μm in radius and with a high aspect ratio, e.g., height to radius ratio $\geq$ 2) can exhibit adhesive strength higher than unstructured surface. As a supporting evidence, an array of multi-walled carbon nanotube with diameters in the range of 20 to 30nm was shown to exhibit remarkable adhesion similar to gecko's feet [22].

Many other studies investigated the effect of geometry on the adhesion of

fibrillar or similarly patterned interface. Lamblet *et al.* [11] utilized a peeling test to measure the adhesion of a micro-patterned PDMS-Acrylic adhesive interface. The PDMS substrate was patterned with micro pillars that had a radius of 1 μm, while the surface of the acrylic adhesive remains non-patterned. The height of pillars was systematically changed to obtain different aspect ratios. Their results showed that different aspect ratios could lead to different adhesion enhancements. With a relatively low aspect ratio (< 3), the patterned interface showed enhanced adhesion, and the adhesion enhancement increased with increasing aspect ratio in this range. With a relative large aspect ratio (>3), the patterned interface lost the ability to enhance adhesion because the long pillars tended to collapse with each other, which was detrimental to the formation of good contact between the two surfaces. Later, Poulard *et al.* [12] conducted a systematic study on the effects of diameter and spacing of the micro pillars. Their results showed that when the spacing of the pillars is larger than three times the pillar diameter, the adhesion increases linearly with increasing contact area (i.e., decreasing spacing and increasing pillar density). As the spacing decreases further to be lower than three times the pillar diameter, the adhesion enhancement slowly approaches a saturation region. Based on these studies, the adhesion enhancement on a patterned interface can be fine tuned by adjusting the geometry and density of the pillars.

Instead of modulating the size, aspect ratio and spacing of the patterns on the interface, some studies have focused on the geometry of the fiber tip. Campo *et al.* [23] conducted a systematic study on different PDMS fiber tip geometries including flat, sphere, mushroom and spatula. The mushroom tip showed extraordinary adhesive strength, which is much larger than that of an unstructured surface (e.g., about 30 times higher for the mushroom tip with radius of $10\mu m$). Besides the mushroom tip, Glassmaker *et al.* [24] discovered that vertical fibrils with a thin layer of film connecting them can also lead to enhanced adhesion. They referred to this phenomenon as the crack-trapping effect: the periodic micro structure near the interface results in reduction in the energy release rate G available for crack propagation; for G to reach the intrinsic work of adhesion, more energy is required externally and hence the

apparent adhesion is enhanced.

While the above works investigated the adhesion between a structured/ patterned surface and a smooth surface, there have also been studies where the surface modification was done on both sides of the interface, e.g., complementary surfaces. One inherent advantage associated with such an interface is that the adhesion is highly selective: only when the upper and lower surfaces have complementary patterns and are well aligned can enhanced adhesion be achieved during the separation. Vajpayee *et al.* [13] conducted experiments to measure the adhesion between two PDMS sheets that contain complementary rippled structures described by a sinusoidal function. During the experiments, the two sheets are first pushed together and then separated by inserting a wedge into the interface. A separate finite element(FE) model with the same dimensions as the actual sample was created to evaluate the energy release rate at the crack tip as it propagates through the interface. The FE model is subject to a uniform displacement along the top edge to mimic a mode I loading. The FE results indicated that the energy release rate is reduced when the crack propagates in directions other than the horizontal, and is periodically undulated with the apparent crack tip location. The ratio between the local minima of the energy release rate ($G_{pattern}$) and those in a flat control at the same apparent crack tip location (G_{flat}) is calculated. The adhesion enhancement in the rippled interface was assessed by the inverse of this ratio. The adhesion is enhanced due to the same crack trapping mechanism as mentioned in Glassmaker *et al.* [24], and was shown to increase with increasing amplitude of the ripple. Later, Singh *et al.*[14] investigated the adhesion in a PDMS interface with complementary pillars and channels. Similar to the study of the rippled interface [13], a FE model was created to evaluate the energy release rate at the crack tip, when the sample was subjected to a uniform displacement on the top. The FE results showed that the adhesion enhancement for the pillar/channel interface is approximately 5 times and is independent of the pillar height.

In many engineering applications, directional adhesion is desired where interface separation along different directions requires different fracture energy.

One such example is climbing robot (*stickybot*[3]), which needs strong adhesion to stick their feet on vertical surfaces and weak adhesion to detach the feet while walking. The directional adhesion in *stickybot* was enabled by the angled polymer fibrils on its feet pad: when loaded against the preferred direction, the structure exhibits friction with no adhesion; when loaded in the preferred direction, the structure exhibits adhesion in both normal and shear directions. The angled fibrillar structure can also be integrated with different tip geometries to modulate the degree of directional adhesion. For example, Murphy *et al.* [25] implemented the idea of mushroom tip by attaching them to the end of angled fibrils. The shear strength was found to be $\sim 10N/cm^2$ in the preferred direction but only $\sim 2N/cm^2$ opposite to the preferred direction.

While angled fibrils can produce directional adhesion, they do reduce the contact area as well as create some cavities in the bulk material near the interface, which is not desirable for some applications. Furthermore, there are other issues related to fibrils such as the collapse and adhesion between them, which weaken interface adhesion. In this thesis, we explore another strategy to induce enhanced and directional adhesion, motivated by the adhesion enhanced by complementary patterned interface. In the works by Vajpayee *et al.* [13] and Singh *et al.* [14], no directional adhesion is expected as the interface patterns used are symmetric, i.e., there is no difference for the crack to propagate from the two opposite directions. In this work, the above symmetric interface patterns are replaced by asymmetric triangles separated by flat regions, which are expected to lead to different adhesion enhancements along different separation directions.

The structure of the thesis is as follows. Fundamentals of fracture mechanics and details about the FE modelling are presented in Chapters 2 and 3, respectively. In Chapter 4, FE results for symmetric complementary interface under several loading conditions are discussed. This chapter demonstrates how different loading conditions influence the adhesion enhancement. It also serves as a model validation by comparing our results with existing data. In Chapter 5, the results for asymmetric complementary interface under several loading conditions are presented and discussed, to investigate directional adhe-

sion. The influences of geometrical parameters of the interface on the adhesion enhancement are discussed in Chapter 6. Finally, conclusions and future work are given in Chapter 7.

Chapter 2

Fundamentals

2.1 Linear Elastic Fracture Mechanics

2.1.1 Stress At Crack Tip

Consider a crack embedded in an isotropic linear elastic material, shown in Figure 2.1. A polar coordinate system is defined with its origin at the crack tip. The stress field ahead of the crack tip is given by [26]:

$$\sigma_{ij} = (\frac{k}{\sqrt{r}}) f_{ij}(\theta) + \sum_{m=0}^{\infty} A_m r^{\frac{m}{2}} g_{ij,m}(\theta) \tag{2.1}$$

where

σ_{ij} = stress tensor
k = constant
f_{ij} = dimensionless functions of θ in the leading term
A_m = the amplitude of the m^{th}-order term
$g_{ij,m}$ = dimensionless functions of θ for the m^{th}-order term.

As r approaches zero, the leading term approaches infinity while the higher-order terms remain finite or approach zero. Thus Eqn.(2.1) predicts that the stress field at the crack tip is singular.

2.1.2 Stress Intensity Factor

Figure 2.2 shows the three types of loading conditions that a crack can experience and they are named by Mode I, Mode II and Mode III, respectively. Mode I loading refers to the applied loading normal to the crack surface, tending to open the crack; Mode II loading refers to in-plane shear, tending to slide one

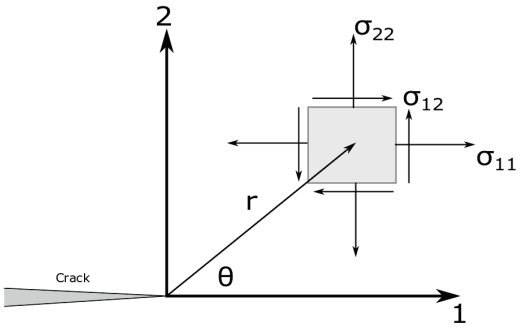

Figure 2.1: A polar coordinate system with its origin at the crack tip in an isotropic linear elastic material

crack face relative to the other; Mode III refers to out-of-plane shear. In each Mode there is a presence of $\frac{1}{\sqrt{r}}$ stress singularity at the crack tip. The proportionality constant k and dimensionless function f_{ij} depend on the Mode. Thus k is replaced by *stress intensity factor* K which is defined by $K = k\sqrt{2\pi}$. Subscripts I, II and III are used to denote the Mode of loading, i.e. K_I, K_{II}, K_{III}. Planar cracks, such as the ones to be considered in this work, are subject to Mode I and/or Mode II loadings only. The stress field ahead of the crack tip in an isotropic linear elastic material for Modes I and II can be expressed as:

$$\begin{aligned} \lim_{r\to 0} \sigma_{ij}^{I} &= \frac{K_I}{\sqrt{2\pi r}} f_{ij}^{I}(\theta) \\ \lim_{r\to 0} \sigma_{ij}^{II} &= \frac{K_{II}}{\sqrt{2\pi r}} f_{ij}^{II}(\theta) \end{aligned} \tag{2.2}$$

Complete expressions of stress field in proximity of the crack tip due to Mode I and II loadings are given in Table 2.1. K is considered as an important parameter in linear elastic fracture mechanics because given K, strain, stress and displacement fields near the crack tip can be completely determined. To compute K, one must relate it to the remotely applied loading and the crack geometry. Closed-form solutions exsit for some simple configurations, one of which is a finite-length through-thickness crack in an infinite body subject to axial tensile stress, shown in Figure 2.3. Because the applied loading is normal to the crack surface, the loading is pure Mode I. K in this case is given by:

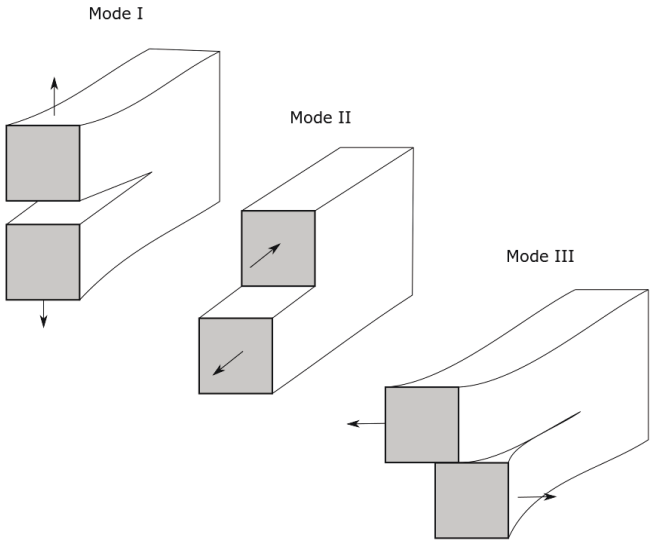

Figure 2.2: The three modes of loading

$$K_I = \sigma\sqrt{\pi a} \tag{2.3}$$

If instead, a remote shear stress τ is applied, the loading is pure Mode II and K is given by:

$$K_{II} = \tau\sqrt{\pi a} \tag{2.4}$$

If the same crack is now oriented with an angle β from the loading direction, as shown in Figure 2.4, the crack tip experiences mixed Mode loading and both K_I and K_{II} will be present. By redefining a coordinate system that conforms with the tilted crack face, one can resolve the applied loading into the normal and shear components, i.e. $\sigma_{2'2'}$ and $\tau_{1'2'}$, which contribute to Mode I and Mode II stress intensity factors, respectively. $\sigma_{1'1'}$ does not contribute to the stress intensity factors. $\sigma_{2'2'}$ and $\tau_{1'2'}$ can be related to σ and β using stress transformation. Then Mode I and Mode II stress intensity factors in Figure 2.4(a) can be expressed as:

$$K_I = \sigma_{2'2'}\sqrt{\pi a} = \sigma\cos^2(\beta)\sqrt{\pi a} \tag{2.5}$$

and

$$K_{II} = \tau_{1'2'}\sqrt{\pi a} = \sigma\sin(\beta)\cos(\beta)\sqrt{\pi a} \tag{2.6}$$

Table 2.1: Stress fields near the crack tip for Mode I and Mode II loading in an isotropic linear elastic material. [26]

	Mode I	Mode II
σ_{11}	$\frac{K_I}{\sqrt{2\pi r}} \cos\frac{\theta}{2}[1 - \sin\frac{\theta}{2}\sin\frac{3\theta}{2}]$	$\frac{K_{II}}{\sqrt{2\pi r}} \sin\frac{\theta}{2}[2 + \cos\frac{\theta}{2}\cos\frac{3\theta}{2}]$
σ_{22}	$\frac{K_I}{\sqrt{2\pi r}} \cos\frac{\theta}{2}[1 + \sin\frac{\theta}{2}\sin\frac{3\theta}{2}]$	$\frac{K_{II}}{\sqrt{2\pi r}} \sin\frac{\theta}{2}\cos\frac{\theta}{2}\cos\frac{3\theta}{2}$
τ_{12}	$\frac{K_I}{\sqrt{2\pi r}} \cos\frac{\theta}{2}\sin\frac{\theta}{2}\cos\frac{3\theta}{2}$	$\frac{K_{II}}{\sqrt{2\pi r}} \cos\frac{\theta}{2}[1 - \sin\frac{\theta}{2}\sin\frac{3\theta}{2}]$
σ_{33}	0 for plane stress $\nu(\sigma_{11} + \sigma_{22})$ for plane strain	0 for plane stress $\nu(\sigma_{11} + \sigma_{22})$ for plane strain
τ_{13}, τ_{23}	0	0

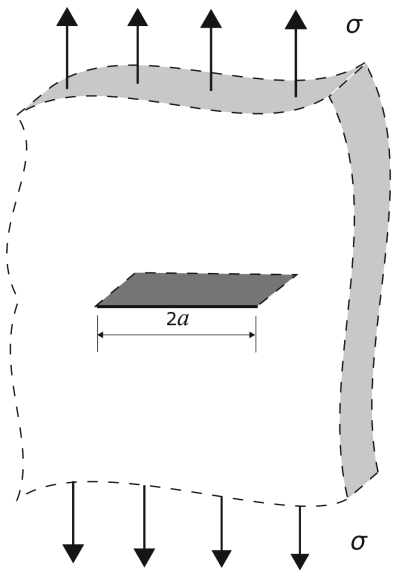

Figure 2.3: A finite-length through-thickness crack subject to uniaxial tensile loading

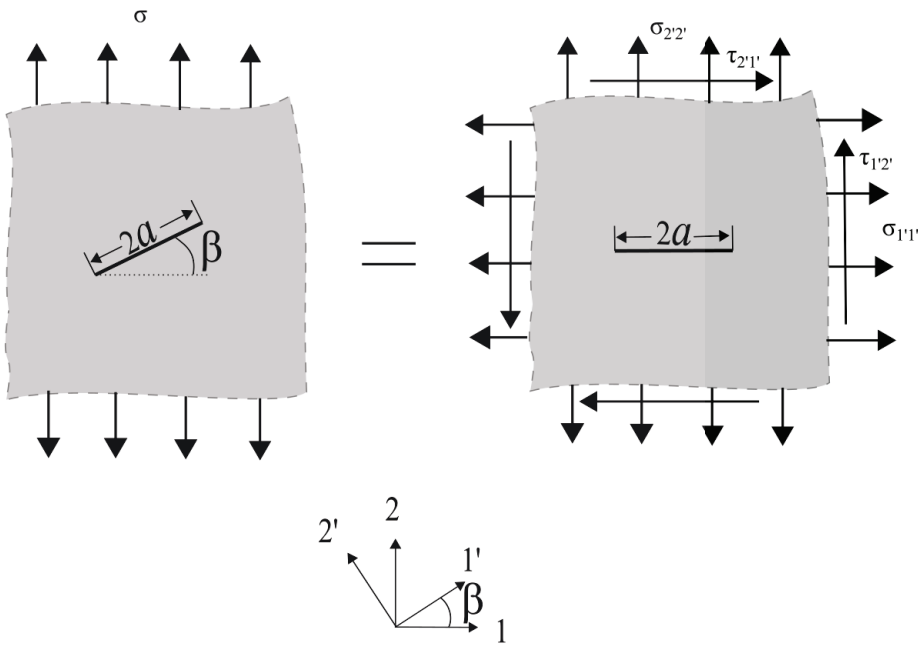

Figure 2.4: A through-thickness crack under mixed Mode loading

2.1.3 Griffith Energy Balance and Energy Release Rate

Griffith [27] applied the concept of the first law of thermodynamics to cracks and defined a critical condition for the crack to grow under equilibrium:

$$\frac{d\Lambda}{dA} = \frac{d\Pi}{dA} + \frac{dW_s}{dA} = 0 \tag{2.7}$$

where:

Λ = total energy
Π = potential energy of the elastic body
W_s = surface energy
dA = an incremental increase of the crack surface area

Therefore, during a quasi-static incremental growth dA of an edge crack, the energy required to create new surfaces is equal to the decrease in the total potential energy of the body (i.e., energy available for the crack growth):

$$-\frac{d\Pi}{dA} = \frac{dW_s}{dA} \tag{2.8}$$

The left hand side term in Eqn.(2.8) is often referred to as energy release rate G, so that:

$$G = -\frac{d\Pi}{dA} = -\frac{d\Pi}{bda} \tag{2.9}$$

where

b = the out-of-plane thickness
da = an incremental increase of the crack length in the plane

In the case where a displacement control boundary condition is applied, the potential energy is equal to the strain energy U, and Eqn.(2.9) can be reduced to:

$$G = -\frac{dU}{bda} \tag{2.10}$$

2.1.4 Relation Between G and K

For a planar crack subject to Mode I loading, such as shown in Figure 2.3, the two quantities G and K_I are related by [26]:

$$G = \frac{K_I^2}{E'} \tag{2.11}$$

where

$E' = E$ for plane stress
$E' = \frac{E}{1-\nu^2}$ for plane strain

E and ν being the Young's modulus and Poisson's ratio of the material, respectively. When Mode I and Mode II are both present, the energy release rate is given by [26]:

$$G = \frac{K_I^2}{E'} + \frac{K_{II}^2}{E'} \tag{2.12}$$

2.1.5 Crack Propagation Criterion

Two commonly-used criteria for crack propagation are the energy release rate criterion and stress intensity factor criterion. The energy release rate criterion states that when G reaches a critical energy release rate G_c, or an equalvalent quantity called the intrinsic work of adhesion W_{ad}, the crack starts propagating. The condition for a crack to grow in a quasi-static manner is given by:

$$\begin{aligned} G &= W_{ad} \\ \frac{dG}{da} &= 0 \end{aligned} \tag{2.13}$$

The stress intensity factor criterion states that when K reaches a critical stress intensity factor K_c, i.e. $K = K_c$ the crack starts propagating. Both G_c and K_c

are measures of the material's fracture toughness. Other crack propagation criteria are available, such as the crack opening displacement criterion, but they are not discussed here.

2.2 Crack Growth in a Double Cantilever Beam

Consider a double-cantilever-beam (DCB) specimen subject to a fixed displacement boundary condition δ, shown in Figure 2.5. The energy release rate in this case can be evaluated in closed form. The DCB specimen has a thickness of $2h$ and out-of-plane thickness of b. Consider a cross section in one of the beams locate at x, with x being the distance from the crack tip to the cross section. The bending moment M and area moment of inertia I of the cross section are given by:

$$M = (a - x)w \tag{2.14}$$

$$I = \frac{bh^3}{12} \tag{2.15}$$

where w is the force at the end of the DCB to cause deflection δ. The stress and strain in an infinitesimal element on the cross section are given by:

$$\sigma = \frac{My}{I} \tag{2.16}$$

$$\epsilon = \frac{My}{EI} \tag{2.17}$$

where

$y =$ the distance from the element to the neutral axis of the beam

The strain energy of the DCB is given by:

$$U = 2 \int \frac{1}{2} \sigma \epsilon dV \tag{2.18}$$

where the factor of 2 accounts for the two identical beams in the DCB. Sub-

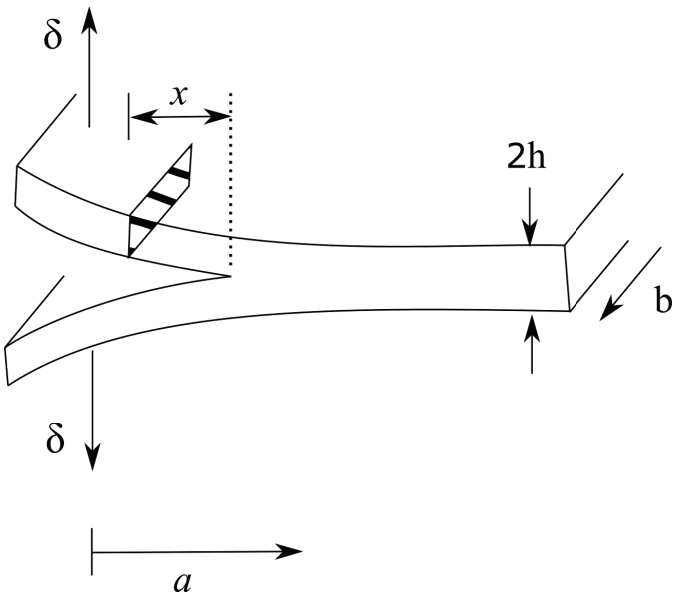

Figure 2.5: A crack in a double cantiliver beam subject to fixed displacement at one end

stituting the expressions of σ and ϵ into Eqn.(2.18), U can be written as:

$$\begin{aligned} U &= 2\int \frac{1}{2}\frac{w^2(a-x)^2y^2}{\frac{E}{144}b^2h^6}dV \\ &= \frac{144}{E}\int_0^a \int_{\frac{-h}{2}}^{\frac{h}{2}} \frac{w^2(a-x)^2y^2}{b^2h^6}dydx(b) \\ &= \frac{12}{Eb}\int_0^a \frac{w^2(a-x)^2}{h^6}h^3dx \\ &= \frac{4w^2a^3}{Ebh^3} \end{aligned} \tag{2.19}$$

Force w can be written in terms of δ by:

$$w = \frac{\delta Ebh^3}{4a^3} \tag{2.20}$$

Substituting Eqn.(2.20) into Eqn.(2.19), U can be written as:

$$U = \frac{4a^3}{Ebh^3}\frac{\delta^2E^2b^2h^6}{16a^6} = \frac{\delta^2Eh^3b}{4a^3} \tag{2.21}$$

Then the strain energy release rate G is given by:

$$G = -\frac{\partial U}{\partial A} = -\frac{\partial U}{b\partial a} = \frac{3}{4}\frac{\delta^2Eh^3}{a^4} \tag{2.22}$$

Eqn.(2.22) is an analytical expression for G in a DCB under Mode I loading, and will be used for Model validation in section 3.3.

2.3 Kinked Crack Tip under In-Plane Loading

When the propgation of a crack embbeded in an infinite body suddenly changes direction, a kink is formed. The study of the kink can help us understand crack propagation on a patterned interface. Figure 2.6 shows an infinitesimal kink at the tip of a horizontal crack in an infinite body. The kink has an angle of α with the main crack surface. The stress intensity factors at the kinked crack tip under combined in-plane loadings are given by [26]:

$$\begin{aligned} K_I(\alpha) &= C_{11}K_{I,n} + C_{12}K_{II,n} \\ K_{II}(\alpha) &= C_{21}K_{I,n} + C_{22}K_{II,n} \end{aligned} \tag{2.23}$$

where

$K_{I,n}$ = nominal Mode I stress intensity factor on the main crack surface
$K_{II,n}$ = nominal Mode II stress intensity factors on the main crack surface

and

$$\begin{aligned} C_{11} &= \frac{3}{4}\cos(\frac{\alpha}{2}) + \frac{1}{4}\cos(\frac{3\alpha}{2}) \\ C_{12} &= -\frac{3}{4}[\sin(\frac{\alpha}{2}) + \sin(\frac{3\alpha}{2})] \\ C_{21} &= \frac{1}{4}[\sin(\frac{\alpha}{2}) + \sin(\frac{3\alpha}{2})] \\ C_{22} &= \frac{1}{4}\cos(\frac{\alpha}{2}) + \frac{3}{4}\cos(\frac{3\alpha}{2}) \end{aligned}$$

Using Eqn.(2.12), the strain energy release rate at the kinked crack tip can be expressed as:

$$G_{kink} = \frac{K_I^2(\alpha) + K_{II}^2(\alpha)}{E'} \tag{2.24}$$

In the special case where only Mode I loading is applied, $K_{II,n} = 0$. Therefore:

$$\begin{aligned} K_I(\alpha) = C_{11}K_{I,n} &= [\frac{3}{4}\cos(\frac{\alpha}{2}) + \frac{1}{4}\cos(\frac{3\alpha}{2})]K_{I,n} = \cos^3(\frac{\alpha}{2})K_{I,n} \\ K_{II}(\alpha) = C_{21}K_{I,n} &= [\frac{1}{4}[\sin(\frac{\alpha}{2}) + \sin(\frac{3\alpha}{2})]K_{I,n} = \sin(\frac{\alpha}{2})\cos^2(\frac{\alpha}{2})K_{I,n} \end{aligned} \tag{2.25}$$

Substituting Eqn.(2.25) into Eqn.(2.24), the total energy release rate at the kinked crack tip is given by:

$$\begin{aligned} G_{kink} &= \frac{K_I^2(\alpha) + K_{II}^2(\alpha)}{E'} \\ &= \frac{K_{I,n}^2}{E'}[\cos^6(\frac{\alpha}{2}) + \sin^2(\frac{\alpha}{2})\cos^4(\frac{\alpha}{2})] \\ &= \frac{K_{I,n}^2}{E'}\cos^4(\frac{\alpha}{2}) \end{aligned} \tag{2.26}$$

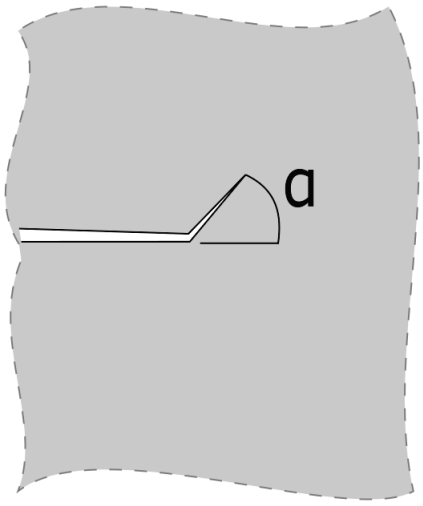

Figure 2.6: An infinitesimal kink at a crack tip in an infinite body.

2.4 Mechanism of Crack Trapping on Patterned Interface

It has been shown that pattened interfaces are able to enhance the interfacial adhesion by trapping the cracks [24]. This section explains the mechanism of crack trapping on patterned interfaces. Figure 2.7(a) shows the schematic of a sinusoidal-curved interface with an initial crack in an infinite body. The maximum angle between the interface and the horizontal is 45°. Figure 2.7(b) shows a flat interface with an initial crack in an infinite body which serves as a control. In both cases, the sample is subjected to uniaxial loading in y-direction. We will compare the energy release rate G for the crack propagation along these two interfaces to discuss the fundamental mechanism by which adhesion may be enhanced on patterned interface.

Given a crack tip location on the patterned interface, an analogy can be drawn to the kinked crack shown in Figure 2.6 if we assume the patterned surface before the crack tip is flat. This is a strong approximation, but allows us to qualitatively assess the change in G caused by the pattern. Considering $G_{pattern} = G_{kink}$ and using Eqn.(2.11) to relate $\frac{K_I^2}{E'}$ to the energy release rate at

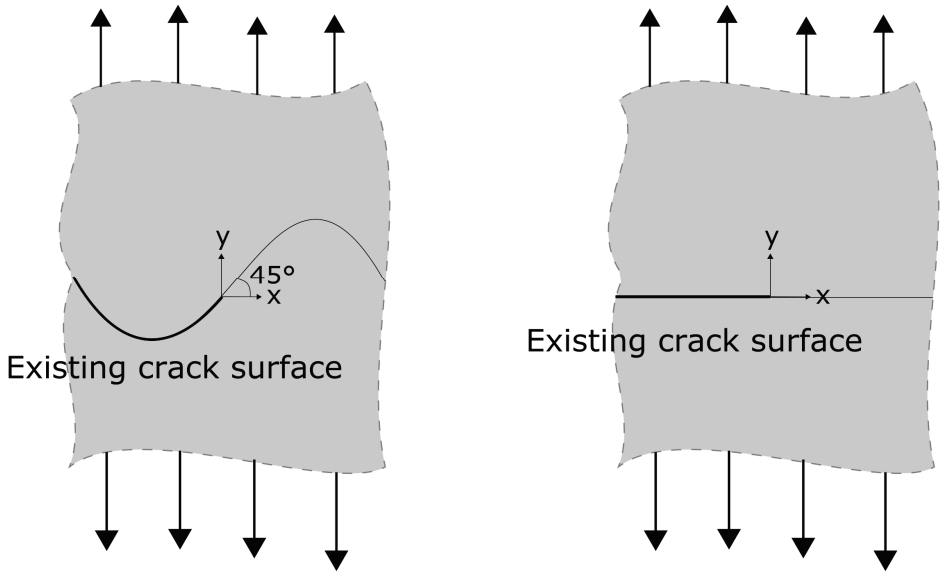

(a) (b)

Figure 2.7: (a): a sinusoidal-curved interface with an initial crack. (b): a flat interface with an initial crack.

the crack tip on a flat interface, i.e. $G_{flat} = \frac{K_I^2}{E'}$, Eqn.(2.26) can be expressed as:

$$G_{pattern} = G_{flat} \cos^4(\frac{\alpha}{2}) \tag{2.27}$$

where α is the tangential angle at a point along the patterned interface. Then the ratio of $G_{pattern}$ to G_{flat} is given by:

$$R \equiv \frac{G_{pattern}}{G_{flat}} = \cos^4(\frac{\alpha}{2}) \tag{2.28}$$

Figure 2.8(a) shows the shape of the interface described by the sinusoidal function: $\frac{y}{y_{max}} = \sin(\frac{x}{L})$, where L is the wave length, and y_{max} is the peak height in the pattern. Figure 2.8(b) shows the tangential angle α of the sinusoidal interface. Figure 2.8(c) shows how R changes as the crack tip moves along the sinusoidal-curved interface. As can be seen, R varies periodically with the tangential angle α. The local maxima of R are equal to 1 and take

place where α is zero, i.e. at the peaks and bottoms of the sinusoidal interface. The local minima of R can be determined using Eqn.(2.28):

$$R_{min} = \cos^4(\frac{\alpha_{max}}{2}) = \cos^4(\frac{45^\circ}{2}) = 0.729$$

For the crack to grow on the patterned surface, $G_{pattern}$ needs to be at least W_{ad}. As examples, the three horizontal lines in Figure 2.8(c) correspond to three cases where $W_{ad} = \frac{1}{2}G_{flat}$, $\frac{9}{10}G_{flat}$ and G_{flat}, respectively. In the case where $W_{ad} = 0.5G_{flat}$, the corresponding horizontal line is entirely below the R curve, i.e., $G_{pattern} > W_{ad}$, indicating the crack on the patterned interface is able to propagate without getting trapped. In the case where $W_{ad} = G_{flat}$, the horizontal line is above the R curve, i.e. $G_{pattern} < W_{ad}$, indicating the crack on the patterned interface is entirely trapped. If the horizontal line intersects with the R curve, e.g. when $W_{ad} = 0.9G_{flat}$, the crack will get trapped where the R curve is below the horizontal line. Thus if the line corresponding to W_{ad}/G_{flat} just passes the local minima of the R curve, i.e. $W_{ad} = 0.729G_{flat}$, the crack is just able to propagate through the entire patterned interface.

The above arguments imply that under the same loading condition as a flat interface, the patterned interface leads to reduction in G and trapping of the crack. In order to propagate the crack on the patterned interface, the external load will need to be increased for $G_{pattern}$ to reach W_{ad}. At this point it is convenient to introduce the adhesion enhancement factor which is defined as the maximum ratio between G_{flat} and $G_{pattern}$:

$$F = (\frac{G_{flat}}{G_{pattern}})_{max} = \frac{1}{R_{min}} \tag{2.29}$$

For the specific pattern considered here:

$$F = \frac{1}{\cos(\frac{\alpha_{max}}{2})^4} = \frac{1}{0.729} = 1.373 \tag{2.30}$$

F is a measure of the adhesion enhancement in the patterned interface as compared to the flat control. However, it needs to be mentioned that Eqn.(2.30) is an approximation to the case where the crack is embedded in an infinite body under Mode I loading, and the surface behind the crack tip is horizontal. In

the case where the crack is embedded in a finite body with combined loadings and a complex geometry, the problem needs to be handled numerically, e.g., by Finite Element Analysis(FEA).

To give an example, two separate FE models are created for the patterned and flat interfaces in Figure 2.7 with the same overall dimensions, and the material is Aluminum with young's modulus being $69000MPa$. The crack tip on the patterned interface is at the inflection point where the tangential angle is 45°. The corresponding crack tip on the flat interface is at the same apparent length as that on the patterned interface. A small kink is present at the crack tip with the kink angle being 45°. Both models are subjected to the same externally applied Mode I loading and the stress distributions near the crack tips are shown in Figure 2.9. As can be seen, differences in all stress distributions can be observed between the flat and patterned interface models.

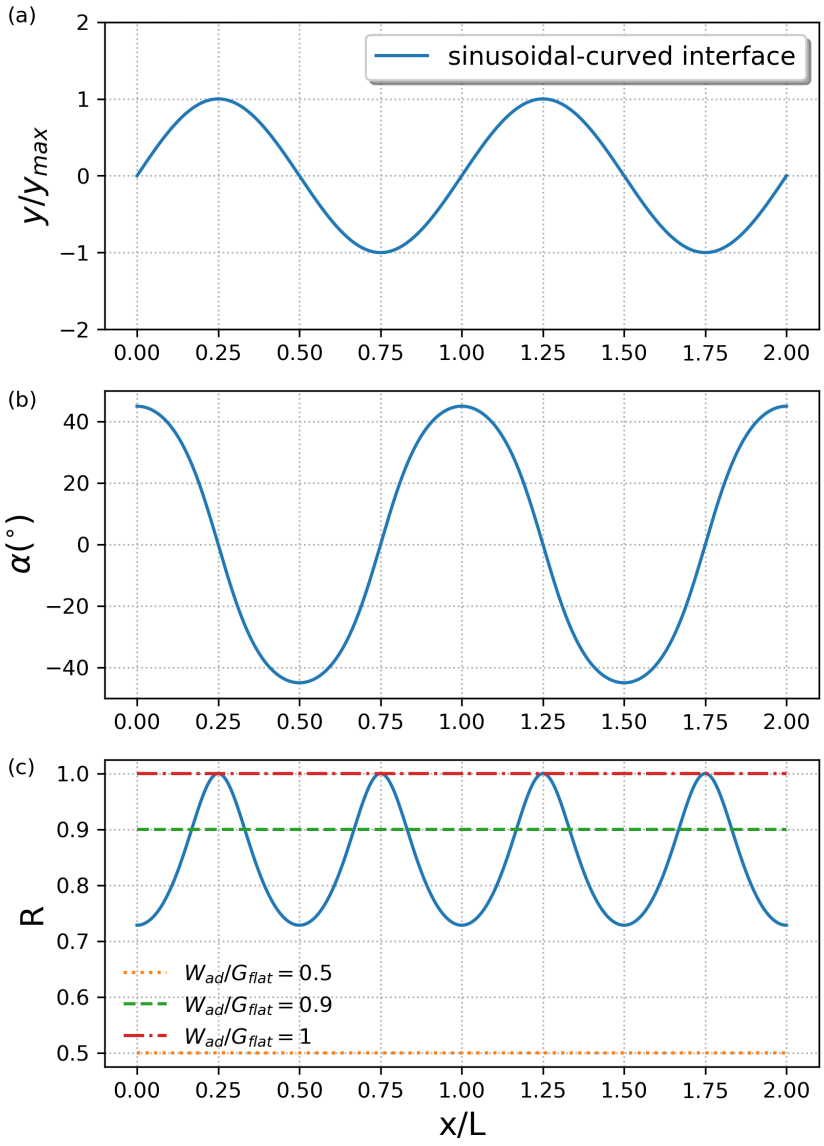

Figure 2.8: (a) the shape of an interface described by $y/y_{max} = \sin(x/L)$. (b) the tangential angle of the interface. (c) R versus x/L and several horizontal lines corresponding to different W_{ad}/G_{flat} values.

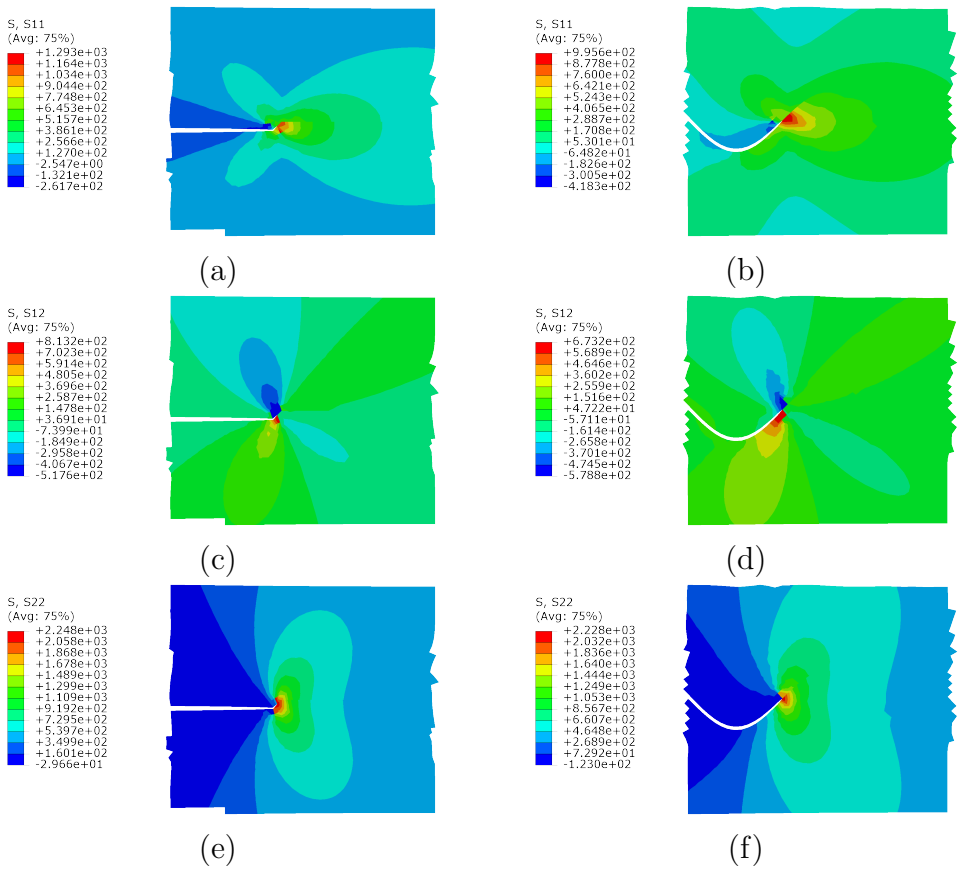

Figure 2.9: The stress distributions near the kink on the flat interface and the crack tip on the patterned interface when subjected to the same externally applied Mode I loading, left panel: flat interface with the small kink; right panel: patterned interface.

Chapter 3

Finite Element Models

3.1 Simulated Systems

Three types of pattern are investigated, which are rectangular, rippled and triangular, shown in Figure 3.1(a)(b)(c), respectively. In each patterned interface model, energy release rate G is evaluated as the crack propagates, and compared to that from a flat control, shown in Figure 3.1(d). Commercial package ABAQUS was utilized for the FEA.

Among the three patterned interface models shown in Figure 3.1(a)(b)(c), the rectangular and rippled models will be referred to as symmetric patterns and the triangular model will be referred to as asymmetric patterns. For the symmetric patterns, crack propagation from left to right is the same as propagation from right to left. Whereas such symmetry is lost in the triangular pattern in Figure 3.1(c), which can potentially lead to directional adhesion. The symmetric patterns are used to investigate the enhanced adhesion in patterned interfaces compared to flat interfaces. Besides, they also serve as model validation, as the results will be compared with those from the literature [13][14]. The asymmetric patterns are used to investigate whether the adhesion enhancement is different via different crack propagation directions and the sensitivity of the results to geometry and loading conditions.

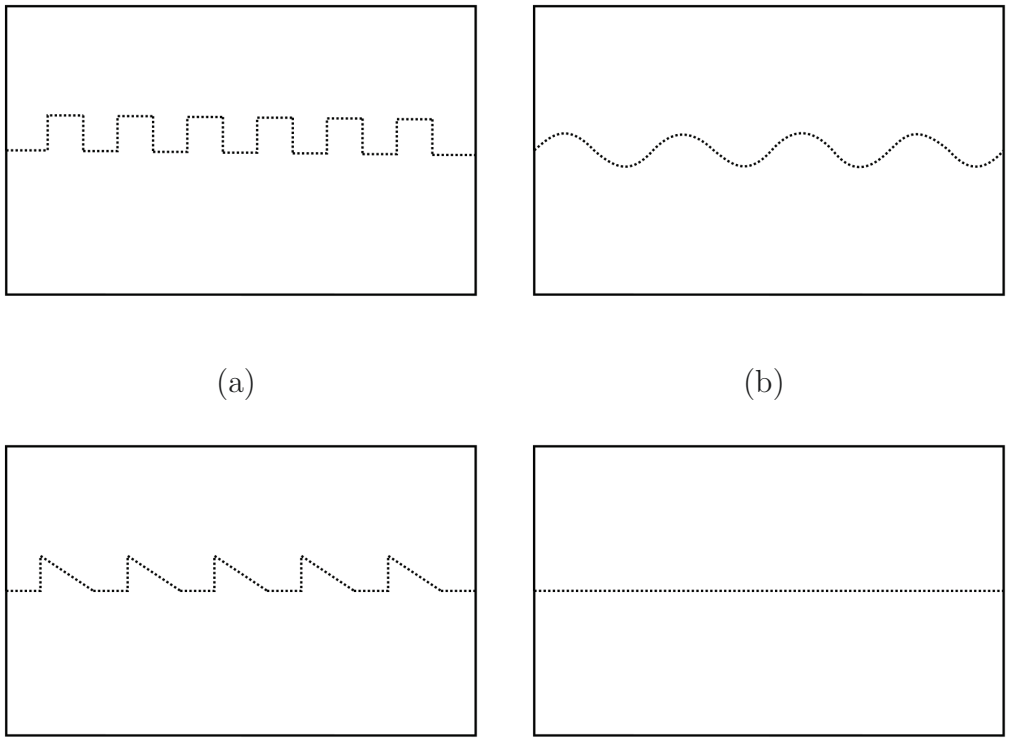

Figure 3.1: The schematics of (a) rectangular interface model (b) rippled interface model (c) triangular interface model and (d) flat control.

3.2 Simulation Details

3.2.1 Units in ABAQUS

In ABAQUS, users do not need to specify the units, so it is important to keep the units consistent. In our FE models, the units for length and modulus are μm and MPa, respectively. Using a dimensional analysis, the unit for strain energy release rate G is given by:

$$\frac{energy}{area} = \frac{force * length}{area} = \frac{MPa * \mu m^2 * \mu m}{\mu m^2} = \frac{N}{m} = \frac{J}{m^2} \tag{3.1}$$

3.2.2 Material Properties

In the FE models, the material used is polydimethylsiloxane(PDMS), modeled as an incompressible Neo-Hookean hyperelastic material. This material was

chosen becasue it is widely used in adhesion testing as well as in fabrication of patterned interfaces due to its low surface energy and weak chemical reactivity. The strain energy density for Neo-Hookean material is given by:

$$U = C_{10}(I_1 - 3) + \frac{1}{D_1}(J^{el} - 1)^2 \tag{3.2}$$

where

I_1 = the first deviatoric strain invariant = $\lambda_1^2 + \lambda_2^2 + \lambda_3^2$
J^{el} = the elastic volume ratio

λ_1, λ_2 and λ_3 being the principle strethces. The value of coefficient C_{10} is obtained from an experimental work that measured the mechanical properties of PDMS [28] $C_{10} = 0.0705MPa$. For incompressible materials, $J^{el} = 1$ such that the second term in Eqn.(3.2) vanishes and the strain energy density is given by:

$$U = C_{10}(I_1 - 3)$$

In ABAQUS, the elimination of the second term in Eqn.(3.2) is triggered by setting $D_1 = 0$.

3.2.3 Mesh and Element

Quad-dominated mesh scheme and 4-node bilinear plane stress elements with reduced integration(CPS4R) are applied to the models. The two sides of the interfaces (upper and lower surfaces) contains the same number of nodes and they are all equally spaced, as shown in Figure 3.2.

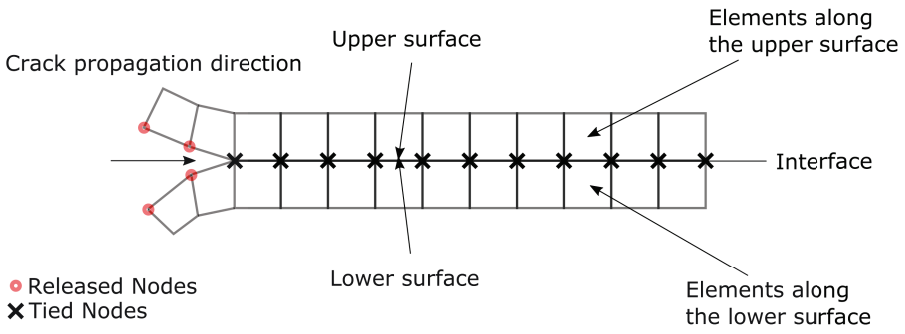

Figure 3.2: The schematic of elements along an interface.

3.2.4 Contact and Boundray Conditions

Each model consists of one upper part (above the interface) and one lower part (below the interface). The upper and lower surfaces are defined as master and slave surfaces, and they form frictionless and hard contact pairs with the penalty constraint enforcement method [29]. Penalty method allows small degree of penetration between the contact pairs, thus it makes the problem easier to converge as well as reduces the number of iterations for the analysis. As mentioned earlier, the upper and lower surfaces contain the same number of nodes. All the paired nodes along the interface are initially tied via the MPC (multi points constraint) user subroutine implemented in ABAQUS, which eliminates all degrees of freedom of the nodes on the slave surface relative to those on the master surface. In the numerical analysis, the paired nodes are released from the constraint step by step, by controlling the parameter LMPC in MPC. In this fashion, the length of the crack is extended in the direction along which the tied nodes are released to mimic a crack propagation, as Figure 3.2 illustrates. A complete code block of MPC user subroutine is written in Fortran 99 and given in Appendix A.

For a 2D problem in ABAQUS, U and UR represent displacement and rotation respectively, followed by numbers $1, 2$ and 3 to denote the direction along which the displacement or rotation takes place, e.g. $U1$ and $UR3$ represent displacement in direction 1 and rotation about axis 3, respectively. In this work, there are three types of loading and associated boundary conditions that the models can be subject to, shown in Figure 3.3. In the first case(Figure 3.3(a)), hereafter referred to as the pulling condition, the top boundary is subject to a uniform displacement δ while the bottom edge is subjected to "frictionless" boundary conditions where all the nodes are constrained by $U2 = UR3 = 0$. In addition, the first node (marked by ▲ in Figure 3.3(a)) is completely constrained, i.e. $U1 = U2 = U3 = UR3 = 0$, to remove any rigid body motion. In the second case(Figure 3.3(b)), hereafter referred to as the symmetric peeling condition, the first few nodes on the top and bottom edges are subject to displacement δ. In the third case (Figure 3.3(c)), referred to as the asymmet-

ric peeling condition, the first few nodes on the top boundary is subject to displacement δ and the bottom edge is constrained by "frictionless" boundary condition. Similar to Figure 3.3(a), in Figures 3.3(b) and (c) one node is completely constrained to remove rigid body motion, which is marked by ▲.

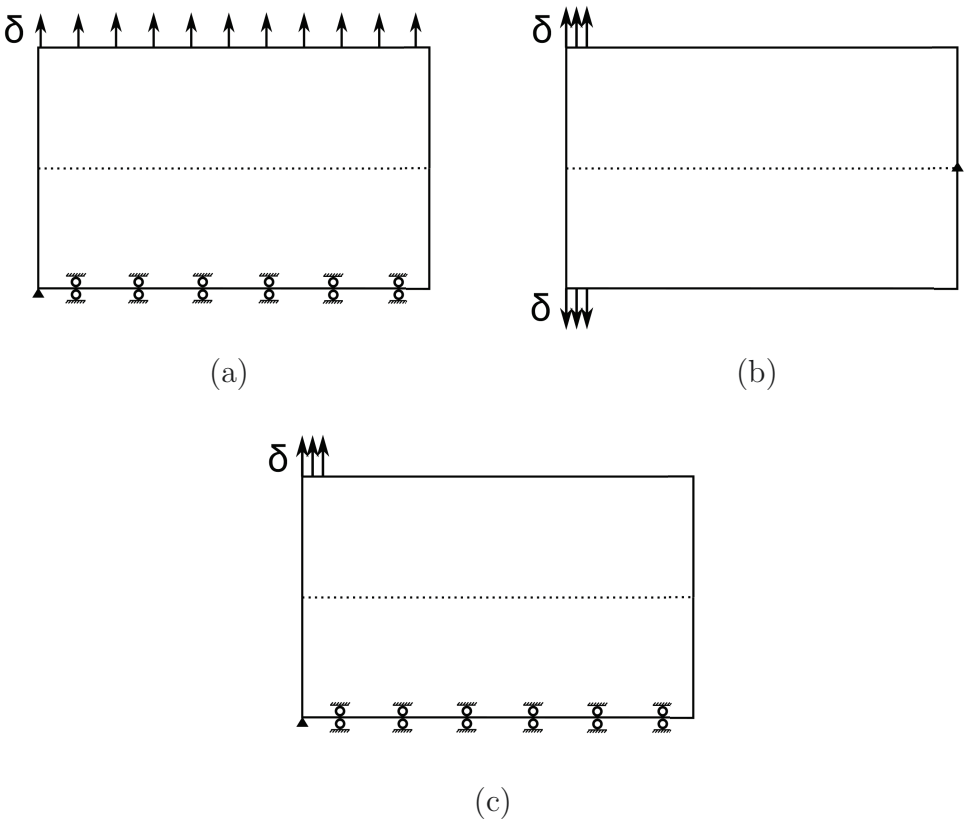

Figure 3.3: The three types of loading and boundary conditions that can be applied to the FE models: (a) pulling, (b) symmetric peeling and (c) asymmetric peeling.

Figure 3.4 shows how the displacement δ changes with numerical step n. As can be seen, from 0 to n_0, δ increases linearly from 0 to δ_0 during which all the paired nodes along the interface are still tied by MPC. After $n = n_0$, δ becomes constant and the tied nodes start being released from MPC step by step.

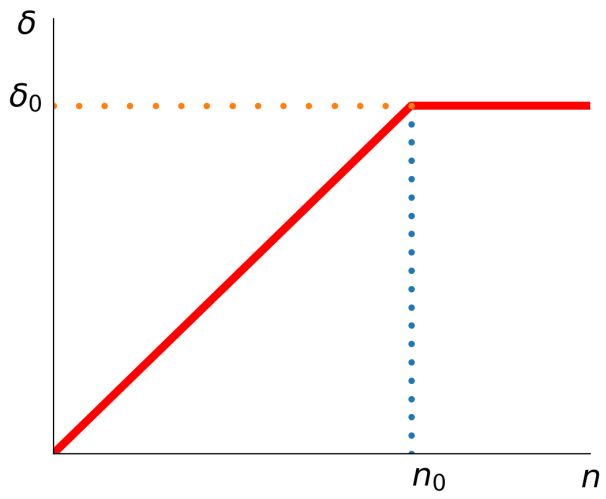

Figure 3.4: Displacement boundary condition δ versus numerical step n.

3.2.5 Evaluation of G

During each numerical step($n \geq n_0$), the strain energy for the entire model U is recorded, and the strain energy release rate G is calculated using Eqn.(2.10):

$$G = -\frac{dU}{da} \approx \frac{U_n - U_{n+1}}{a_{n+1} - a_n} \tag{3.3}$$

Here, in the 2D model, b is set to be 1 and hence does not appear explicitly in Eqn.(3.3).

3.3 Validation for G Calculation

To validate the above method of calculating G, this section presents the comparison between the FE result for a simple configuration shown in Figure 3.5 and the analytical solution for a DCB, Eqn.(2.22). Two models (A and B) with the same length L but different thicknesses H are used, as specified in Table 3.1. Both models are subject to the symmetric peeling condition. Because the analytical solution Eqn.(2.22) is based on linear elastic DCB, linear elastic material aluminum is used in FEA with Young's modulus and possion's ratio being $69000MPa$ and 0.33, respectively.

G for a linear elastic DCB under pure mode I loading is given by Eqn.(2.22):

$$G = \frac{3}{4}\frac{\delta^2 E h^3}{a^4} = \frac{3}{4}\frac{\delta^2 E}{h}(\frac{h}{a})^4$$

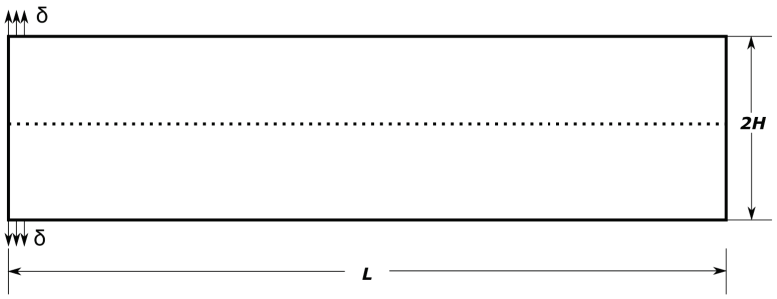

Figure 3.5: FE model with flat interface subject to symmetric peeling.

Table 3.1: Parameters for the two flat interface models.

parameter	Model A	Model B
$H(\mu m)$	30	10
$L(\mu m)$	200	200

To directly compare the FE results and analytical solutions for the two different models, a dimensionless $\bar{G}$ is defined as:

$$\begin{aligned} \bar{G} &\equiv \frac{G}{\frac{3}{4}\frac{\delta^2 E}{h}} \\ &= \frac{4h}{3\delta^2 E} G \\ &= (\frac{a}{h})^{-4} \end{aligned} \tag{3.4}$$

The FE results of G for models A and B are first multiplied by the factor $\frac{4h}{3\delta^2 E}$ and then plotted against a dimensionless crack length $\bar{a}$ defined as $\bar{a} = \frac{a}{h}$ in Figure 3.6. The corresponding analytical solution given by Eqn.(3.4) is also plotted in Figure 3.6. It is worth emphasizing that Eqn.(2.22) is derived based on the Bernoulli-Euler beam theory, which assumes that the beams are 'thin', with thickness $\ll$ length. This has led to a monotonic decrease of $\bar{G}$ with $\bar{a}$, and $\bar{G} \to \infty$ as $\bar{a} \to 0$.

Unlike the analytical DCB solution, $\bar{G}$ evaluated in FEA for both models initially increase with a/h. This is because when the crack is very short, the situation resembles a short crack in a 2D solid, rather than the DCB configuration. As the crack length increases, $\bar{G}$ eventually begins to decrease with

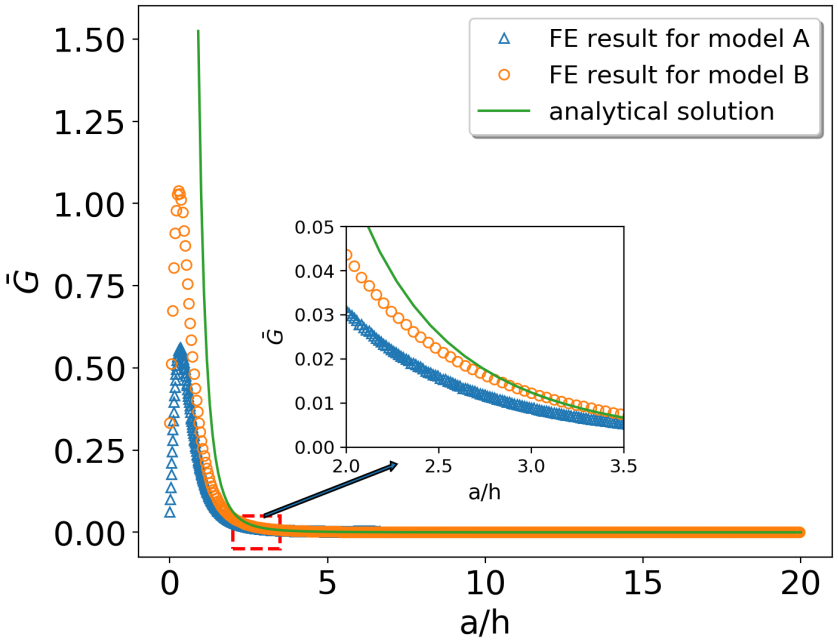

Figure 3.6: Comparison between the FE results and analytical solution for Model A and Model B.

a/h, as the model becomes closer to the DCB configuration. Moreover, as the model's thickness decreases (from model A to model B), $\bar{G}$ approaches the analytical solution in the decreasing branch as shown in the enlarged inlet. This observation is consistent with the Bernoulli-Euler beam theory where the model's thickness is assumed to be much smaller than its length. It is reasonable to expect that as the model's thickness further decreases, $\bar{G}$ evaluated in FEA will finally match the analytical solution in the decreasing branch. The comparison confirms the validity of our method to calculate G in FEA. In all the FE simulations performed in this work on patterned interface, a flat region is present at the beginning of interface separation, such that the first pattern appears in the decreasing branch of the G curve.

Chapter 4

Enhanced Adhesion with Symmetric Interfaces

The first objective of this chapter is to validate the FE model by comparing the results for the symmetric patterned interfaces with existing numerical results from literatures[14][13]. Two types of symmetric interfaces are examined including rippled and rectangular interfaces. Loading is applied through "pulling" to allow for direct comparison with literature. In addition, the effect of loading condition on the adhesion enhancement is discussed by considering "peeling" of the same models.

4.1 Rippled Interface

Figure 4.1 shows the schematic of a patterned interface that contains ripples which can be described by sinusoidal function $\frac{y(x)}{y_{max}} = \sin(\frac{2\pi x}{l})$, where l and y_{max} are the wave length and amplitude of the ripple, respectively. A flat interface serving as a control is also shown with the same apparent length L and thickness $2H$. l_f is the length of the flat region before the start of the pattern at point A. Points B and D are respectively the highest and lowest points in the first period of the pattern, while C marks the inflection point in this period. Projections of these points onto the flat interface are denoted by same symbol but with subscript 0. For simplicity, points in the subsequent periods of the pattern having the same relative positions will also be referred to as points A, B, C, D, with the specification of which period they are located

in. The geometrical parameters of the patterned surface are fixed and given in Table 4.1.

Table 4.1: Parameters for the rippled interface model (see Figure 4.1 for their definitions)

Parameter	value(μm)
y_{max}	4
l	20
l_f	25
L	150
H	60

Under the pulling condition, the bottom of the model is fixed and the top edge of the model is subjected to a uniform displacement δ, which first increases from 0 to $\delta_0 = 1\mu m$ in n_0 steps and then remains constant, as shown in Figure 3.4. Because the rippled pattern is symmetric, only one crack propagation direction is examined, from left to right as shown in Figure 4.1(c).

As explained in Section 3.2.5, during each numerical step, the strain energy for the entire model is recorded and the strain energy release rate G is calculated for the patterned interface ($G_{pattern}$) and flat interface(G_{flat}). The discretization in FEA has led to different node locations on the patterned and flat interfaces. To be able to directly compare $G_{pattern}$ and G_{flat} at the same apparent crack tip location, linear interpolation was done for the flat interface to extract G_{flat} at the same locations as the nodes in the patterned model.

Figure 4.2 shows $G_{pattern}$ and G_{flat} plotted against the actual crack tip location a. For the rippled interface, a is defined as the total distance along the curved surface before the crack tip. As can be seen, before the start of the pattern (point A), $G_{pattern}$ follows G_{flat}. It then deviates from G_{flat} and shows a discontinuity at A where the crack propagation suddenly changes direction. Afterwards, the direction of the crack changes smoothly and there is no abrupt change observed in the $G_{pattern}$ curve. After the crack tip passes the last "kink" connecting the rightmost end of the sinusoidal curve and the flat region, $G_{pattern}$ follows G_{flat} again.

To compare $G_{pattern}$ and G_{flat}, it is convenient to use the energy release

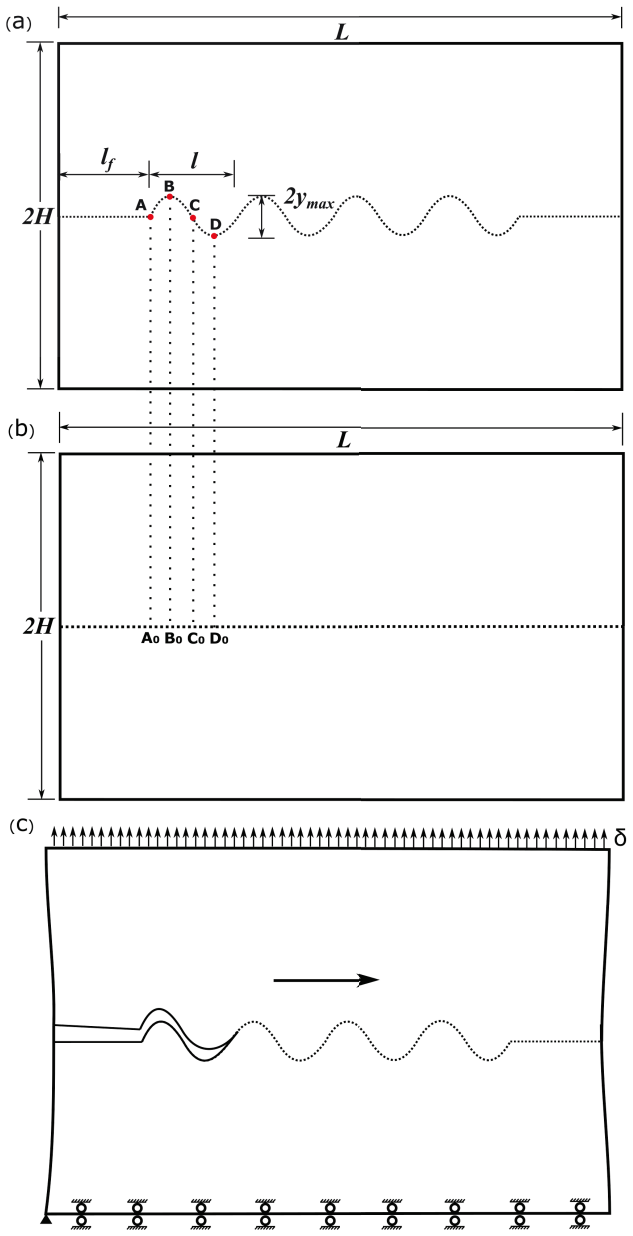

Figure 4.1: Schematics of (a) the interface with rippled pattern, (b) flat control and (c) the pulling condition, where the arrow indicates the crack propagation direction.

rate ratio defined by Eqn(2.28) in Chapter 2, $R = \frac{G_{pattern}}{G_{flat}}$. Figure 4.3(a) shows the schematic of crack propagation along the rippled interface. The five periods of the pattern are denoted by I, II, III, IV and V based on the sequence in which they are accessed by the crack tip. Figure 4.3(b)(c) show how R changes with the apparent crack tip location x and the actual crack tip

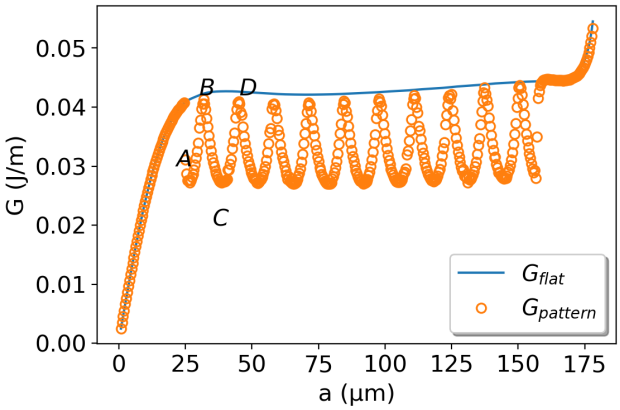

Figure 4.2: $G_{pattern}$ and G_{flat} for the rippled interface under the pulling condition, plotted against the actual crack tip location a.

location a, respectively. Figure 4.3(d) shows enlarged region in Figure 4.3(c), where A^- is used to denote the location just prior to (one node before) point A.

As can be seen in Figure 4.3(b), from the leftmost end to A^- the crack is horizontal (flat) and the R value is equal to 1. Between A^- and A, R experiences an abrupt decrease from 1.03 to 0.71. From A to B the surface is ramping-up with a decreasing slope, and R first decreases to a local minimum of 0.59 and then increase to 0.96. From B to C, the surface is ramping-down with an increasing slope and R decreases from 0.96 to 0.59. The variation of R for the rest of period I is similar to what is observed from A to C. As well, from period I to V, the R curve shows periodic pattern.

Figure 4.4 shows the minimum of $R(R_{min})$ during each period versus the apparent crack tip location x and the corresponding locations on the patterned interface. As can be seen, R_{min} always occurs in the vicinities of A and C in each period where the slope of the surface is the largest in magnitude. The adhesion enhancement factor in the patterned interface is given by Eqn.(2.29), $F = \frac{1}{R_{min}}$, and plotted in Figure 4.5 against the crack tip location where R_{min} occurs. F values obtained previously in literature [13] are extracted and shown in the same figure. As can be seen in Figure 4.5, the F values from our FE model vary in the range of 1.52 to 1.58, which are slightly higher than those reported in [13] with a value of 1.47. The discrepancy could be due to the

different model dimensions (L and H values)or mesh sizes used, which are not specified in [13]. It is also worth mentioning that F magnifies the difference in R_{min} between our work and [13], which is very small ($< 5\%$).

With the assumptions made in deriving Eqn.(2.30), the theoretical F value can be calculated as follows. Recall the shape of the ripple is obtained:

$$\frac{y(x)}{y_{max}} = \sin(\frac{2\pi x}{l})$$

The slope of the surface is then given by:

$$\tan(\alpha) = \frac{dy}{dx} = \frac{2\pi y_{max}}{l}\cos(\frac{2\pi x}{l})$$

Thus, the tangential angle along the interface is given by:

$$\alpha = \tan^{-1}(\frac{2\pi y_{max}}{l}\cos(\frac{2\pi x}{l}))$$

for the specific rippled interface considered here, $\frac{2y_{max}}{l} = 0.4$. Thus, the highest tangential angle along the surface is:

$$|\alpha_{max}| = \tan^{-1}(0.4\pi)$$

which occurs at $\frac{2\pi x}{l} = m\pi$, or $x = \frac{m}{2}l$, where m is an integer. By substituting α_{max} to Eqn.(2.30), the theoretical F value can be obtained:

$$F_{theory} = \frac{1}{\cos^4(\frac{\alpha_{max}}{2})} = 1.52$$

which is plotted in Figure 4.5 for comparison with those evaluated from our FE model and from the literature. This predication indicates that the adhesion enhancement is independent of the crack tip locations where R_{min} occurs, which is in well agreement with the numerical results. The small deviation between the numerical results and F_{theory} is believed to result from several violations of the assumptions of Eqn.(2.30) including the crack being embedded in an infinite body and the crack surface before the crack tip being flat.

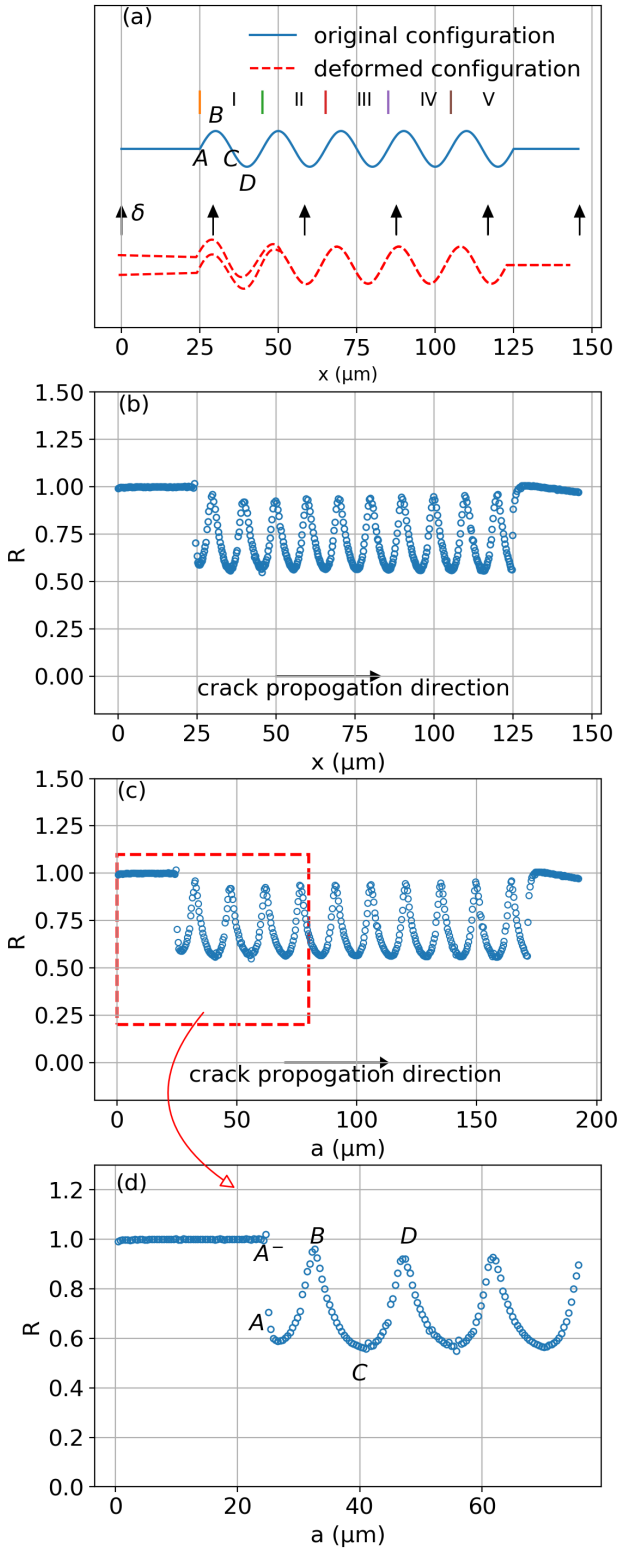

Figure 4.3: Energy release rate ratio R for the rippled interface under the pulling condition. (a) is the schematic of the interface as the crack propagates. (b) and (c) are R versus apparent crack tip location x and the actual crack tip location a, respectively. (d) is the enlarged region in (c).

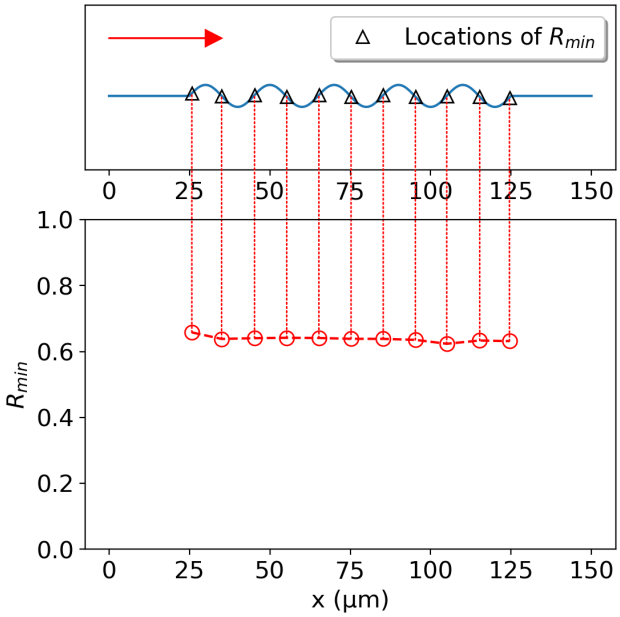

Figure 4.4: R_{min} for the rippled interface under the pulling condition, plotted against the apparent crack tip location where R_{min} occurs. The red arrow indicates the crack propagation direction.

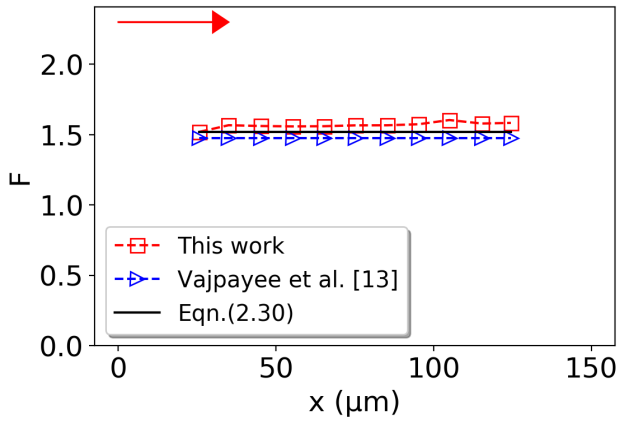

Figure 4.5: Adhesion enhancement factor F for the rippled interface under the pulling condition, evaluated from our FE model and literature [13] as well as Eqn.(2.30), plotted against the apparent crack tip location where R_{min} occurs. The red arrow indicates the crack propagation direction.

4.2 Rectangular Interface

Figure 4.6 shows the schematic of a patterned interface that contains rectangles. A flat interface serving as control is also shown with the same apparent length L and thickness $2H$. Figure 4.6(a) also marks the first four kinks on the patterned interface where the crack propagation changes direction. They are denoted by A, B, C and D based on the sequence in which they are accessed by the crack tip. The projections of these points onto the flat interface are denoted by the same symbol but with subscript 0. A to B is a vertical line on the patterned interface, and hence their projections overlap on the flat control. The same is true for C and D. The geometrical parameters of the patterned interface are fixed and given in Table 4.2. Similar to the rippled interface, $\delta_0 = 1\mu m$ is used and only one crack propagation direction is examined, from left to right as shown in Figure 4.6(c). The same steps to calculate $G_{pattern}$, G_{flat} and R are also followed here.

Table 4.2: Parameters for the rectangular interface model (see Figure 4.6 for their definitions)

Parameter	value(μm)
y	10
l	10
l_f	50
L	170
H	60

Figure 4.7(a) shows $G_{pattern}$ and G_{flat} plotted against the actual crack tip location a. For the rectangular interface, a is defined as the total distance along the separated surfaces before the crack tip. For example, the projection of any points along a vertical path onto the flat interface is a single point. For this part, a increases but G_{flat} is a single value, as shown in Figure 4.7(b). $G_{pattern}$ initially follows G_{flat} before the first kink. It then deviates from G_{flat} and shows a discontinuity when the crack propagation changes direction. After the crack tip passes the last kink close to the rightmost end, $G_{pattern}$ follows G_{flat} again.

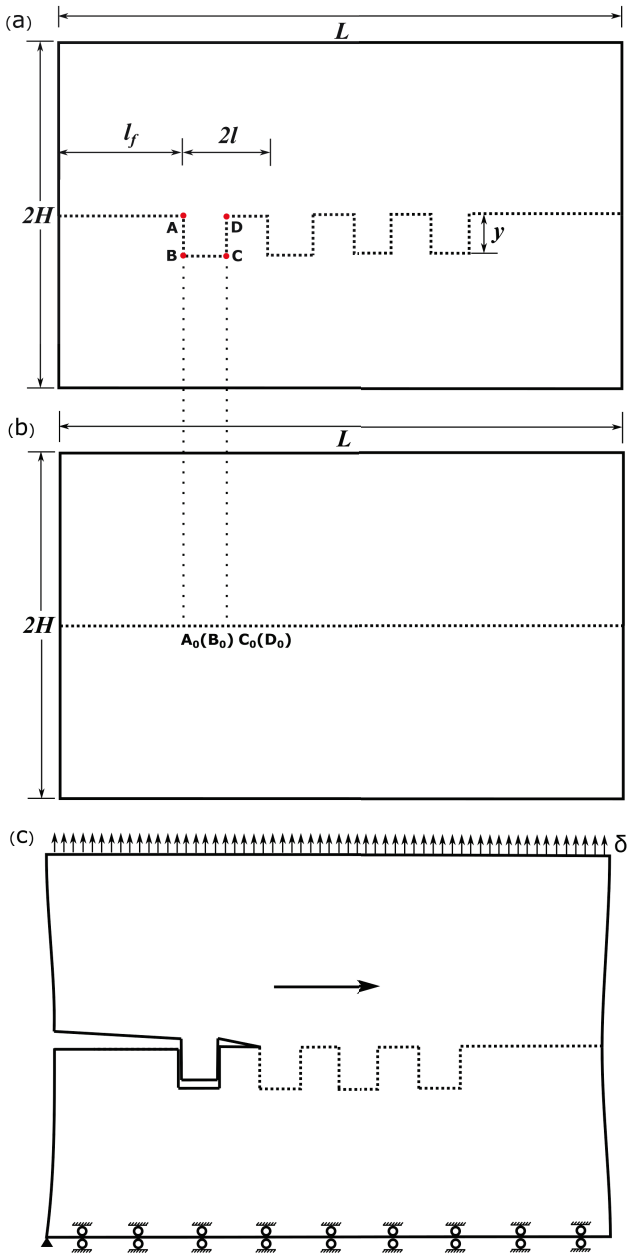

Figure 4.6: Schematics of (a) the interface with rectangular patten, (b) flat control and (c) the pulling condition. The arrow indicates crack propagation direction.

Figure 4.8(a) shows the schematic of crack propagation along the rectangular interface, with the five periods denoted I to V. Figure 4.8(b) and (c) show how R changes with the apparent crack tip location x and the actual crack tip location a. Figure 4.8(d) shows the enlarged region in Figure 4.8(c), where superscripts $-$ is used to denote the location just prior to each kink.

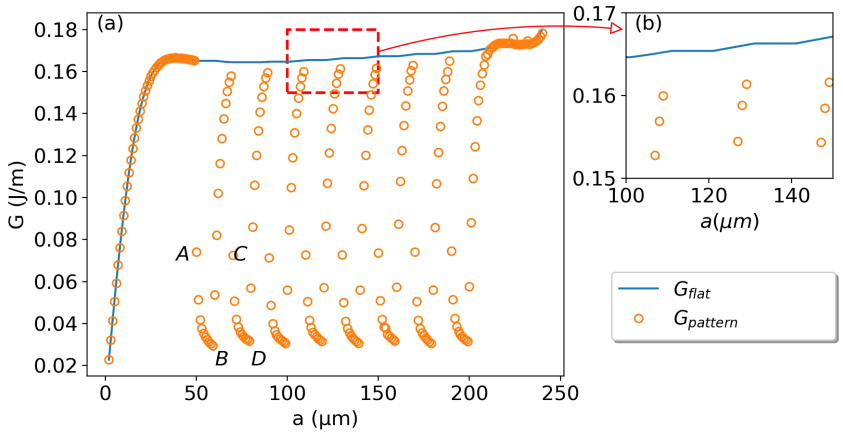

Figure 4.7: (a) $G_{pattern}$ and G_{flat} under the pulling condition, plotted against the actual crack tip location a. (b) enlarged region in (a).

For example, A^- refers to the location one node prior to A.

From the leftmost end to A^-, the crack is horizontal (flat) and the R value is equal to 1. Between A^- and A, R experiences an abrupt decrease from 1 to 0.41. From A to B^-, the surface is vertical (vertical-down) and R decreases further from 0.41 to 0.2. Between B^- and B, R experiences an abrupt increase from 0.2 to 0.37. From B to C^-, the crack is flat again but R is not constant. Instead it quickly increases from 0.37 to a value close to 1. From C^- to D (vertical-up), R changes in the same manner as that from A^- to B. From period I to V, R curve shows periodic pattern.

Figure 4.9 shows R_{min} versus the apparent crack tip location and the corresponding locations on the interface. As can be seen, R_{min} always occurs in the vicinities of B and D, which are the ends of the vertical-down and vertical-up surfaces, respectively. The adhesion enhancement factor F is plotted in Figure 4.10 against the crack tip locations where R_{min} occurs. Upon examining the R curve presented in the literature (see Figure 10 in [14]), spikes (suddenly drops in R) can be observed near several local minima, which are not present in our calculations. Such spikes are not present for every period of the pattern, and are not discussed in [14]. Not knowing the details of the simulations in [14], we cannot determine the source of these spikes, although we suspect they are likely caused by numerical errors as the mesh appears to be coarse outside the patterned region. Nevertheless, by neglecting the spikes in the R curve,

the F values are extracted and plotted in the same figure. As can be seen in Figure 4.10, there are some discrepancies between F values from this work and from [14]. While we tried to simulate the rectangular pattern with the same dimensions as in [14], i.e., the same y and l in Figure 4.6, certain model dimensions are not specified in [14], e.g., L, H and l_f in Figure 4.6. This is likely the reason for the discrepancies seen in Figure 4.10. Also, as discussed in Section 4.1, F magnifies the discrepancy in R_{min}, which is much smaller (in the range of 0.03 to 0.05)

The theoretical F can be calculated by Eqn.(2.30). For the rectangular model considered here, the maximum angle along the surfaces is 90°. Thus, the theoretical F value is given by:

$$F_{theory} = \frac{1}{\cos^4(\frac{\alpha_{max}}{2})} = \frac{1}{\cos^4(\frac{90^\circ}{2})} = 4$$

which is also plotted in Figure 4.10. The deviation of numerical results from F_{theory} is again due to the violation of the assumptions in deriving Eqn.(2.30). In particular, one strong assumption states the surface before the crack tip is flat whereas in our model the surface before the crack tip where R_{min} occurs is vertical.

To conclude, we examined the rippled and rectangular interfaces under the pulling condition. Without knowing the exact geometries of the models in [13][14], our results are not only in excellent qualitative agreement, but also close quantitatively (discrepancy in $R_{min} < 5\%$ for rippled interface and $< 20\%$ for rectangular interface). Thus, it is reasonable to conclude that our FE model is validated.

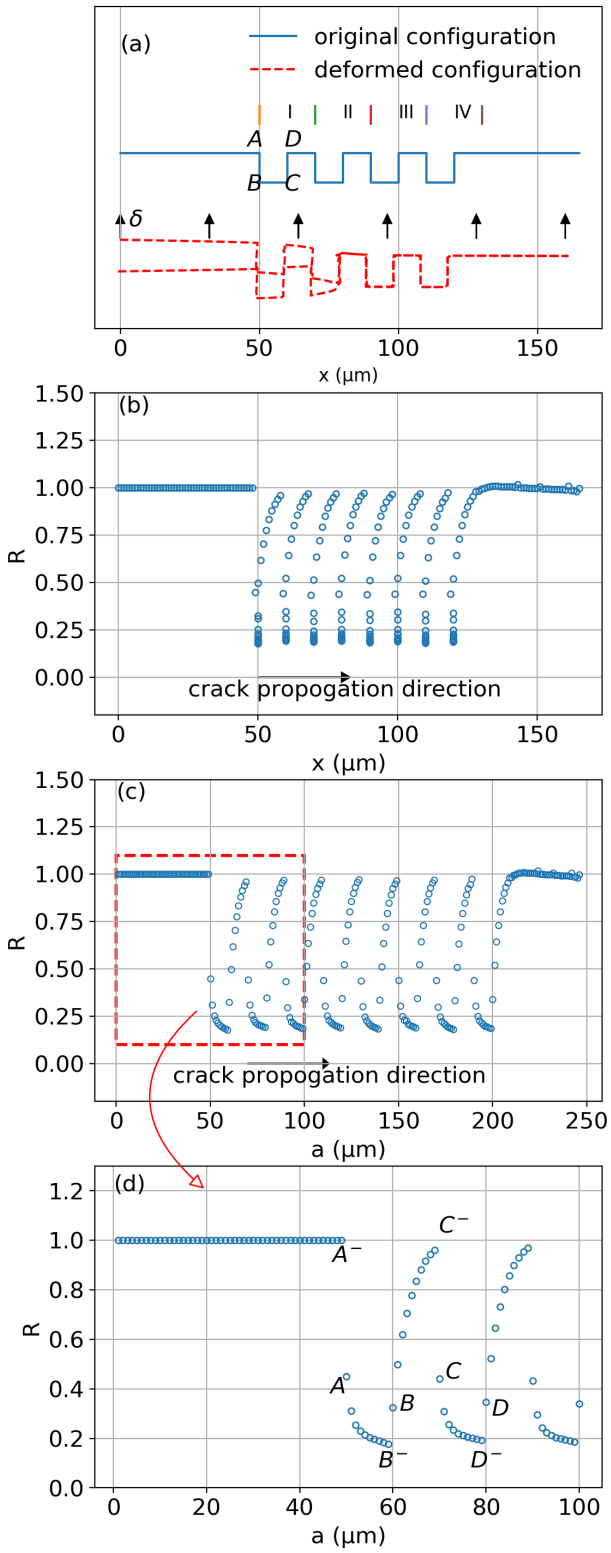

Figure 4.8: Energy release rate ratio R for the rectangular interface under the pulling condition. (a) is the schematic of the interface as the crack propagates. (b) and (c) are R versus apparent crack tip location x and the actual crack tip location a, respectively. (d) is the enlarged region in (c).

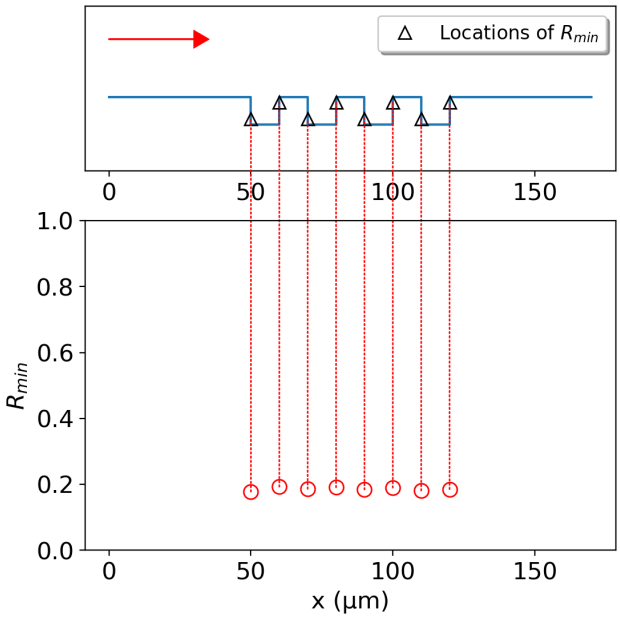

Figure 4.9: R_{min} for the rectangular interface under the pulling condition, plotted against the apparent crack tip location where R_{min} occurs. The red arrow indicates the crack propagation direction.

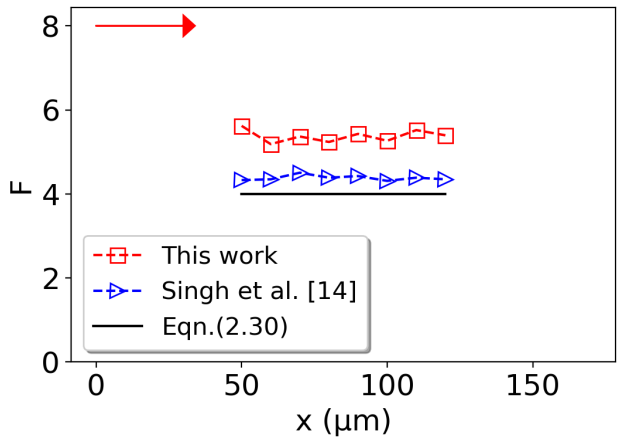

Figure 4.10: Adhesion enhancement factor F for the rectangular interface under the pulling condition, evaluated from our FE model and literature [14] as well as Eqn.(2.30), plotted against the apparent crack tip location where R_{min} occurs. The red arrow indicates the crack propagation direction.

4.3 Effect of Loading Condition

In real applications, a patterned interface can and is more likely to be subjected to a peeling condition, instead of a uniformly distributed pulling condition. To investigate how the adhesion enhancement factor could be affected by the loading condition, the same models simulated in sections 4.1 and 4.2 are now considered under peeling, where the bottom is fixed and the first few nodes on the top left edge are loaded with a fixed displacement boundary condition δ as shown in Figure 3.4 with $\delta_0 = 1\mu m$. The same steps used to calculate $G_{pattern}$, G_{flat} and R in the case of pulling are followed here. The crack on the interface propagates from left to right as shown in Figure 4.11.

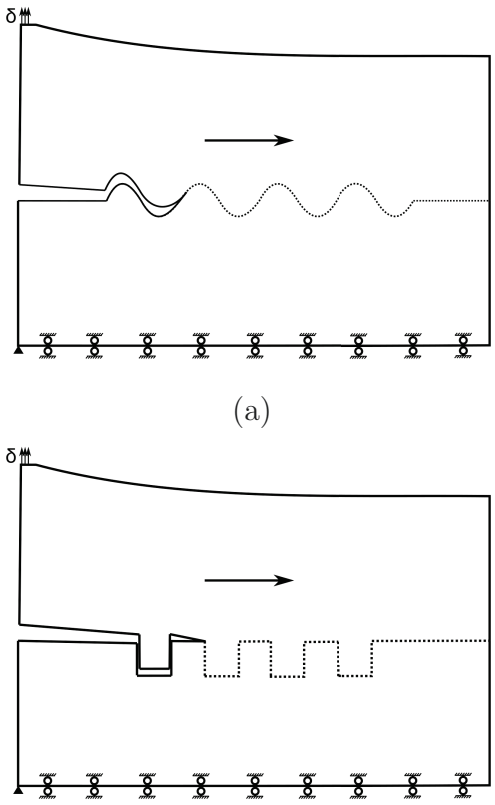

Figure 4.11: Schematics of (a) the rippled interface and (b) the rectangular interface under peeling. The arrows indicate the crack propagation direction.

Figure 4.12 shows $G_{pattern}$ and G_{flat} for the rippled interface under peeling, plotted against the actual crack tip location a. Comparing this plot to Figure

4.2, there are several differences. Firstly, while $G_{pattern}$ and G_{flat} also increase at the beginning, like in Figure 4.2, they exhibit an overall decreasing trend after a reaches a certain value around $25\mu m$. Secondly, different from Figure 4.2, $G_{pattern}$ is no longer periodic when the crack propagates through the periodic ripples. Finally, $G_{pattern}$ exceeds G_{flat} at some locations in Figure 4.12 whereas the $G_{pattern}$ curve in Figure 4.2 is always below the G_{flat} curve.

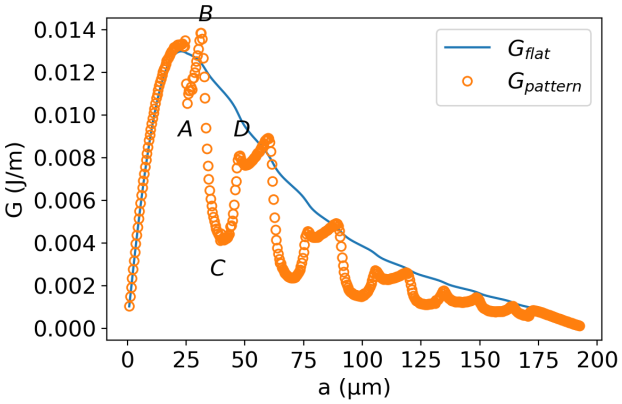

Figure 4.12: $G_{pattern}$ and G_{flat} for the rippled interface under peeling, plotted against the actual crack tip location a.

Figure 4.13(a) shows the schematics of crack propagation along the rippled interface, with the five periods denoted by I to V. Figure 4.13(b) and (c) show how R changes with the apparent crack tip location x and the actual crack tip location a. Figure 4.13(d) shows the enlarged region in Figure 4.13(c). Local minima R_{min} and their locations are plotted in Figure 4.15. As can be seen, from periods I to V, R curve shows some periodic trend but its magnitudes including maxima and minima vary from one period to another. Besides, while R_{min} on the ramping-down surface still occurs in the vicinity of C, the location of R_{min} on the ramping-up surface is not always near A. Instead it moves from the vicinity of D to the vicinity of A as the crack tip propagates from periods I to V. This indicates that the application of peeling condition has led to the loss of periodicity in R. The adhesion enhancement F is plotted in Figure 4.15 against the location where R_{min} occurs. Comparing this plot to Figure 4.5, F has a much greater variation with the apparent crack tip location x, which is now in the range of 1.15 to 1.75 on the ramping-up surfaces and 1.83

to 2.73 on the ramping-down surfaces. F on the ramping-down surfaces is general higher than F on the ramping-up surfaces, while these two sets of F values approach each other as the crack propagates, which is expected to reach a steady value. Under the same δ, F values in Figure 4.15 are overall greater than those in Figure 4.5, indicating stronger adhesion enhancement under the peeling condition.

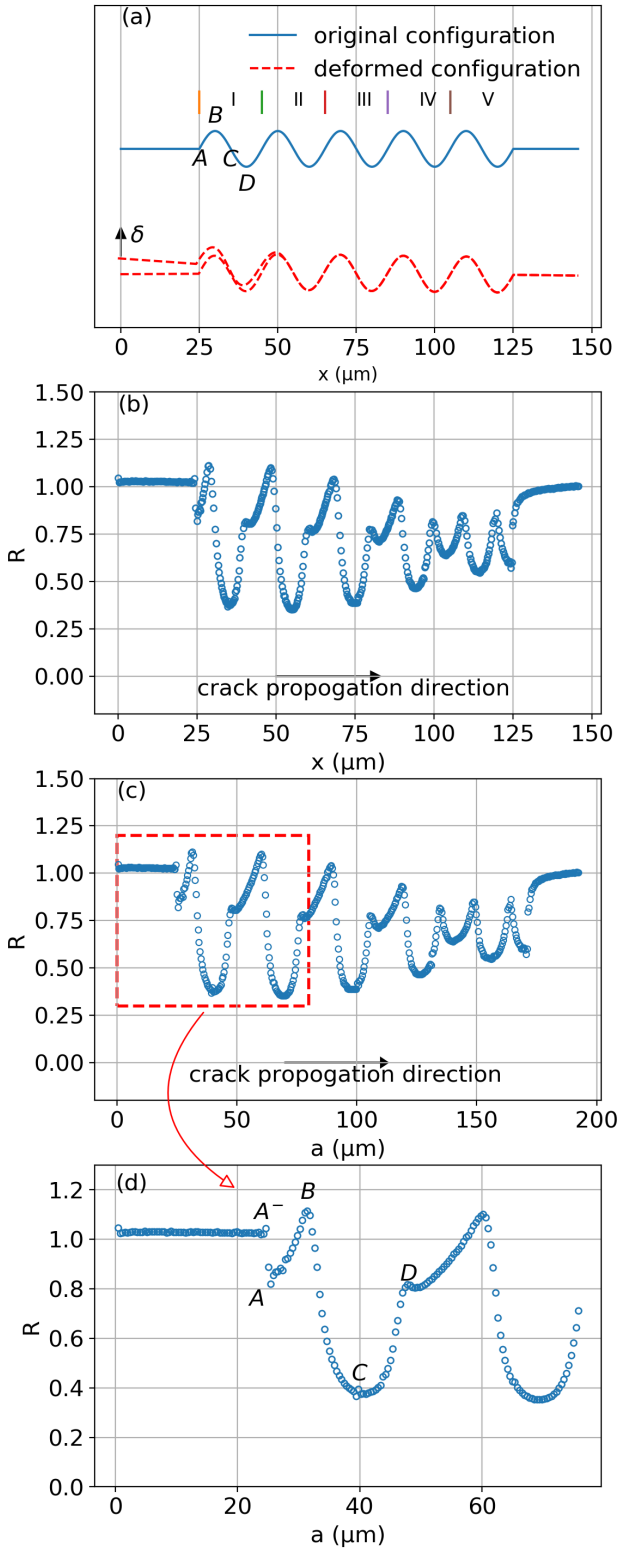

Figure 4.13: Energy release rate ratio R for the rippled interface under peeling. (a) is the schematic of the interface as the crack propagates. (b) and (c) are R versus apparent crack tip location x and the actual crack tip location a, respectively. (d) is the enlarged region in (c).

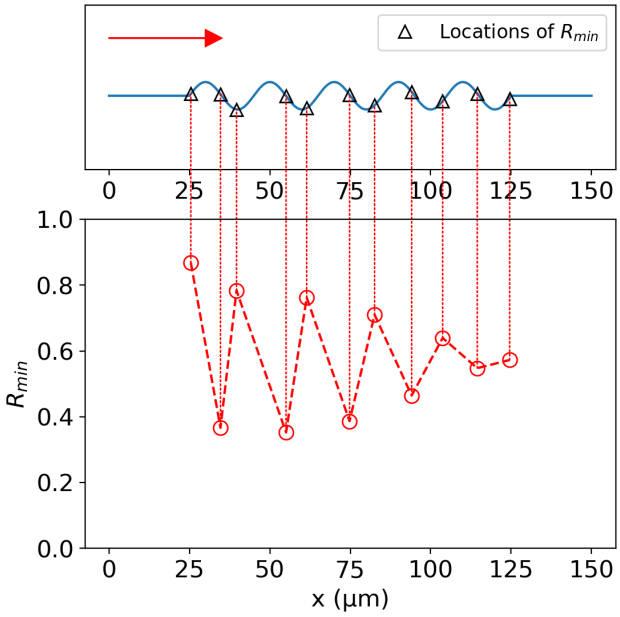

Figure 4.14: R_{min} for the rippled interface under peeling, plotted against the apparent crack tip location where R_{min} occurs. The red arrow indicates the crack propagation direction.

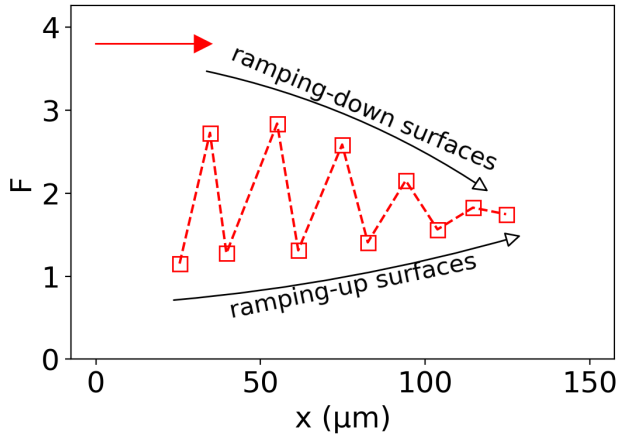

Figure 4.15: Adhesion enhancement factor F for the rippled interface under peeling, plotted against the apparent crack tip location where R_{min} occurs. The red arrow indicates the crack propagation direction.

Figure 4.16 shows $G_{pattern}$ and G_{flat} for the rectangular interface under the peeling condition, plotted against the actual crack tip location a, which again shows significant difference from Figure 4.7 under pulling. Figure 4.17(a) shows the schematic of the crack propagation along the rectangular interface. Figure 4.17(b) and (c) shows how R changes with the apparent crack tip location x and the actual crack tip location a. Figure 4.17(d) shows the enlarged region in Figure 4.17(c). R_{min} values and their locations are plotted in Figure 4.18. Similarly to the rippled interface, the periodicity in R observed under pulling is lost due to the application of peeling. Besides, the location of R_{min} are no longer limited to points B and D. Instead, it can occur anywhere on the vertical-up and vertical-down surfaces. Figure 4.19 shows the adhesion enhancement factor F plotted against the apparent crack tip location x. Comparing this plot to Figure 4.10, F has a much greater variation with the apparent crack tip location. While F on the vertical-down surfaces is lower than that in Figure 4.10, in the range of 3.17 to 4.01, F on the vertical-up surfaces is as high as 12.7 at the beginning, although it decreases for later periods and approaches the values on the vertical-down surfaces.

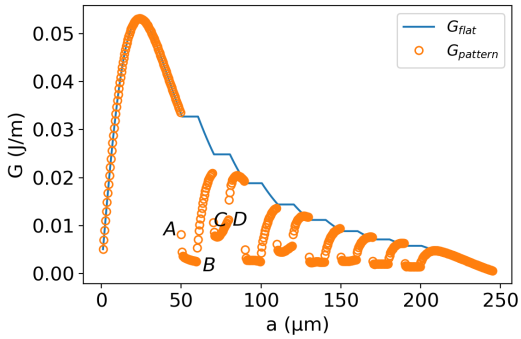

Figure 4.16: $G_{pattern}$ and G_{flat} for the rectangular interface under peeling, plotted against the actual crack tip location a.

To conclude, the application of the peeling condition can strongly affect the adhesion enhancement. It can lead to the loss of periodicity in R, change location of R_{min} (hence where crack trapping may occur) and magnitude of F. Because of this, in the next chapter the asymmetric interfaces will be investigated under both pulling and peeling conditions.

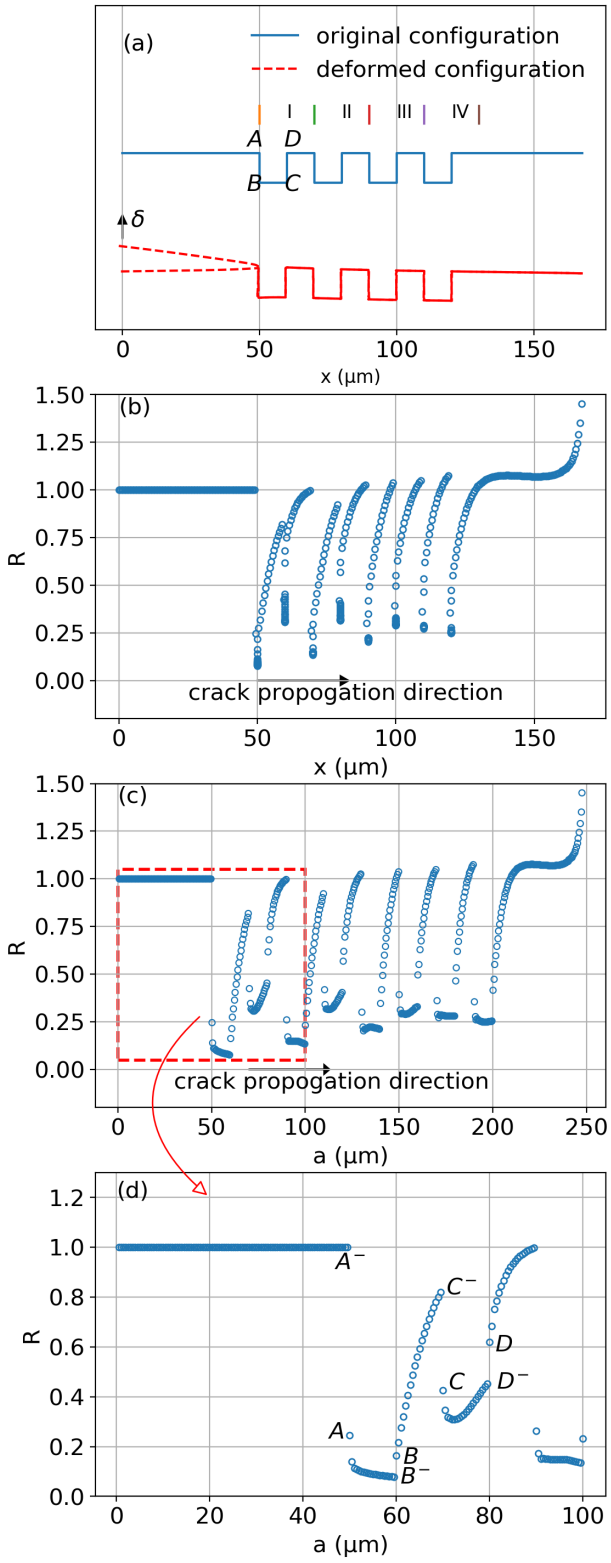

Figure 4.17: Energy release rate ratio R for the rectangular interface under peeling. (a) is the schematics of the interface as the crack propagates. (b) and (c) are R versus apparent crack tip location x and the actual crack tip location a, respectively. (d) is the enlarged region in (c).

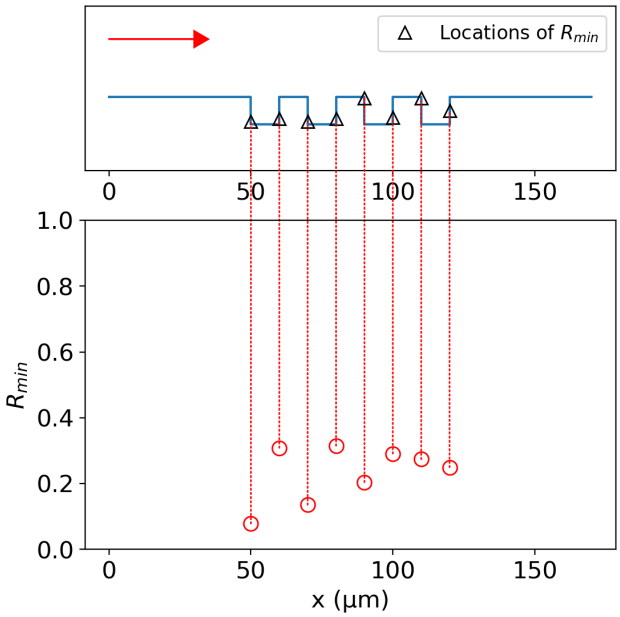

Figure 4.18: R_{min} for the rectangular interface under peeling, plotted against the apparent crack tip location where R_{min} occurs.

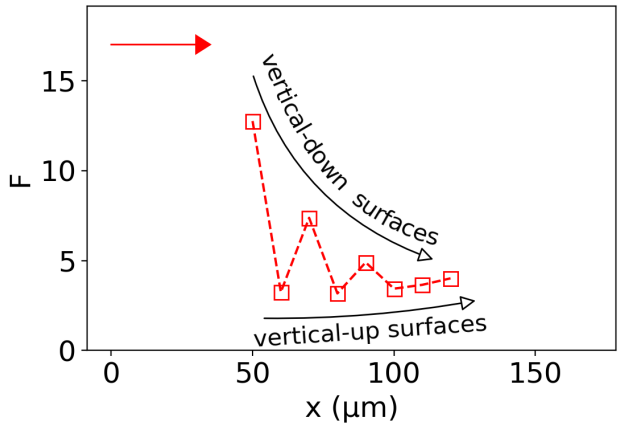

Figure 4.19: Adhesion enhancement factor F for the rectangular interface under peeling, plotted against the apparent crack tip location where R_{min} occurs.

Chapter 5

Directional Adhesion with Asymmetric Interfaces

The objective of this chapter is to investigate whether the adhesion enhancement in an interface consisting of asymmetric pattern can be different via opposite crack propagation directions. Since it has been shown in Section 4.3 that the loading condition can have profound effect on adhesion enhancement, the asymmetric interface is first considered under the symmetric peeling condition. Afterwards, asymmetric peeling and pulling are also examined. The definition of each loading condition is given in Section 3.2.4. For the pulling and symmetric peeling conditions, two opposite crack propagation directions are examined; for the asymmetric peeling condition, four ways of propagating the crack are considered.

5.1 Symmetric Peeling

Figure 5.1 shows the schematic of a patterned interface that contains right triangles separated by flat regions. A flat interface serving as a control is also shown with the same apparent length (L) and thickness ($2H$). Equal and opposite displacements δ are applied to the first few nodes on the top and bottom edges of the model, which first increases from 0 to $\delta_0 = 1\mu m$ in n_0 steps and then remains constant, as shown in Figure 3.4. Because the triangular pattern is asymmetric, two peeling directions are examined, as shown in Figure 5.2. As the crack propagates from left to right (peeling direction 1), it first

travels upwards along the vertical side of the triangle, and then downwards along the hypotenuse. As the crack propagates from right to left (peeling direction 2), it first travels upwards along the hypotenuse, and then downwards along the vertical side. Figure 5.1 also illustrates the first three 'kinks' on the patterned interface where the crack propagation changes direction. They are denoted by A, B and C based on the sequence in which they are accessed by the crack tip. Subscripts 1 and 2 are used to denote different peeling directions, for example A_1 corresponds to the first 'kink' accessed by the crack tip in peeling direction 1. Projections of these points onto the flat interface are denoted by the same symbol but with subscript 0. The geometrical parameters of the patterned surface are fixed and given in Table 5.1. It is worth mentioning that the real application of the simulated sample is a thin film, i.e., $L \gg H$. Thus, in FEA the lateral length of the sample is set to be much larger than the thickness as well as the dimensions of the triangular teeth.

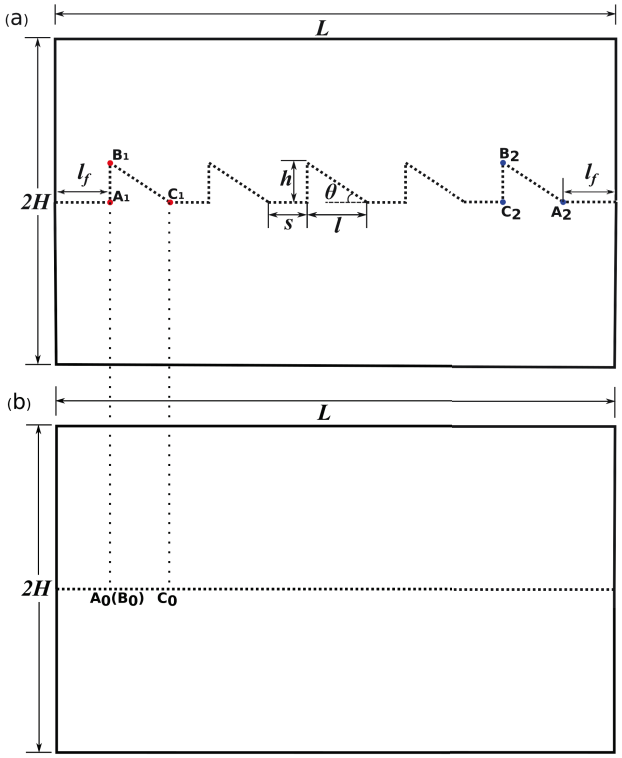

Figure 5.1: Schematics of (a) the interface with triangular pattern and (b) flat control.

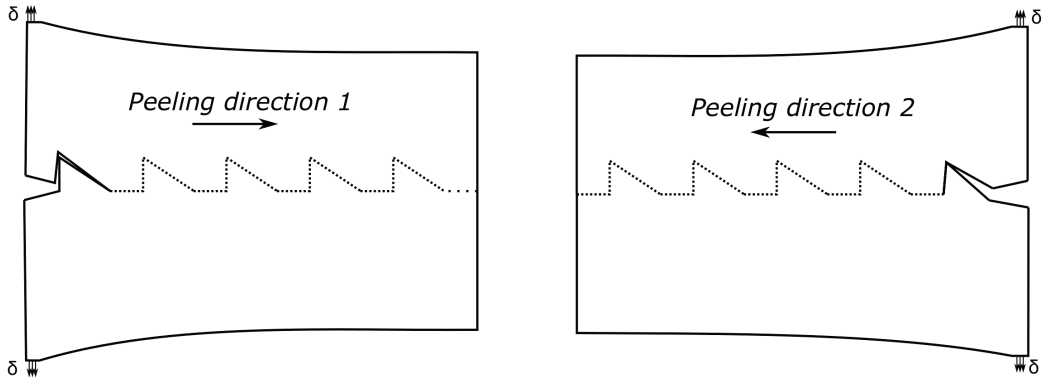

(a) (b)

Figure 5.2: Schematics of symmetric peeling along (a) direction 1 and (b) direction 2

Table 5.1: Parameters for the triangular interface model (see Figure 5.1 for their definitions). In addition, $\theta = 30°$

parameter	value (μm)
h	2.3
l	4
s	20
l_f	60
$\theta(°)$	30
L	219
H	14

Similarly to what was done in Chapter 4, $G_{pattern}$ and G_{flat} are calculated by gradually releasing the "tied" nodes. Linear interpolation was done for the flat interface to extract G_{flat} at the same locations as the nodes in the patterned model. As well, a grid study has been conducted to determine the appropriate meshing scheme. Specifically, $G_{pattern}$ at B_1 and B_2 (see Figure 5.1 for the definition of B_1 and B_2) are monitored while varying the total number of elements as shown in Figure 5.3(a). Finally a total number of 244517 elements is chosen for this study and the mesh for a region near B_1 is shown in Figure 5.3(b).

Figure 5.4 shows $G_{pattern}$ and G_{flat} versus a, the actual crack tip location for peeling direction 1. For the triangular interface, a is defined as the total

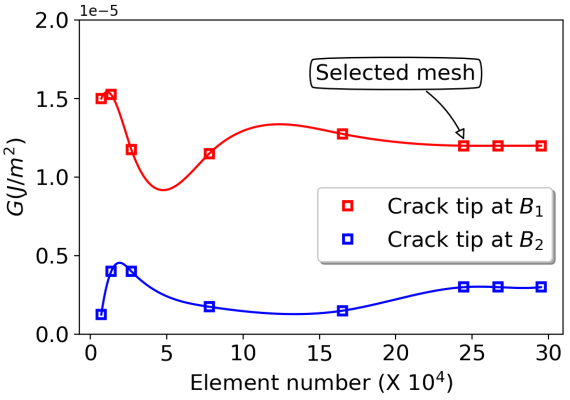

(a)

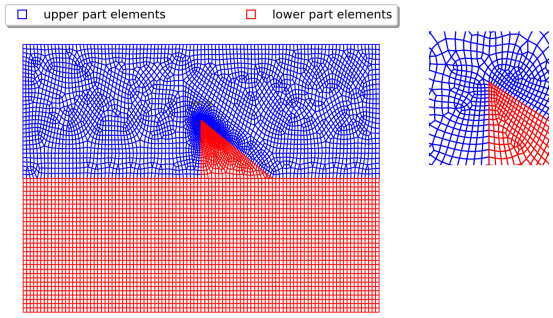

(b)

Figure 5.3: (a) $G_{pattern}$ at B_1 and B_2 versus the total number of elements, for symmetric peeling along direction 1. (b) mesh with 244517 elements for a region near B_1, with the sub-figure showing the further enlarged region near B_1.

distance along the separated surfaces before the crack tip. For example, the projection of any points along the vertical path from A_1 to B_1 onto the flat interface is a single point $A_0(B_0)$. For this part, a increases but G_{flat} is a single value, as shown in the enlarged inset. As can be seen, before the first kink $G_{pattern}$ follows G_{flat}; it then deviates from G_{flat} and shows discontinuity when the crack propagation changes direction.

To compare $G_{pattern}$ and G_{flat}, it is convenient to use energy release rate ratio, $R = \frac{G_{pattern}}{G_{flat}}$. Results for the two peeling directions are shown in Figure 5.5 and 5.6, respectively. The colour grey is used to highlight regions where $R > 1$, while blue is used to highlight regions with $R \leq 1$. Figure 5.5(a) shows the schematic as the crack propagates along the triangular interface along direction 1. The five periods of the pattern are denoted by I, II, III, IV and

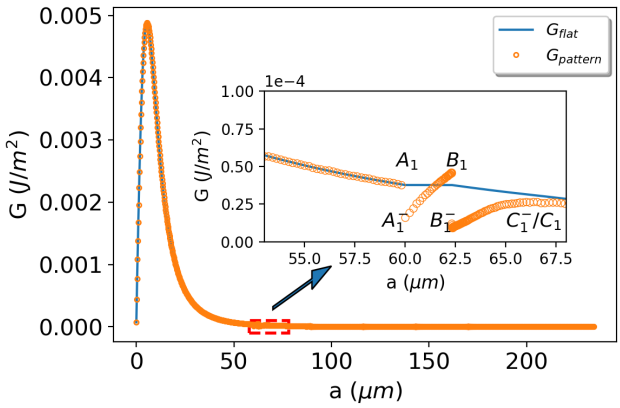

Figure 5.4: $G_{pattern}$ and G_{flat} versus the actual crack length a for peeling direction 1.

V according to the sequence in which they are accessed by the crack tip. Figure 5.5(b)(c) show how R changes with the actual crack tip location a and the apparent crack tip location x. Figure 5.5(d) shows the enlarged regions in Figure 5.5(b), where superscript $-$ is used to denote the location just prior to the 'kink' in the pattern. For example, B_1^- refers to the location one node prior to B_1. Similar plots are shown in Figure 5.6 for peeling direction 2.

In the case of peeling direction 1 shown in Figure 5.5, from the leftmost end to A_1^- the crack is horizontal (flat) and R is equal to 1. Between A_1^- and A_1, R experiences an abrupt decrease from 1 to 0.40. From A_1 to B_1^-, the crack surface is vertical (vertical-up) and R increases from 0.40 to 1.20. Between B_1^- and B_1, R suddenly decreases from 1.20 to 0.23. From B_1 to C_1^-, the crack surface has an angle of 30° below horizontal (ramping-down) and R increases from 0.23 to 0.81. Between C_1^- and C_1, R slightly increases from 0.81 to 0.82. From C_1 to A_1^- in period II, the crack surface is flat again yet the R curve is not flat, instead it increases from 0.82 to a plateaus value of 0.95. From period I to period V, the R curve shows periodic pattern but its magnitude varies from one period to another.

In the case of peeling direction 2 shown in Figure 5.6, from the rightmost end to A_2^-, the crack surface is horizontal (flat) and R is equal to 1. Between A_2^- and A_2, R slightly decreases from 1 to 0.90. From A_2 to B_2^-, the crack surface has an angle of 30° above horizontal (ramping-up) and R increases

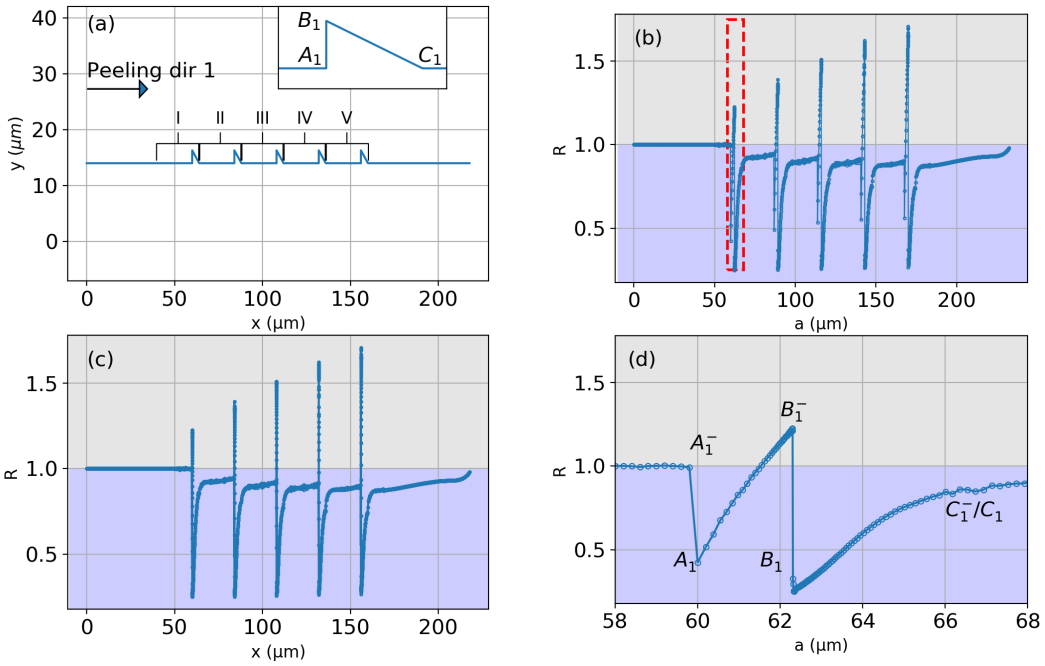

Figure 5.5: Energy release rate ratio R for peeling direction 1. (a) schematic of the interface and the five periods, (b) R versus the actual crack tip location, (c) R versus the apparent crack tip location, (d) enlarged region in (b).

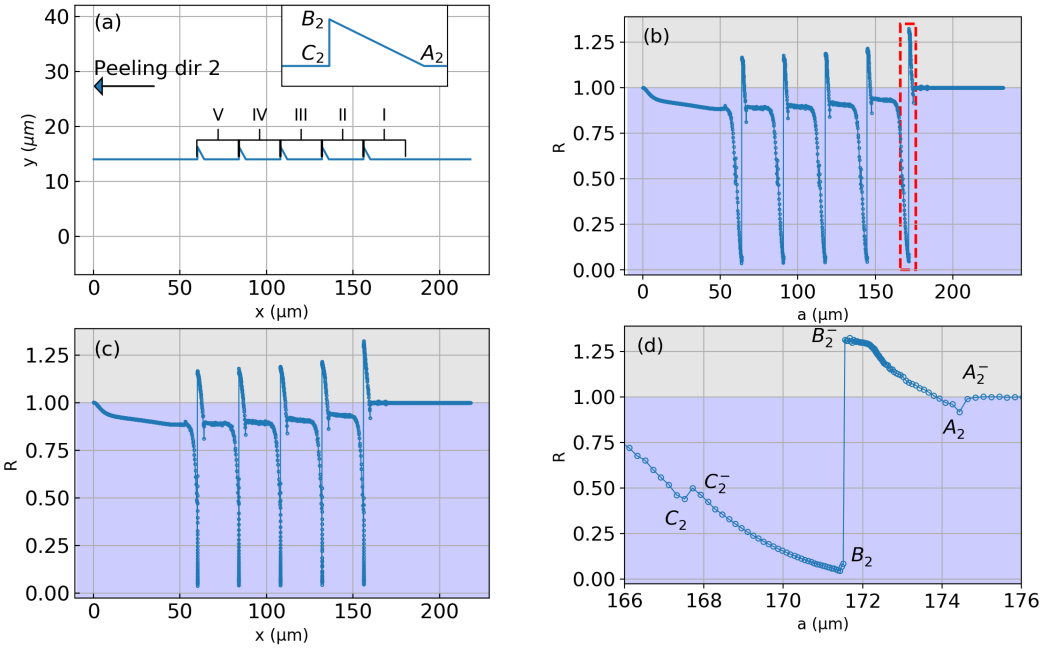

Figure 5.6: Energy release rate ratio R for peeling direction 2. (a) schematic of the interface and the five periods, (b) R versus the actual crack tip location, (c) R versus the apparent crack tip location, (d) enlarged region in (c).

from 0.90 to 1.30. Between B_2^- and B_2, R experiences an abrupt decrease from 1.30 to 0.08. From B_2 to C_2^-, the crack surface is vertical (vertical-down) and R increases from 0.08 to 0.49. Between C_2^- and C_2, R slightly decreases from 0.49 to 0.44. From C_2 to A_2^- in period II, the crack surface is flat yet R is not 1, instead it increases from 0.44 to a plateaus value of 0.93. From period I to period V, the R curve shows periodic pattern but variations in its magnitude.

Several similarities can be observed between the results from the two peeling directions. Firstly, for both peeling directions the R curves show discontinuities at 'kinks' where the crack propagation changes direction. Secondly, R in the first flat region is constant and equal to 1, but this does not hold in later flat regions. Finally, figure 5.7 shows the minimum values of R (R_{min}) during each period versus the apparent crack tip location x and the corresponding locations on the patterned interface. As can be seen, R_{min} always occurs in the vicinity of kink B regardless of the peeling direction.

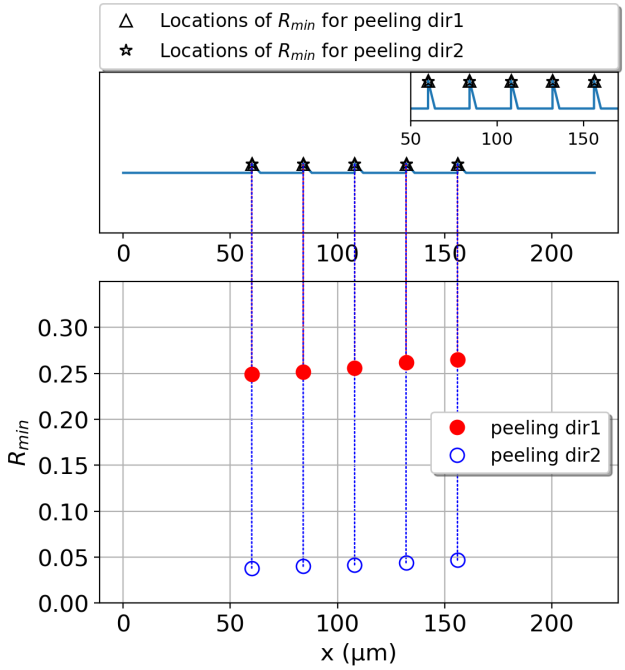

Figure 5.7: R_{min} for peeling directions 1 and 2, plotted against the apparent crack tip location where R_{min} occurs.

Despite the above qualitative similarities, especially the same locations

where R_{min} occurs, there is substantial difference in the R_{min} values. R_{min} for peeling direction 1 varies in the range of 0.25 to 0.26 while R_{min} for peeling direction 2 varies in the range of 0.038 to 0.047. The adhesion enhancement factor in patterned interface is given by Eqn.(2.29), $F = \frac{1}{R_{min}}$, and plotted in Figure 5.8 against the apparent crack tip location where R_{min} occurs. As can be seen in Figure 5.8, F is in the range of 3.8 to 4.0 for peeling direction 1 and 21.0 to 26.0 for peeling direction 2. In addition, F for peeling direction 2 have a much greater variation. The results indicate that directional adhesion is achieved, and the adhesion enhancement factors for peeling direction 2 are approximately 6 times higher than peeling direction 1. It should be pointed out that applying different values of displacement δ_0 could lead to slight difference in F values. Here, a relatively small $\delta_0 = 1\mu m$ is used to avoid highly distorted elements near the crack tip. Different displacement $\delta_0 = 2\mu m$ applied to the model in Figure 5.1 is given in Appendix B, which show the same qualitative observation as seen in Figure 5.8

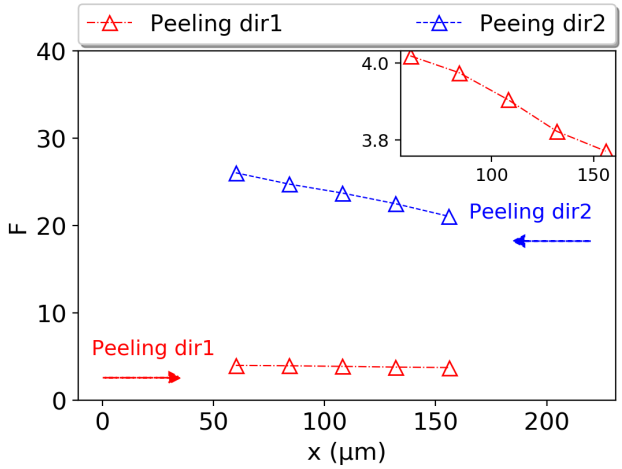

Figure 5.8: Adhesion enhancement factor F for peeling directions 1 and 2, plotted against the apparent crack tip location where R_{min} occurs. Inset is a magnified plot for peeling direction 1.

To explain the directional adhesion, we carefully investigated the regions in the vicinity of kink B in the first period where the crack tips are at B_1^+ and B_2^+ for peeling directions 1 and 2, respectively, shown in Figure 5.9(a) and (b). Here, superscript + is used to denote the location just after the

'kink' in the pattern. For example, B_1^+ refers to the location one node after B_1. Figure 5.9(c) shows the upper and lower surfaces ahead of B_1^+ in the undeformed state, denoted by S_{rd}^u and S_{rd}^l, respectively where the subscript rd indicates the ramping-down portion of the pattern. A coordinate system $\eta - \zeta$ is introduced as shown with its origin at the bottom of the vertical-up surface. Then we performed the following auxiliary simulations (Case-1a,1b and 1c) to investigate the deformation of S_{rd}^u and S_{rd}^l under several loading conditions.

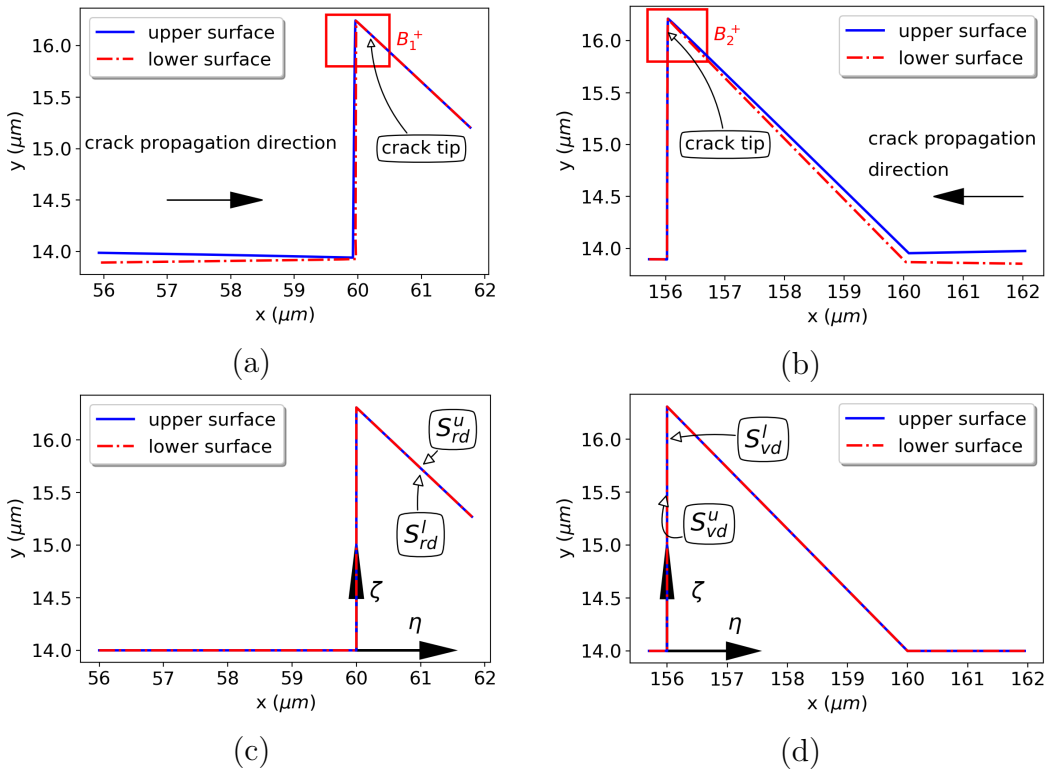

Figure 5.9: (a) and (b) are schematics of the two surfaces when the crack tips are at B_1^+ and B_2^+ where R_{min} occurs. (c) and (d) are undeformed shapes of the two surfaces in (a) and (b), respectively.

Case-1a: The displacement δ in Figure 5.2(a) is only applied to the top while the bottom edge is fixed. The crack tip is allowed to propagate from B_1 to B_1^+.

Case-1b: δ in Figure 5.2(a) is only applied to the bottom while the top edge is fixed. The crack tip is allowed to propagate from B_1 to B_1^+.

Case-1c: δ in Figure 5.2(a) is applied to both top and bottom. The crack is allowed to propagate from B_1 to B_1^+. It returns to the problem of symmetric

peeling.

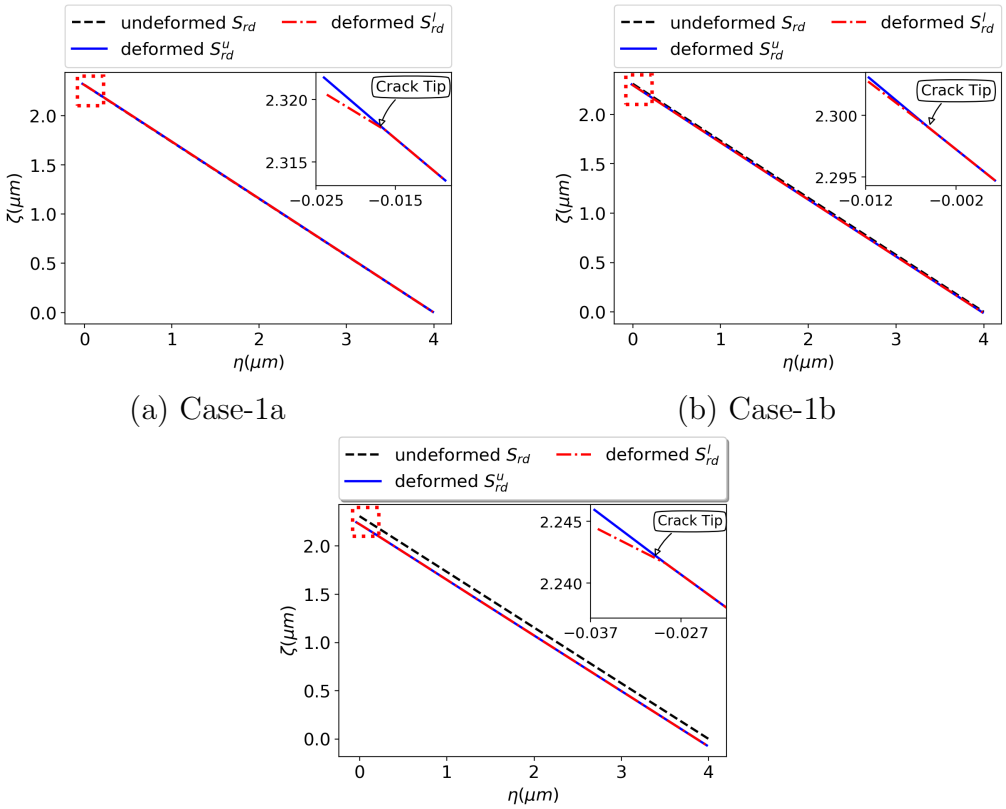

(a) Case-1a

(b) Case-1b

(c) Case-1c

Figure 5.10: Deformed and undeformed S^u_{rd} and S^l_{rd} in (a) Case-1a (b) Case-1b and (c) Case-1c.

The deformed S^u_{rd} and S^l_{rd} are shown in Figure 5.10 for the three cases, along with their undeformed shape for comparison. A region near the crack tip is enlarged in the inset of each figure. As illustrated in the enlarged inset in Figure 5.10(a), peeling the upper part alone causes S^u_{rd} to deform toward the top-right direction, i.e. away from S^l_{rd}. Hence, a separation at the crack tip is introduced. Similarly, peeling the lower part alone causes S^l_{rd} to deform toward the bottom-left direction, away from S^u_{vd}, leading to a separation at the crack tip, as illustrated in the enlarged inset in Figure 5.10(b). Hence, individual peeling of the upper and lower parts both tends to open up the crack at B_1^+ and when both parts are peeled as shown in Figure 5.10(c), the two effects combine to drive larger opening of the crack. The contribution from peeling the upper surface is greater, evidenced by the much larger crack

opening is Case-1a compared with Case-1b.

Figure 5.9(d) shows the upper and lower surfaces ahead of B_2^+ in the undeformed state for peeling direction 2. S_{vd}^u and S_{vd}^l are used to denote the upper and lower surfaces ahead of the crack tip, along the vertical-down portion of the pattern. Similarly to Figure 5.9(c), coordinate system $\eta - \zeta$ is introduced with its origin at the bottom end of S_{vd}. We again performed auxiliary simulations (Case-2a, 2b and 2c) to investigate the deformation of S_{vd}^u and S_{vd}^l under several loading conditions.

Case-2a: δ in Figure 5.2(b) is only applied to the top while the bottom edge is fixed.

Case-2b: δ in Figure 5.2(b) is only applied to the bottom while the top edge is fixed.

Case-2c: δ in Figure 5.2(b) is applied to both top and bottom. In each case, the crack tip is allowed to propagate from B_2 to B_2^+, and Case-2c returns to the problem of symmetric peeling.

The deformed S_{vd}^u and S_{vd}^l are shown in Figure 5.11 for the three cases, along with their undeformed shape for comparison. A region near the crack tip is enlarged in the inset of each figure. As illustrated in the inset of Figure 5.11(a), peeling the upper part causes S_{vd}^u to deform to the right, i.e. towards S_{vd}^l. The triangular tooth adjacent to S_{vd}^l then plays a role of resisting the deformation of S_{vd}^u. As a result, the crack between S_{vd}^u and S_{vd}^l is "closed". In Case-2b as illustrated in the inset of Figure 5.11(b), peeling the lower part causes S_{vd}^l to deform to the right, away from S_{vd}^u and opening the crack. Contrary to peeling direction 1, along peeling direction 2 loadings on the upper and lower parts have opposite effects on crack propagation. Consequently, when both parts are peeled as in Figure 5.11(c), the two effects compete leading to an overall small crack opening.

In summary, when the crack tip reaches the vicinity of kink B from different directions, peeling the upper or lower parts play different roles in the crack propagation: when the crack tip is in the vicinity of kink B_1, peeling upper and lower parts both contribute to crack propagation; when the crack tip is in the vicinity of kink B_2, peeling the lower part contributes to crack propagation

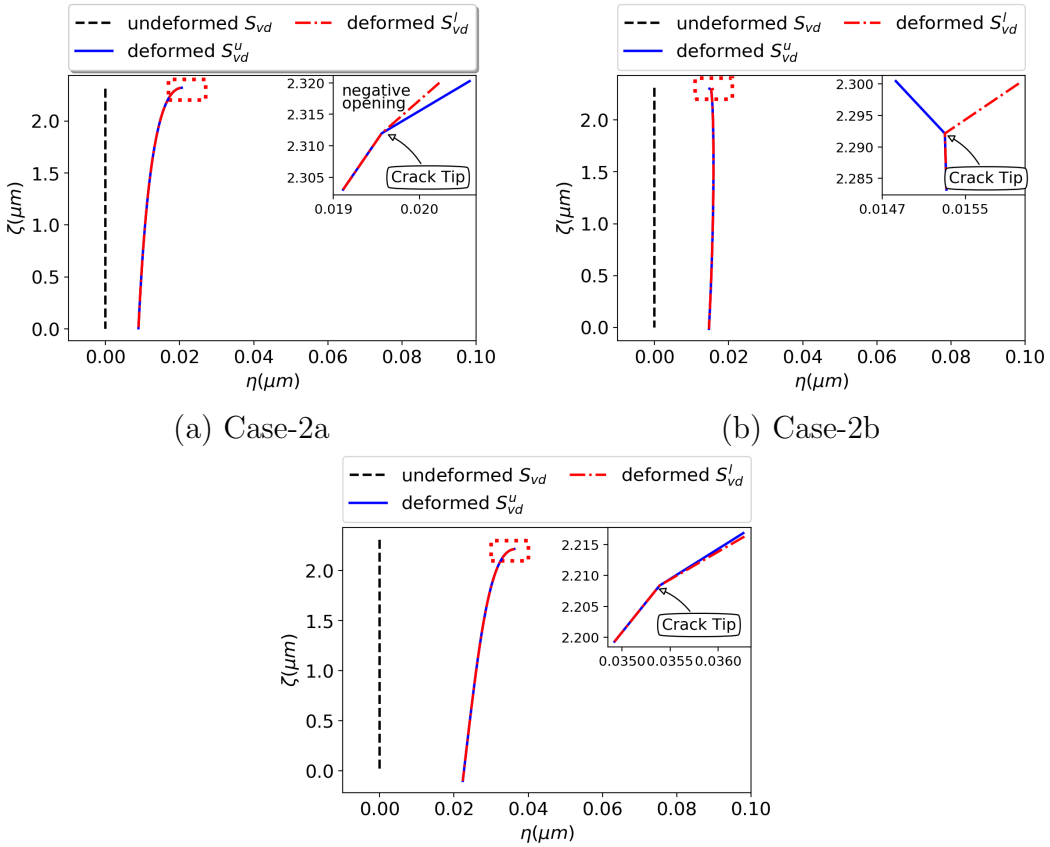

(a) Case-2a

(b) Case-2b

(c) Case-2c

Figure 5.11: Deformed and undeformed S^u_{vd} and S^l_{vd} in (a) Case-2a (b) Case-2b and (c) Case-2c.

whereas peeling the upper part contributes to crack trapping. The above analysis qualitatively explains why the R_{min} value in the vicinity of B_1 is higher than that in the vicinity of B_2.

Besides the above qualitative analysis, we also investigated the stress field ahead of the crack tips at B_1^+ and B_2^+ under the symmetric peeling condition. Figure 5.12(a) and (b) respectively show two regions in which the crack tips are at B_1^+ and B_2^+ in the first period of the pattern. The two boxed regions in Figure 5.12(a) and (b) are enlarged and shown in Figure 5.12(c) and (d). These two regions are referred to as region B_1 and region B_2, respectively. The stress field is extracted at the integration points in two elements α and β ahead of the crack tip, and then transformed according to the direction of the future crack surface, shown in Figure 5.12 (e) and (f). $1-2$ and $1^{'}-2^{'}$ are the

original and transformed coordinate systems with $1^{'}$-axis coincident with the future crack surface. The angle between $1-2$ and $1^{'}-2^{'}$ systems in regions B_1 and B_2 are -30° and 90°, respectively. Thus, the stress transformations in the two regions are given by:

In region B_1:

$$\begin{aligned} \sigma_{2'2'} &= \frac{1}{4}\sigma_{11} + \frac{3}{4}\sigma_{22} + \frac{\sqrt{3}}{2}\sigma_{12} \\ \sigma_{1'2'} &= -\frac{\sqrt{3}}{4}\sigma_{11} + \frac{\sqrt{3}}{4}\sigma_{22} + \frac{1}{2}\sigma_{12} \end{aligned} \tag{5.1}$$

In region B_2:

$$\begin{aligned} \sigma_{2'2'} &= \sigma_{11} \\ \sigma_{1'2'} &= -\sigma_{12} \end{aligned} \tag{5.2}$$

The transformed stress fields in α and β are averaged to obtain a representative stress field (denoted by superscript ave) ahead of the crack tip, given in Table 5.2. Although PDMS simulated here is hyperelastic instead of linearly elastic, an analogy can be drawn to Section 2.1.2, where among all the stress components ahead of the crack tip, $\sigma^{ave}_{2'2'}$ and $\sigma^{ave}_{1'2'}$ contribute to Mode I and II stress intensity factors, respectively, while $\sigma^{ave}_{1'1'}$ makes no contribution. As can be seen, $\sigma^{ave}_{2'2'}$ and $\sigma^{ave}_{1'2'}$ are both greater in region B_1 than in region B_2, implying greater R_{min} values in the vicinity of kink B_1 than in the vicinity of kink B_2.

Table 5.2: Stress components in elements α and β in $1-2$ and $1'-2'$ coordinate systems in regions B_1 and B_2.

Stress ($\times 10^{-3} MPa$)	α_{B_1}	β_{B_1}	α_{B_2}	β_{B_2}
σ_{11}	18.19	6.43	5.40	2.17
σ_{22}	12.35	17.48	14.28	12.35
σ_{12}	-3.35	-9.10	4.09	-4.43
$\sigma_{1'1'}$	19.63	17.08	14.28	12.35
$\sigma_{2'2'}$	10.91	6.83	5.40	2.17
$\sigma_{1'2'}$	0.85	-9.34	-4.09	4.43
$\sigma^{ave}_{1'1'}$	18.36		13.32	
$\sigma^{ave}_{2'2'}$	**8.85**		**3.785**	
$\sigma^{ave}_{1'2'}$	**-4.245**		**0.17**	

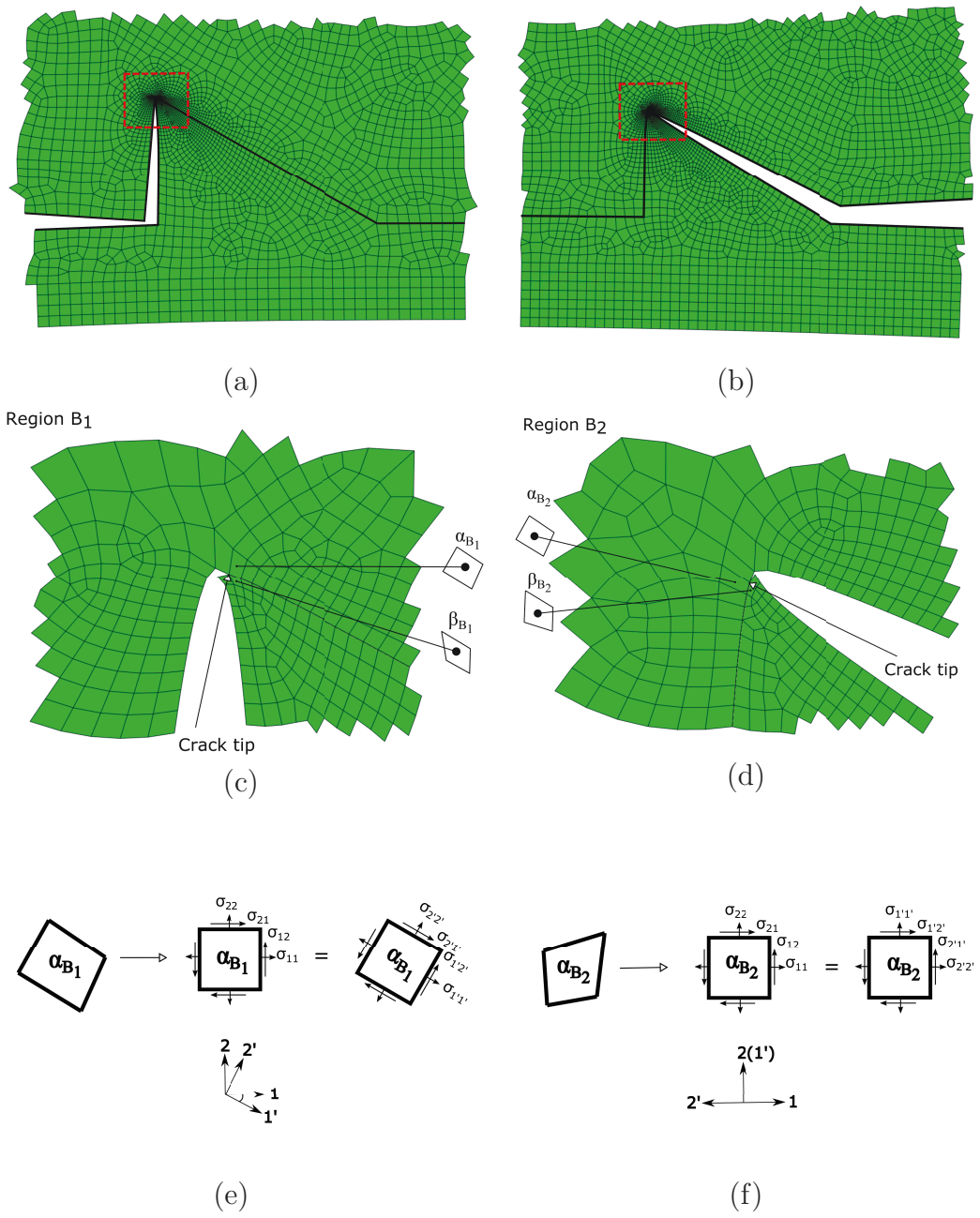

Figure 5.12: Illustration of stress analysis ahead of the crack tip, (a)(c)(e) for symmetric peeling along direction 1, and (b)(d)(f) for symmetric peeling along direction 2.

5.2 Asymmetric Peeling

This section presents the results from asymmetric peeling where the first few nodes on the top is subject to the displacement δ and the bottom edge is fixed, or vice versa. The same patterned interface and flat control models in Figure 5.1 are used. Due to the fact that the interface pattern and the loading condition are both asymmetric, four peeling directions are examined, as illustrated in Figure 5.13: by fixing the bottom and peeling the top edge, the crack propagates from left to right (peeling direction 1) or from right to left (peeling direction 2); by fixing the top and peeling the bottom edge, the crack propagates from left to right (peeling direction 3) or from right to left (peeling direction 4).

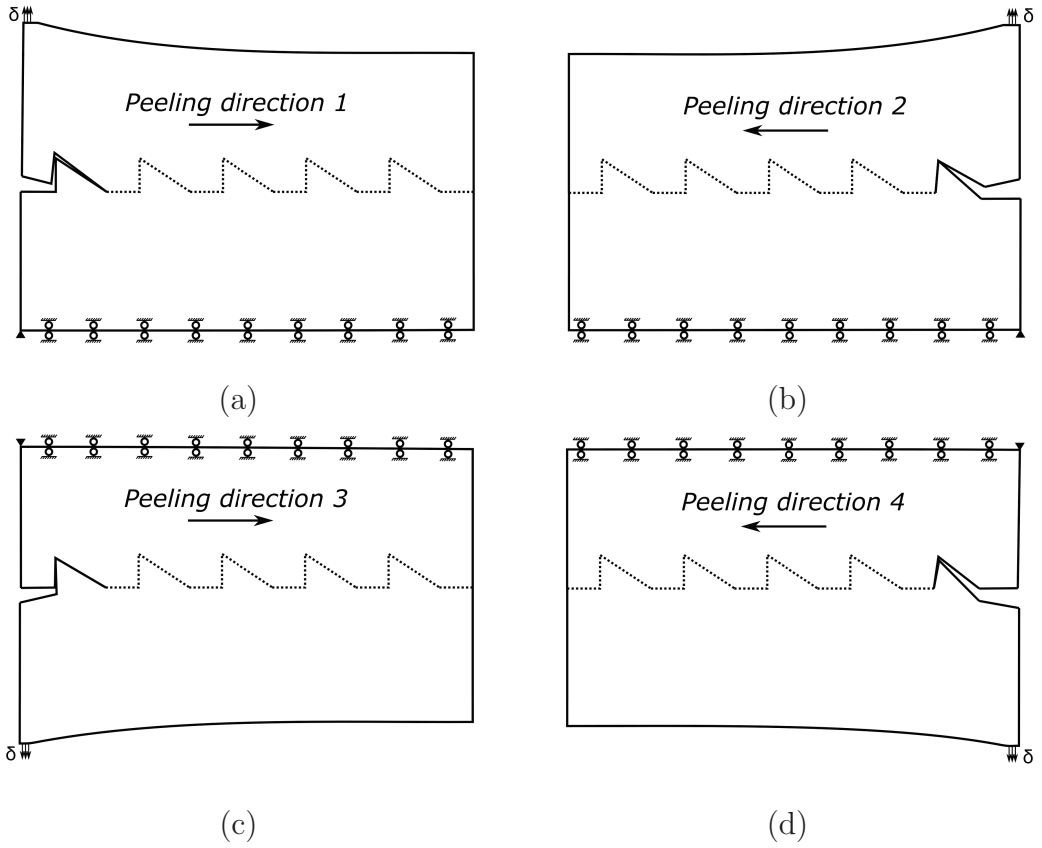

Figure 5.13: Schematics of asymmetric peeling (a) direction 1, (b) direction 2 (c) direction 3, (d) direction 4.

Figure 5.14(a) and (b) shows the schematics of the interface as the crack propagates in peeling directions 1 and 2. Figure 5.14(c)(d) and (e)(f) show

how R changes with the apparent crack tip location x and the actual crack tip location a in the two cases. The corresponding results for peeling directions 3 and 4 are shown in the left and right panels of Figure 5.15, respectively.

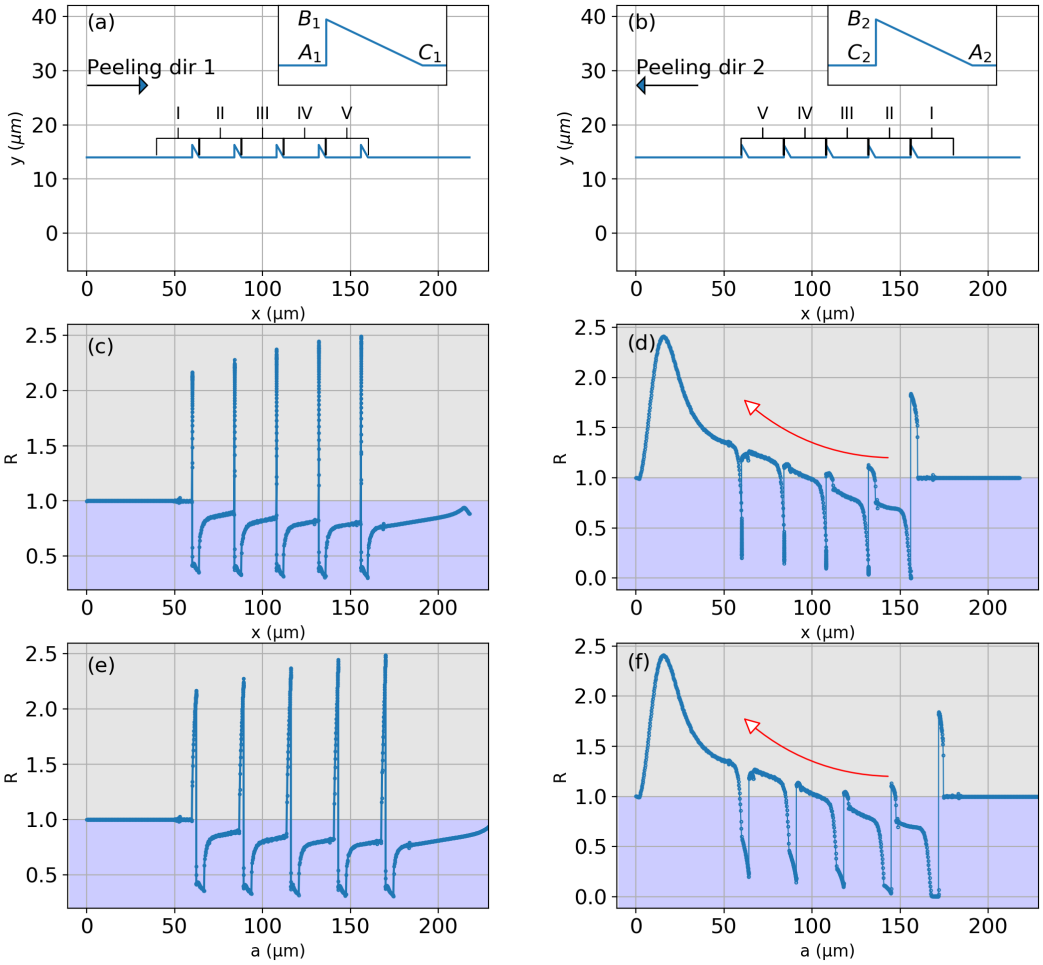

Figure 5.14: Energy release rate ratio R for the two different peeling directions, left panel: peeling direction 1; right panel: peeling direction 2. (a) and (b) are schematics of the interface. (c) and (d) are R versus the apparent crack tip location x. (e) and (f) are R versus the actual crack tip location a.

Upon examining the figures, one similarity among the results from the four peeling directions is the discontinuities in the R curve at 'kinks' where the crack propagation changes direction. On the other hand, more differences can be observed. Firstly, R curves for peeling directions 1 and 4 show periodic patterns, i.e., the range of variation in R is approximately the same for different periods. But this does not hold for peeling directions 2 and 3. For these two

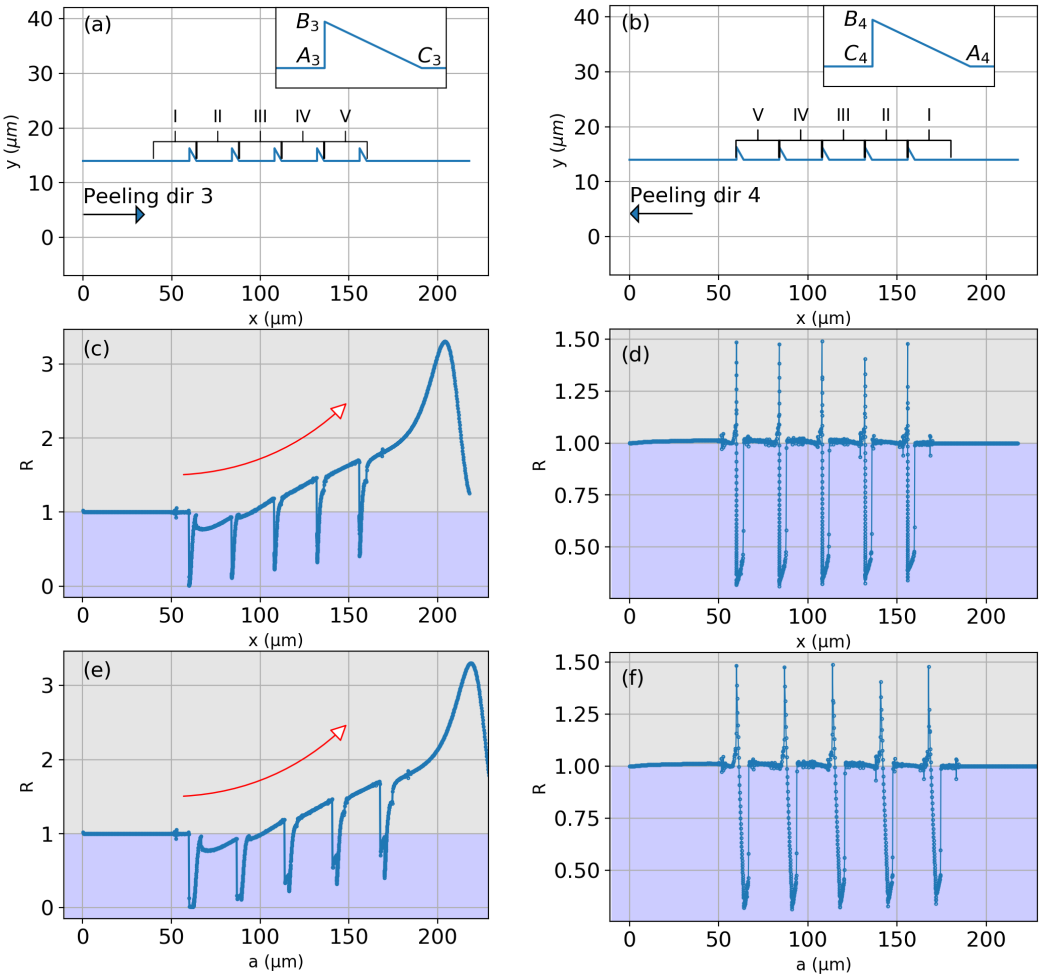

Figure 5.15: Energy release rate ratio R for the two different peeling directions, left panel: peeling direction 3; right panel: peeling direction 4. (a) and (b) are schematics of the interface. (c) and (d) are R versus the apparent crack tip location x. (e) and (f) are R versus the actual crack tip location a.

directions, there is an ascending trend in the R curves indicated by the red arrows in Figure 5.14(d)(f) and Figure 5.15(c)(e).

To explain this observation, Figure 5.16(a) shows the schematic of the two interfaces when the crack tip accesses period II in peeling direction 2. Figure 5.16(b) enlarges the boxed region in Figure 5.16(a). Superscripts u and l are used to distinguish the 'kinks' on the upper and lower surfaces. Figure 5.16(c) shows the same enlarged region but is an image from ABAQUS, with the σ_{11} distribution. Clearly, the upper part is bent and the contact in compression between corner C_2^u and surface $B_2^l C_2^l$ results in stress concentration in the

highlighted region in Figure 5.16(b), indicated by the negative σ_{11} distribution in the same region in Figure 5.16(c). This leads to a considerable amount of strain energy stored in the model. As the crack further advances, the compressive contact between C_2^u and $B_2^l C_2^l$ becomes weaker, and the stored strain energy is released, giving rise to the ascending trend in the R curve. Likewise, in the case of peeling direction 3 as illustrated in Figure 5.17, the contact between B_3^l and $A_3^u B_3^u$ gives rise to the ascending trend in the R curve. The ascending trend was not observed in cases of peeling directions 1 and 4 because under those loading conditions the vertical surfaces separate and there are no compressive contacts between them causing additional stored strain energy.

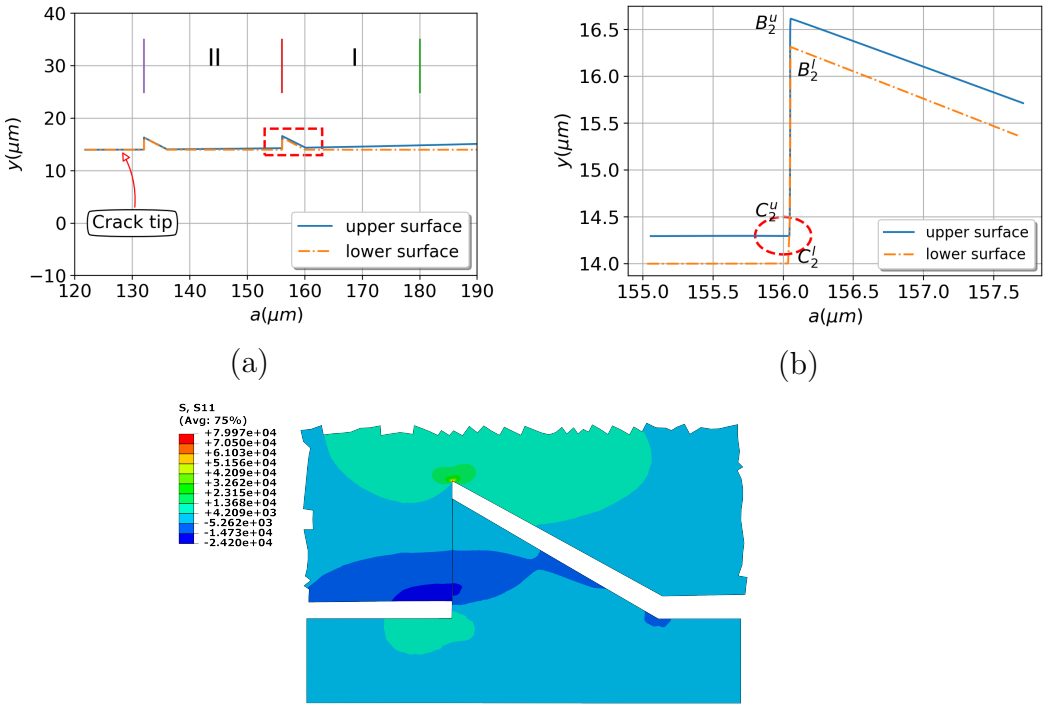

Figure 5.16: (a) Schematics of the interface in peeling direction 2 as the crack tip accesses period II. (b) enlarged view of the boxed region in (a). (c) the same enlarged region from ABAQUS with the σ_{11} stress distribution.

Another difference observed is R_{min} for the four peeling directions occur at different locations (as opposed to symmetric peeling where R_{min} for both

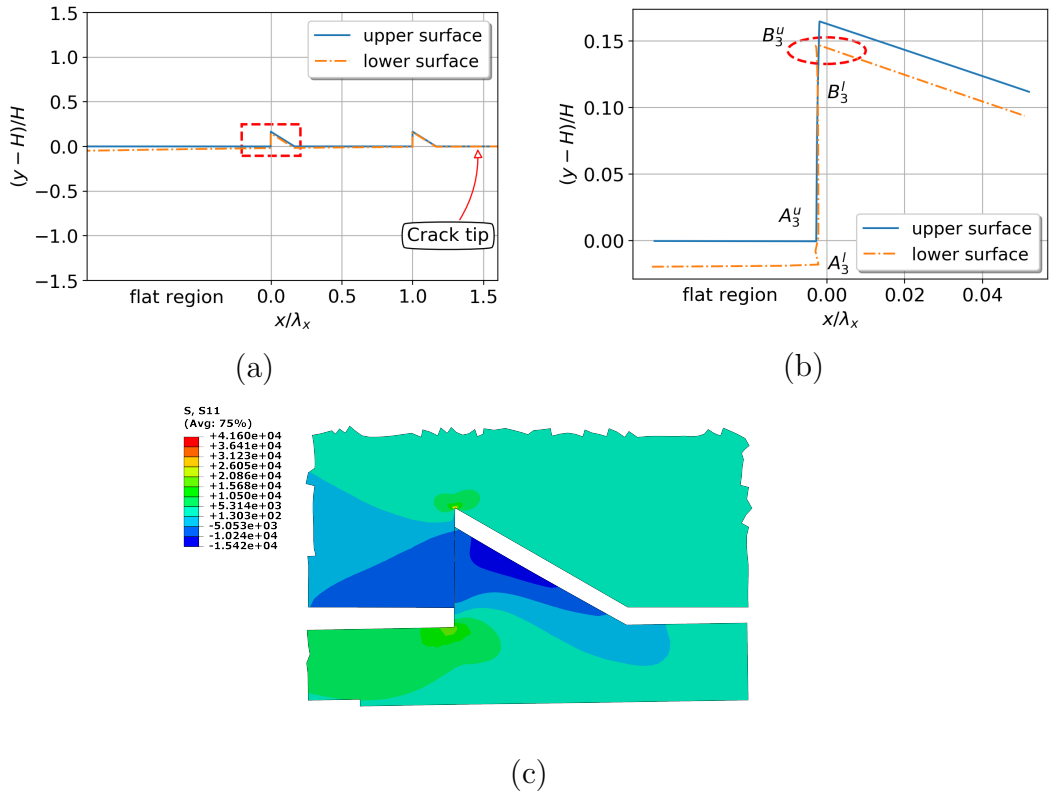

Figure 5.17: (a) Schematic of the interface in peeling direction 3 as the crack tip accesses period II. (b) enlarged view of the boxed region in (a). (c) the same enlarged region from ABAQUS with the σ_{11} stress distribution.

peeling directions occur at the same locations). As Figure 5.18 illustrates, R_{min} for peeling direction 1 always occur in the vicinity of kink C while those for the other 3 peeling directions occur in the vicinity of kink B. The last difference is the different R_{min} values for the four peeling directions. The adhesion enhancement factor $F(=\frac{1}{R_{min}})$ for the four peeling directions are shown in Figure 5.19. F for peeling direction 1 varies from 2.8 to 3.3 while that for peeling direction 2 varies in the large range of 5.0 to 312; F for peeling direction 3 varies from 2.5 to 70 while the range for peeling direction 4 is narrow, from 3.0 to 3.1. The results indicate that directional adhesion is achieved via different peeling directions. Particularly, F for peeling directions 2 and 3 can reach remarkable values in the first period, although the values decrease with crack length and can eventually become comparable to or even lower than those in peeling directions 1 and 4. By contrast, F for peeling

directions 1 and 4 are fairly low but steady as the crack tips propagate through the entire interface.

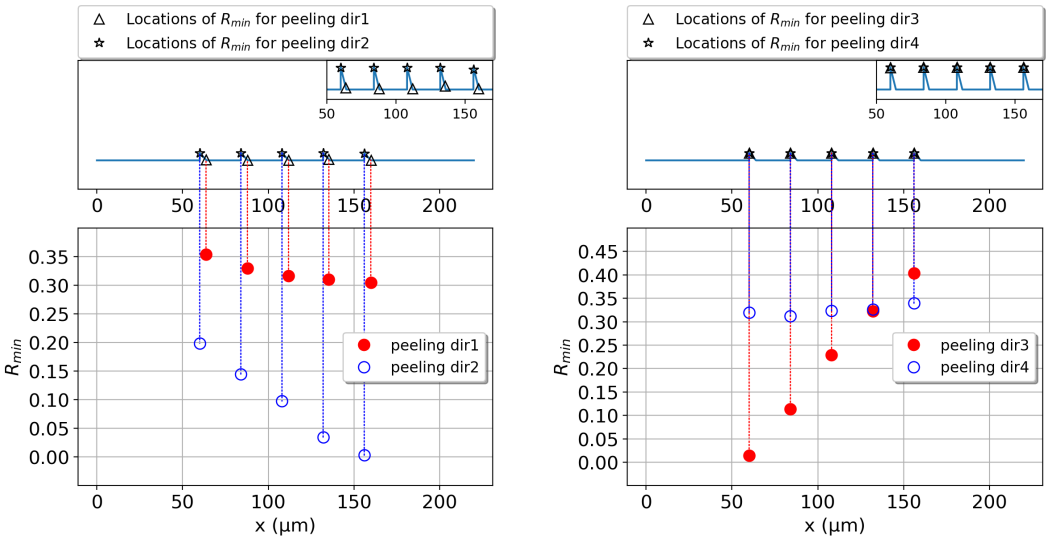

(a) (b)

Figure 5.18: R_{min} for peeling directions (a) 1 and 2, (b) 3 and 4 plotted against the apparent crack tip locations where R_{min} occurs.

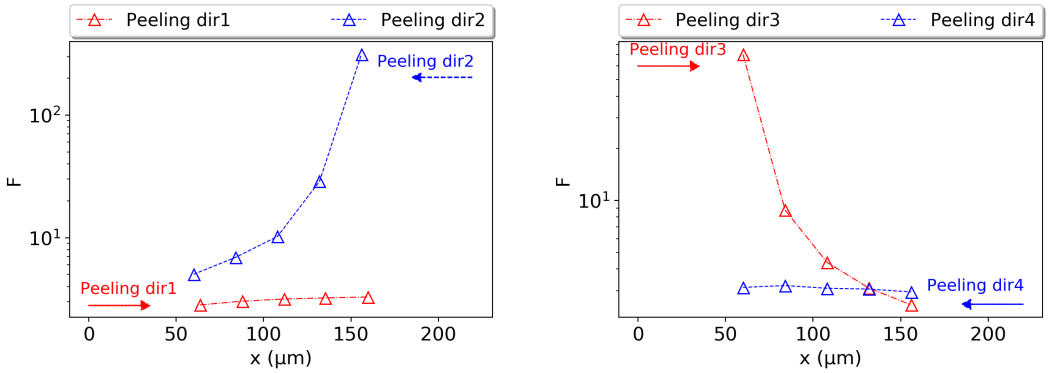

(a) (b)

Figure 5.19: Adhesion enhancement factor F for (a) peeling directions 1 and 2 and (b) peeling direction 3 and 4, plotted against the apparent crack tip locations where R_{min} occurs.

5.3 Pulling

This section presents the results from the pulling condition where the top boundary is subject to a uniformly distributed displacement δ and the bottom edge is fixed. The same patterned interface and flat control models in Figure 5.1 are used. Two pulling directions are examined: the crack propagate from left to right (pulling direction 1) and from right to left (pulling direction 2), as shown in Figure 5.20.

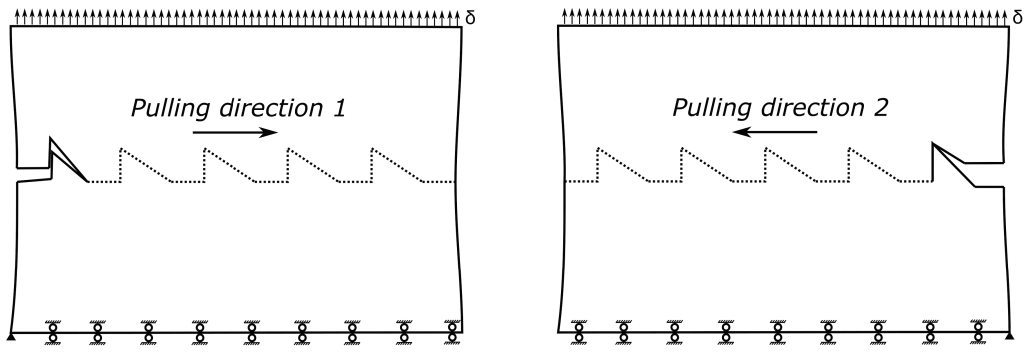

(a) (b)

Figure 5.20: Schemetics of (a) pulling direction 1 and (b) pulling direction 2

Figure 5.21(a) and (b) shows schematics of the interface as the crack propagate on the triangular interface in pulling directions 1 and 2. Figure 5.21(c)(d) and (e)(f) show how R changes with the apparent crack tip location x and actual crack tip location a, respectively. Several similarities can be observed between the results from the two pulling directions. Firstly, R curves again show discontinuities at "kinks" where the crack propagation direction changes. Secondly, R in the first flat region is constant and equal to 1, whereas in later periods it deviates from 1 in the triangular regions but approaches 1 as the crack tip moves away from the "kinks".

Despite the above similarities, several differences can be observed. Firstly, R_{min} for peeling direction 1 occur in the vicinity of kink B_1 while those for peeling direction 2 occur in the vicinity of kink C_2, as Figure 5.22 illustrates. Secondly, there is a small quantitative difference in the R_{min} values. Figure 5.23 shows the adhesion enhancement factor F for the two pulling directions.

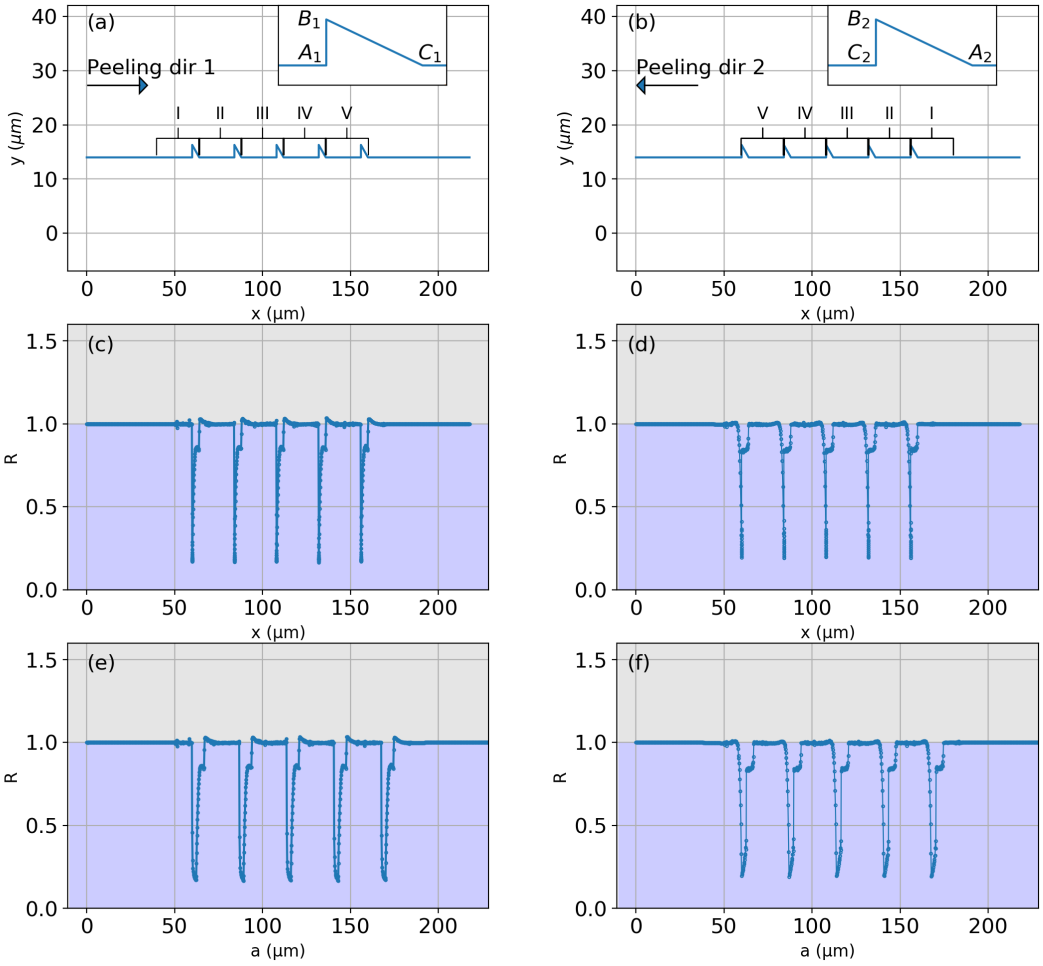

Figure 5.21: Energy release rate ratio R for the two different pulling directions with frictionless constraint on the fixed edge, left panel: pulling direction 1; right panel: pulling direction 2. (a) and (b) are schematics of the interface. (c) and (d) are R versus the apparent crack length x. (e) and (f) are R versus the actual crack length a.

F for pulling direction 1 ranges from 5.8 to 6.0 while that for pulling direction 2 varies between 5.0 and 5.2. Comparing this plot to Figure 5.8 and 5.19, the directional adhesion achieved under pulling is much weaker. The variation of F with the apparent crack tip location is also much smaller for each direction because of the more periodic R_{min} curves. F under both pulling conditions have values higher than the theoretical value predicted by Eqn.(2.30):

$$F = \frac{1}{R_{min}} = 1/\cos^4(\frac{\theta_{max}}{2}) = 1/\cos^4(\frac{90^\circ}{4}) = 4$$

where $\theta_{max} = 90^\circ$ is the angle between the future crack surface and the hori-

zontal at locations where R_{min} occurs. Recall from Section 2.4, the derivation of Eqn(2.30) is based on two strong assumptions: 1) the crack is embedded in an infinite body and 2) the surface before the crack tip is horizontal. In our case, however, the model is of finite size and the surface before the crack tip locations where R_{min} occurs is not horizontal. The violations of the assumptions lead to the discrepancy between our FE results and Eqn(2.30), which states R_{min} only depends on the largest angle of the interface from the horizontal regardless of the crack propagation direction.

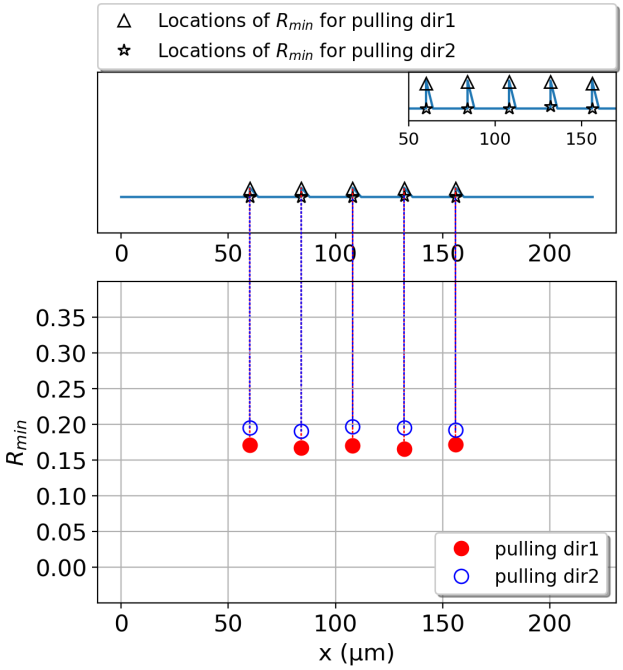

Figure 5.22: R_{min} for pulling directions 1 and 2, plotted against the apparent crack tip locations where R_{min} occurs.

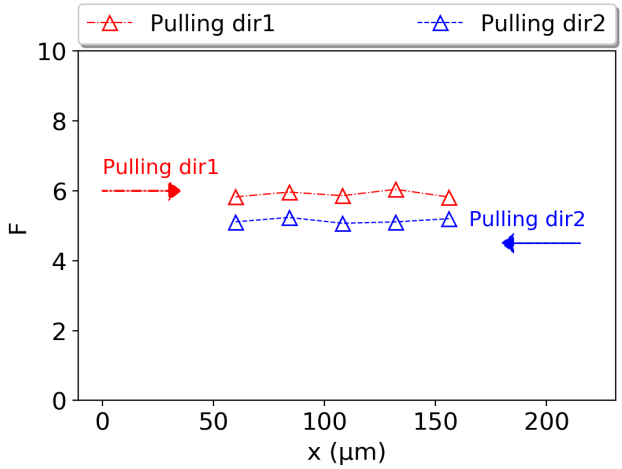

Figure 5.23: Adhesion enhancement factor F for pulling directions 1 and 2, plotted against the apparent crack tip locations where R_{min} occurs.

Chapter 6

Parametric Study

In this chapter, the effects of geometrical parameters in a triangular patterned interface (Figure 5.1) on the adhesion enhancement and directional adhesion are investigated. Three non-dimensional ratios are chosen for this study: H/l, h/l, and s/L. H/l represents a relative size of the bulk sample with respect to the pattern, h/l captures the influence of angle θ since $\tan(\theta) = h/l$, while s/L represents the "density" of the triangles on the interface. Symmetric peeling as defined in Figure 3.3(c) is applied in all cases, and both peeling directions 1 and 2 are considered.

6.1 Effect of H/l

Models with different H/l values are simulated with FEA, where the apparent length of the model (L), the lengths of the horizontal and vertical sides of the triangular teeth (l and h), and the length of the flat region (s) (refer to Figure 5.1) are kept the same as in Table 5.1. The thickness H is varied from 14 μm to 20 μm to obtain four different H/l values, as shown in Table 6.1.

Table 6.1: Parameters for investigating the effect of H/l.

parameter	value			
$H(\mu m)$	14	16	18	20
$l(\mu m)$	4	4	4	4
H/l	3.5	4	4.5	5

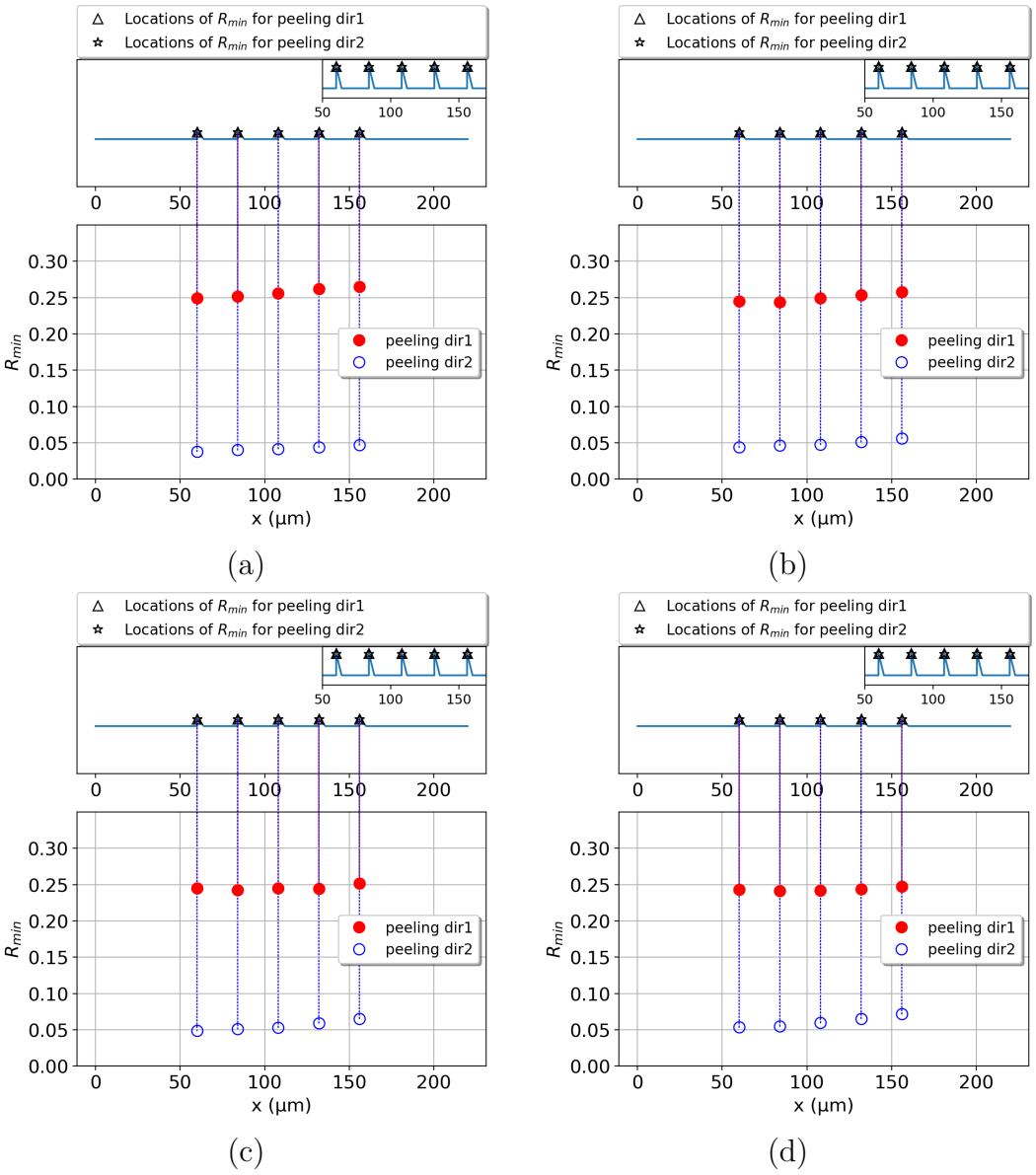

Figure 6.1: R_{min} and the corresponding locations on the interface for H/h = (a) 3.5, (b) 4, (c) 4.5, and (d) 5.

Figure 6.4 shows R_{min} plotted against the apparent crack tip location, as well as the corresponding locations on the interface for all H/l values. As can be seen, R_{min} always occurs in the vicinity of B (see Figure 5.1 for its definition) regardless of the value of H/l. Figure 6.2 shows F versus the apparent crack tip locations where R_{min} occurs. F for peeling direction 1 is generally lower than that for peeling direction 2, and is insensitive to the change of H/l. The slight increases in F as H/l increases can be seen from the

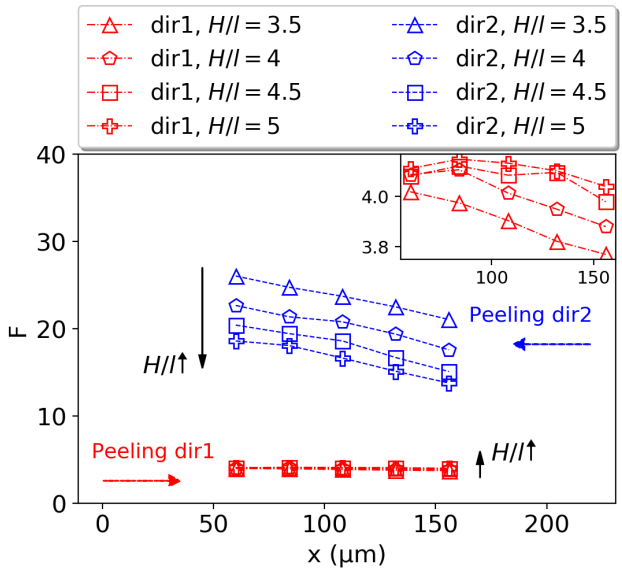

Figure 6.2: Adhesion enhancement factor F plotted against the apparent crack tip locations where R_{min} occurs. The inset plots enlarged region for F along direction 1.

enlarged inset in Figure 6.2. On the other hand, there is a notable decrease in F with increasing H/l if the crack propagates along direction 2. As a result, direction adhesion becomes weaker with increasing H/l. For example, at $x = 108\ \mu m$ F for peeling direction 2 is ~ 6 times higher for $H/l = 3.5$ but ~ 4 times higher for $H/l = 5$.

To understand the above observation, the FEA model is partitioned into an "interface" region and a "bulk" region, as shown in Figure 6.3. Here, the interface region ranges from $1\mu m$ above the top of the teeth to $1\mu m$ below the bottom of the teeth. Following the definition in Eqn 3.3, $G_{pattern}$ can now be written as:

$$\begin{aligned} G_{pattern} &= \frac{U_{bulk}(a) + U_{intf}(a) - U_{bulk}(a+\Delta a) - U_{intf}(a+\Delta a)}{\Delta a} \\ &= \underbrace{\frac{U_{bulk}(a) - U_{bulk}(a+\Delta a)}{\Delta a}}_{G_{bulk}} + \underbrace{\frac{U_{intf}(a) - U_{intf}(a+\Delta a)}{\Delta a}}_{G_{intf}} \end{aligned} \tag{6.1}$$

where the subscripts "bulk" and "intf" respectively stand for the bulk and the interface. Although the partition of the model is somewhat arbitrary, G_{intf} and G_{bulk} roughly capture the relaxation of the materials, upon crack

propagation, near the interface and away from the interface. Both are affected by the patterns on the interface and the overall geometry of the model. Then the local minima of the energy release rate ratio R_{min} can be written as:

$$R_{min} = \underbrace{\frac{G_{bulk}}{G_{flat}}(x_i)}_{R_{min,bulk}} + \underbrace{\frac{G_{intf}}{G_{flat}}(x_i)}_{R_{min,intf}}, i = 1, 2, ..., N \tag{6.2}$$

Here x_i are the apparent crack tip locations where R_{min} occurs and N is the total number of minima.

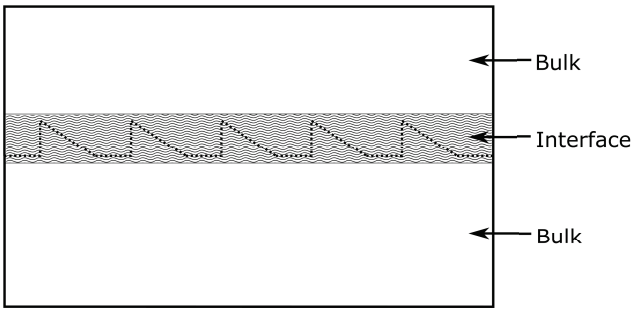

Figure 6.3: Schematic of bulk and interface partition

Figure 6.4(a) and (b) respectively show $R_{min,intf}$ and $R_{min,bulk}$ for the four H/l values and two peeling directions. Along peeling direction 1, as H/l increases $R_{min,bulk}$ increases while $R_{min,intf}$ decreases. This is due to the increase in the volume fraction of the bulk so that G_{bulk}/G_{flat} increases and G_{intf}/G_{flat} decreases. It is also clear that the changes in $R_{min,bulk}$ and $R_{min,int}$ are of similar magnitude, which together with the opposite trend leads to the insensitivity of F to H/l along direction 1.

Along peeling direction 2, as H/l increases again $R_{min,bulk}$ increases while $R_{min,intf}$ decreases. However, different from direction 1 the change is small for $R_{min,intf}$ but larger for $R_{min,bulk}$. This results in R_{min} following the same trend as that of the bulk. Interestingly, $R_{min,intf}$ along direction 2 at each location is negative, i.e., $G_{intf} < 0$, indicating more stored energy as crack propagates. This is due to the large deformation that takes place at the teeth when the crack tip is near B, which is found insignificant along direction 1 but significant along direction 2 (see Section 5.1). The negative value of $R_{min,intf}$ contributes

to the small magnitude of R_{min} and hence more sensitivity of $F(=\frac{1}{R_{min}})$ to H/l.

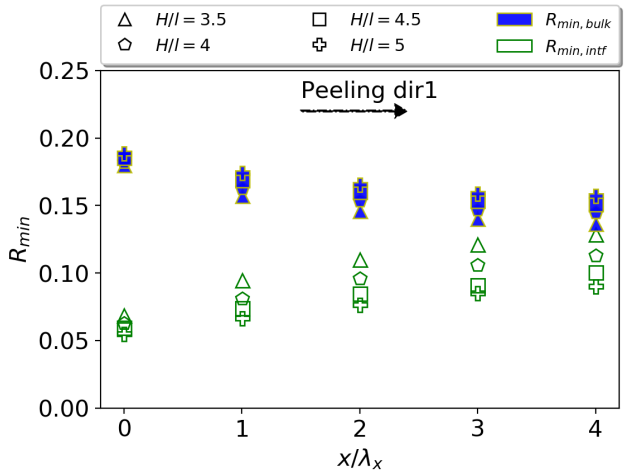

(a)

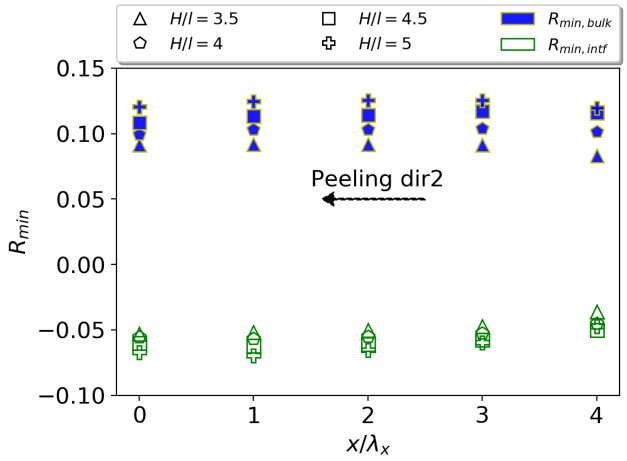

(b)

Figure 6.4: $R_{min,bulk}$ and $R_{min,intf}$ plotted against the apparent crack tip location for peeling directions (a) 1 and (b) 2.

6.2 Effect of θ

In this section, the global dimensions of the model (L, H), and the length of the horizontal side of triangular teeth (l) are kept the same as in Table 5.1, while the vertical side of the teeth (h) is varied from 1.54 to 2.80 to obtain four different h/l values, corresponding to $\theta = 20°, 25°, 30°$ and $35°$, as shown in Table 6.2.

Table 6.2: Parameters for investigating the effect of θ.

parameter	value			
$h(\mu m)$	1.46	1.87	2.31	2.80
$l(\mu m)$	4	4	4	4
$\theta(°)$	20	25	30	35

Figure 6.5 shows R_{min} versus the apparent crack tip location and the corresponding locations on the interface for the four θ values. As can be seen, the locations of R_{min} is always near kink B regardless of the value of θ. The adhesion enhancement factor F for each θ value is plotted in Figure 6.6 against the apparent crack tip location where R_{min} occurs. F for peeling direction 2 is generally higher than that for peeling direction 1. Besides, F for both peeling directions increase with increasing θ while F for peeling direction 2 is more sensitive to θ. As a result, directional adhesion becomes stronger as θ increases. For example, at $x = 60\mu m$ F for peeling direction 2 is approximately 4.1 times higher for $\theta = 20°$ and 7.5 times higher for $\theta = 35°$.

To explain the above observations, we carefully investigated the regions in the vicinity of B in the first period where the crack tips are at B_1^+ and B_2^+ respectively for peeling directions 1 and 2 (see Figure 5.9 for the definitions of points B_1^+ and B_2^+). Similar to Section 5.1, three auxiliary simulations are performed to investigate the deformation of the upper and lower surfaces under three loading conditions: peeling only the top surface, only the bottom surface, or both. The deformed S_{rd}^u and S_{rd}^l are shown in Figure 6.7 for peeling direction 1, along with their undeformed shapes for comparison. Similarly, the deformed S_{vd}^u and S_{vd}^l are shown in Figure 6.8 for peeling direction 2, along

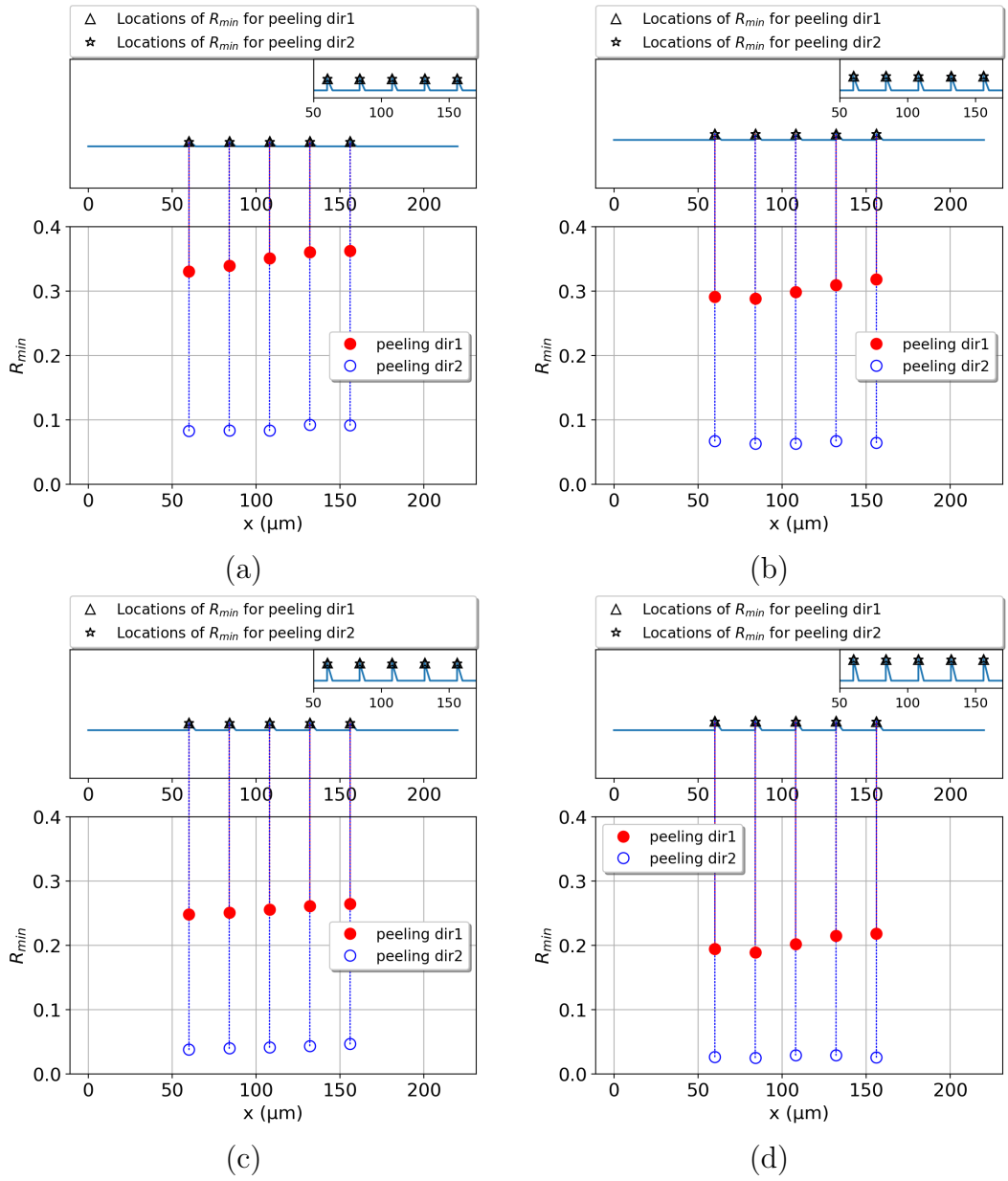

Figure 6.5: R_{min} plotted against the apparent crack tip locations where R_{min} occurs. θ = (a) 20°, (b) 25°, (c)30°,(d) 35°.

with the undeformed shapes. Figure 6.9 shows $G_{pattern}$ evaluated at B_1^+ and B_2^+ under symmetric peeling, plotted against the four θ values.

As discussed in Section 5.1, when the crack tip is at B_1^+, peeling either the upper or lower part contributes to crack propagation and the contribution from peeling the upper part is greater. Upon examining Figure 6.7(a), the crack opening before the crack tip decreases monotonically with increasing

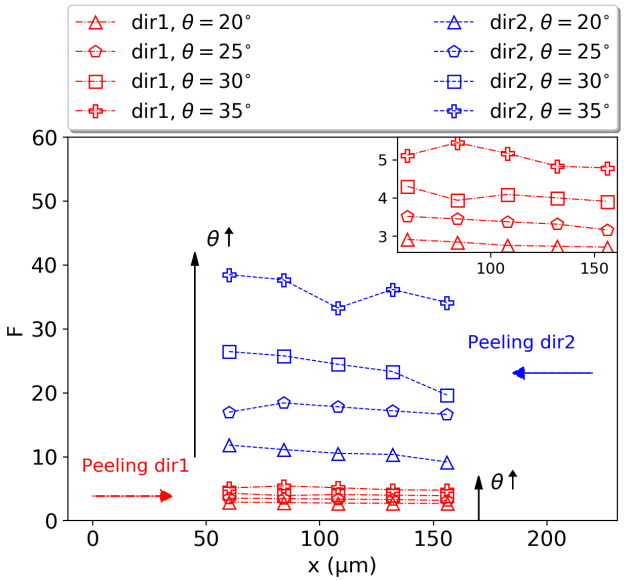

Figure 6.6: Adhesion enhancement factor F, plotted against the apparent crack tip locations where R_{min} occurs.

θ. Similarly, when the lower part is peeled, increasing θ also decreases crack opening as shown in Figure 6.7(b), although the crack openings are much smaller than those obtained by peeling the upper part. The dominant role of peeling the upper part is seen in Figure 6.7(c) where the crack opening under symmetric peeling also decreases monotonically with increasing θ, which is consistent with the trend of $G_{pattern}$ represented by the dashed cyan line in Figure 6.9.

Also discussed in section 5.1, when the crack tip is at B_2^+, peeling the lower part contributes to crack propagation whereas peeling the upper part contributes to crack-trapping. This is confirmed by examining Figure 6.8 where peeling only the upper part causes S_{vd}^l to penetrate into S_{vd}^u, and peeling only the lower part causes S_{vd}^l and S_{vd}^u to separate. In addition, in Figure 6.8(b) the crack opening decreases considerably with increasing θ. The dominant role of peeling the lower part can be seen from Figure 6.8(c) where the crack opening under symmetric peeling also decreases monotonically with increasing θ, which is consistent with the trend of $G_{pattern}$ represented by the dashed blue line in Figure 6.9. Furthermore, the crack trapping effect caused by peeling the upper part contributes to the small magnitude of $G_{pattern}$ along direction

2 and hence more sensitivity of F to θ.

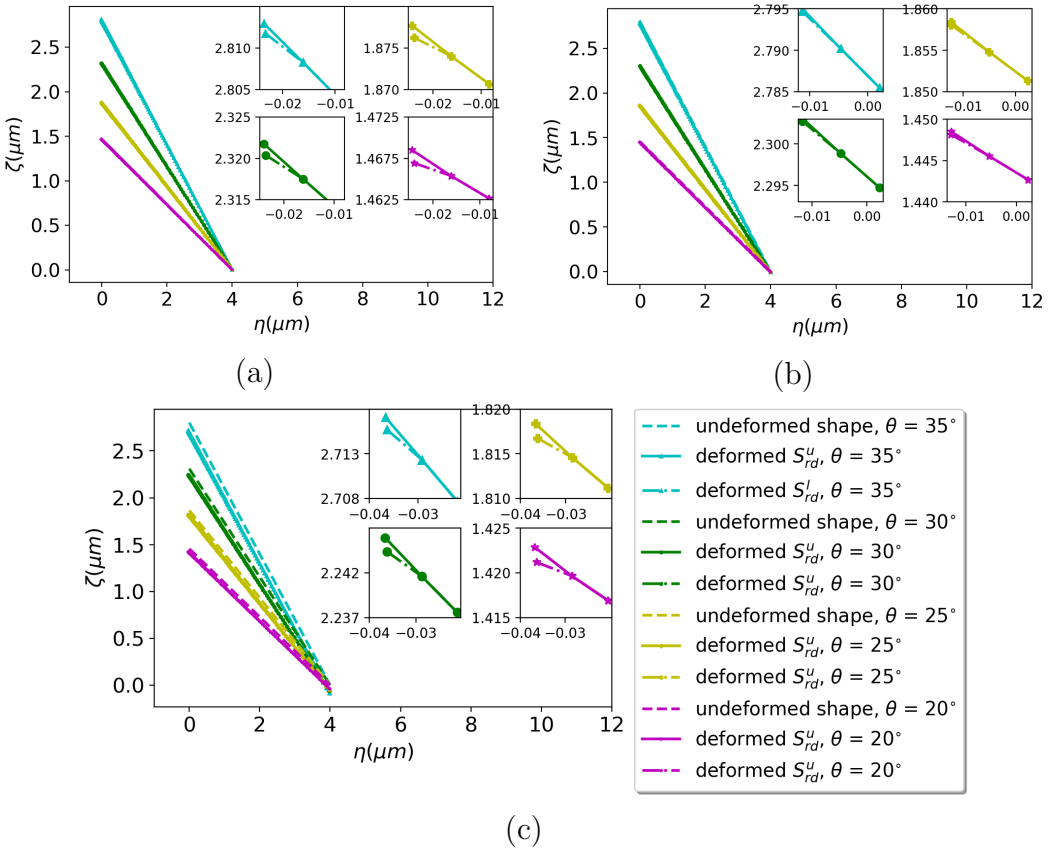

Figure 6.7: Deformations of S^u_{rd} and S^l_{rd} with their undeformed shapes for peeling (a) only the upper part, (b) only the lower part and (c) both, along direction 1.

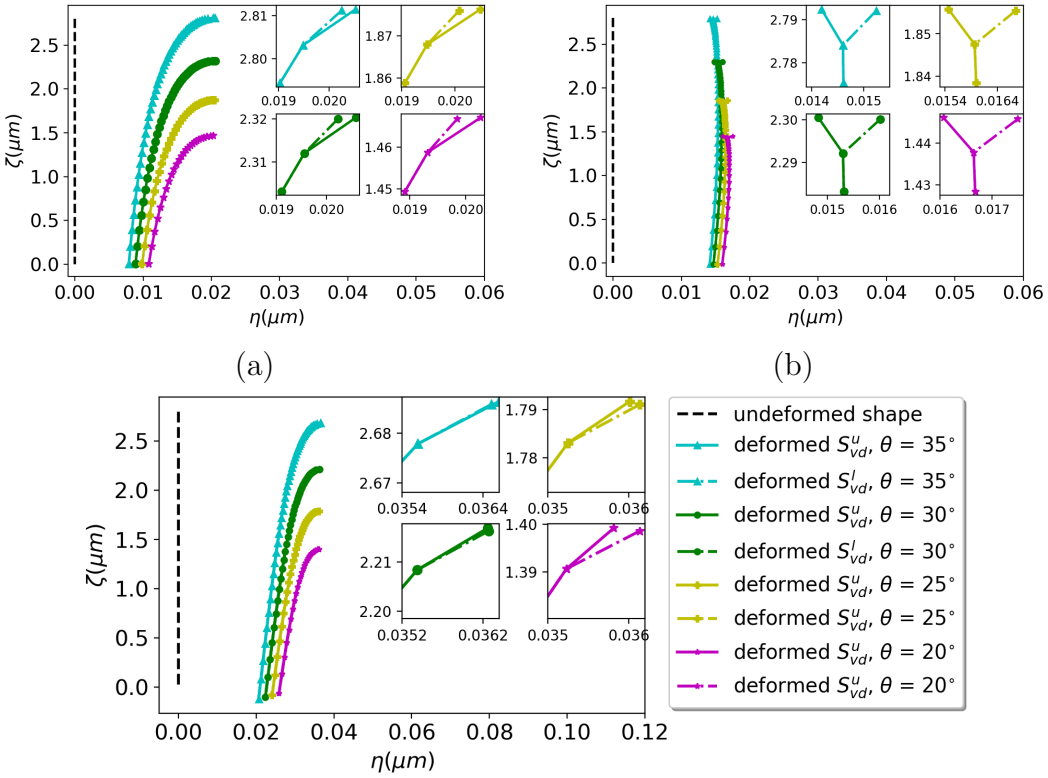

Figure 6.8: Deformations of S^u_{vd} and S^l_{vd} with their undeformed shapes for peeling (a) only the upper part, (b) only the lower part and (c) both, along direction 2.

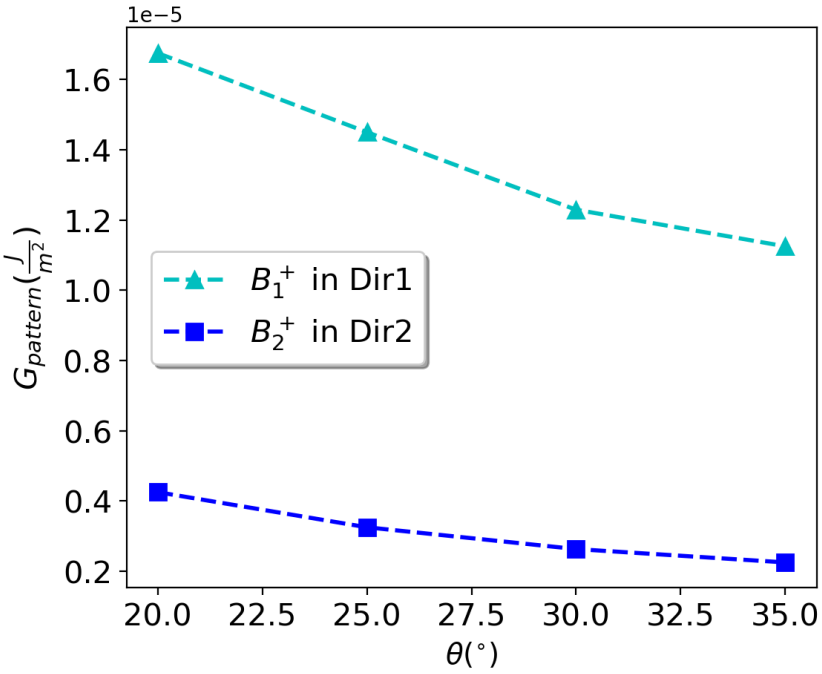

Figure 6.9: $G_{pattern}$ at B_1^+ and B_2^+ under symmetric peeling in directions 1 and 2 respectively, plotted against θ.

6.3 Effect of s/L

In this section, models with different s/L values are simulated in FEA, where the global dimensions of the model (L, H), the lengths of the horizontal and vertical sides of the triangular teeth (l, h) are kept the same as in Table 5.1. The length of the flat regions in the patterned region (s) is varied from $20\mu m$ to $92\mu m$ to obtain four different s/L values, corresponding to 5, 4, 3 and 2 teeth within the same apparent length of the model as shown in Table 6.3.

Table 6.3: Parameters for investigating the effect of s/L.

parameter	value			
$s(\mu m)$	20	28	44	92
$L(\mu m)$	220	220	220	220
s/L	0.09	0.13	0.2	0.42
Total number of teeth	5	4	3	2

Figure 6.10 shows R_{min} and the corresponding locations on the interface for the four s/L values. As can be seen, R_{min} always occurs in the vicinity of B (see Figure 5.1 for the definition of point B) regardless of the value of s/L. Figure 6.11 shows F versus the apparent crack tip locations where R_{min} occurs. Along peeling direction 1, F has little dependence on s/L and all data collapse onto one curve, with slight decreases in value as s/L increases. The observation is quite different along peeling direction 2. At the first teeth, F is the same for the four different s/L values. This is expected as the presence of the teeth ahead of the crack tip has not been felt yet. As the crack further propagates, F becomes different and shows trend of increasing as s/L increases. As a result, directional adhesion becomes stronger as s/L increases. For example, at $x = 60\mu m$ F in direction 2 is approximately 6.5 times higher for $s/L = 0.09$ but 7.4 higher for $s/L = 0.2$.

To explain the dependence of F on s/L along peeling direction 2, we note that as the crack propagates through the interface, near the crack tip the deformation of the upper part is smaller than that of the lower part. This is caused by the deformation of the triangular teeth in the cracked region which

makes it difficult for the externally applied displacement to be propagated to the crack tip. Evidence for this can be seen in Figure 6.12, which contains colored contour maps for the magnitude of the displacement in the vertical direction for different s/L. For comparison, Figure 6.12(e) shows the corresponding contour plot for a flat interface. All the cracks shown in Figure 6.12 have the same apparent length, and the same color bar is used in all plots. Δ is the distance between the right boundaries of the darkblue color bands on the upper and lower parts. As can be seen, Δ is zero in the flat control indicating the same deformation in the two parts. As s/L decreases and the number of teeth increases, Δ increases, suggesting deviation in deformation of the two parts. In fact, by comparison with the flat control, it can be seen that as s/L decreases, the deformation in the lower part is promoted while the deformation in the upper part is suppressed. Similar plots are shown in Figure 6.13 for peeling direction 1, where similar observations can be seen as in Figure 6.12, and the uneven deformation is more significant indicated by the larger Δ values.

Recall from Section 5.1, along direction 2 peeling the lower part contributes to crack propagation whereas peeling the upper part contributes to crack trapping. Thus, as s/L decreases the smaller deformation of the upper part will result in less "crack trapping" and the larger deformation of the lower part will promote propagation. This consequently leads to larger $G_{pattern}$ and smaller F. Also discussed in Section 5.1, along direction 1 peeling upper or lower part both contributes to crack propagation. Thus, as s/L decreases the smaller deformation of the upper part will result in less contribution, which is compensated by the promoted contribution to crack propagation by the larger deformation of the lower part. Thus, the dependence of F on s/L along direction 1 is much smaller compared to that along direction 2.

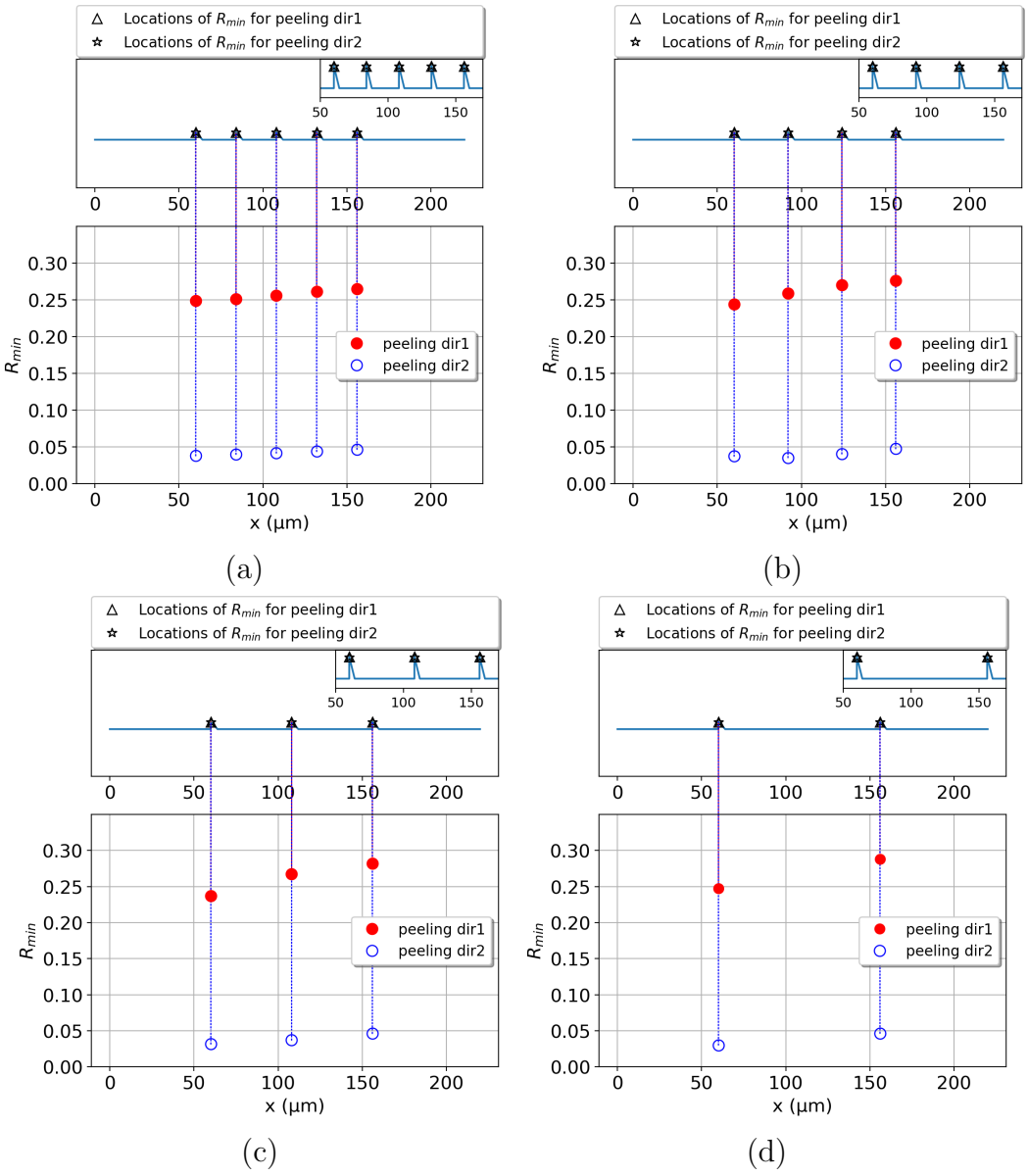

Figure 6.10: R_{min} and the corresponding locations on the interface for s/L = (a) 0.09, (b) 0.13, (c) 0.2 and (d) 0.42.

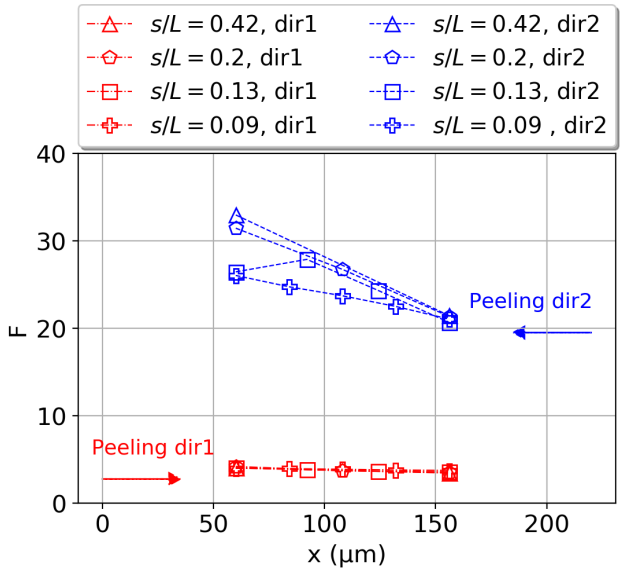

Figure 6.11: Adhesion enhancement factor F plotted against the apparent crack tip locations where R_{min} occurs.

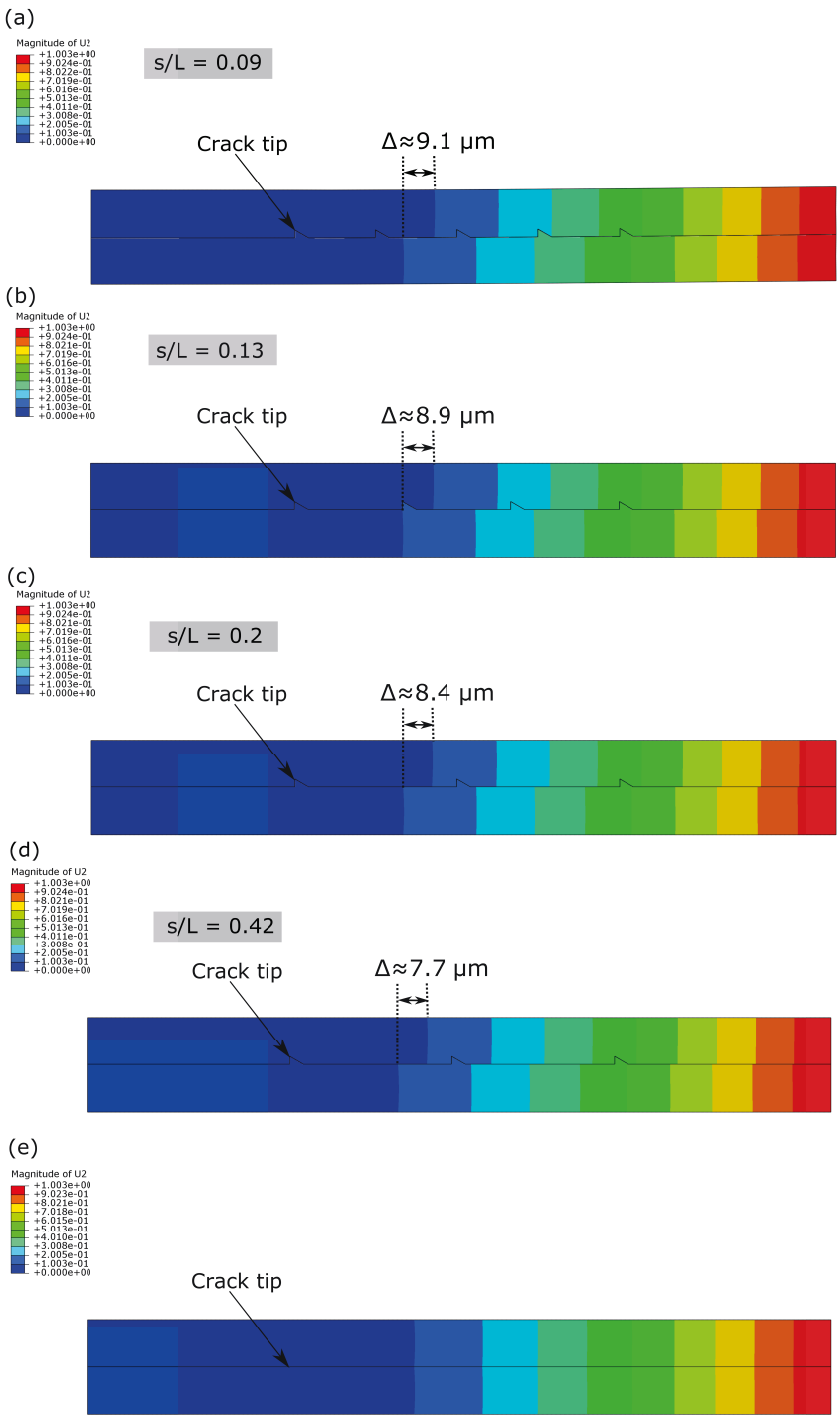

Figure 6.12: Contour plot for the magnitude of the displacement in the vertical direction when a crack propagates along peeling direction 2 to B_2 in the last period for (a) $s/L = 0.09$, (b) $s/L = 0.13$, (c) $s/L = 0.2$, and (d) $s/L = 0.42$. (e) shows the corresponding plot in a flat control with the same apparent crack length. The contours are plotted on the undeformed configuration of the samples.

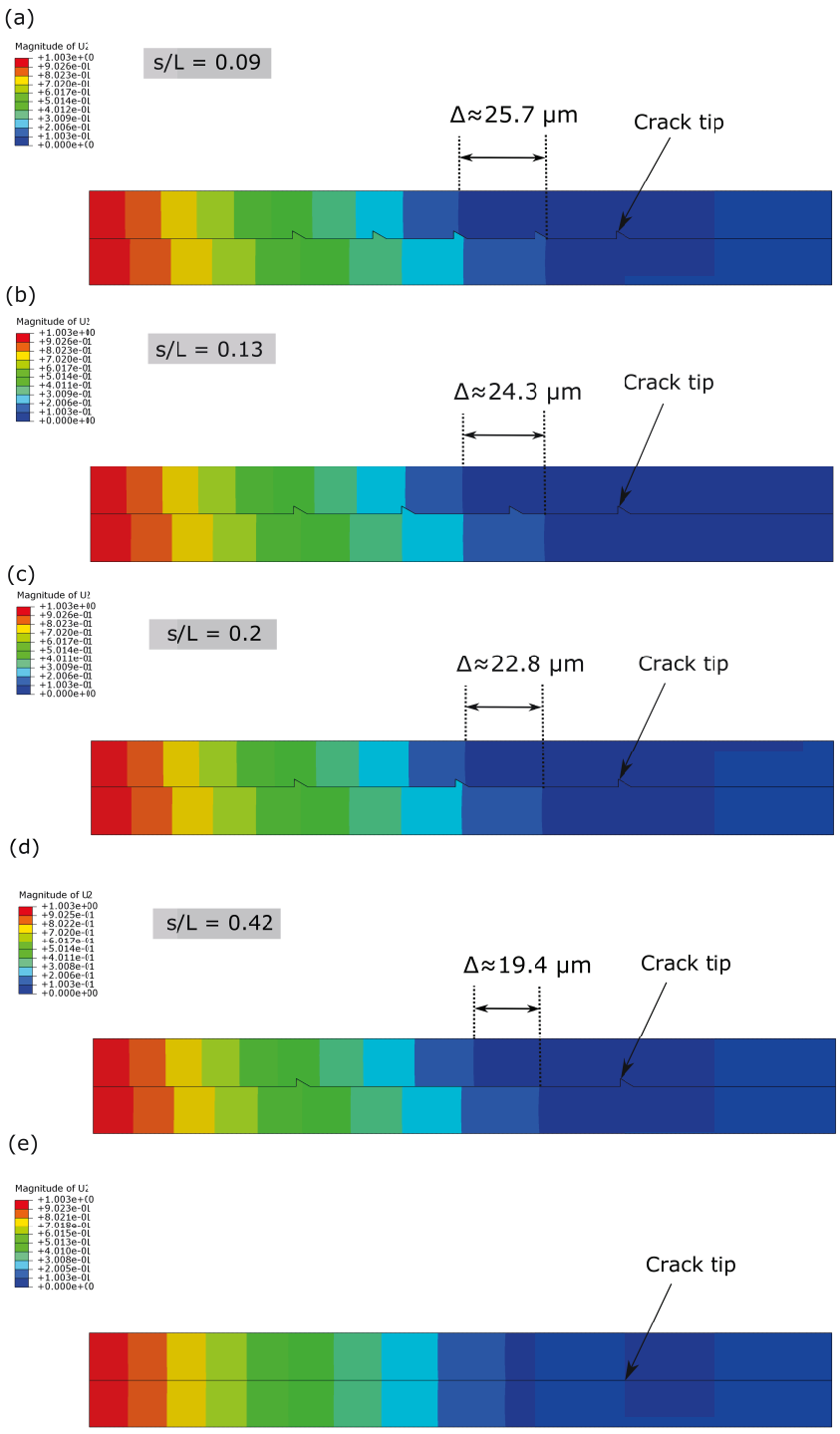

Figure 6.13: Contour plot for the magnitude of the displacement in the vertical direction when a crack propagates along peeling direction 1 to B_1 in the last period for (a) $s/L = 0.09$, (b) $s/L = 0.13$, (c) $s/L = 0.2$, and (d) $s/L = 0.42$. (e) shows the corresponding plot in a flat control with the same apparent crack length. The contours are plotted on the undeformed configuration of the samples.

6.4 Implications to Interface Design

Design principles to produce strong directional adhesion can be generated from a systematic parametric study. While the parameter space varies largely from one application to another, here we provide a demonstration of how to use FEA to make design suggestions. Triangular interface model as shown in Figure 5.1 is subjected to symmetric peeling from two opposite directions (Figure 5.2). Four H/l values (Table 6.1) and four θ values (Table 6.2) are used to create 16 cases simulated in FEA. For each case and along each direction, the adhesion enhancement factor F can vary with the apparent crack tip location where R_{min} occurs (see for example Figure 6.2), so the average value of F is calculated and denoted by $F_{avg,dir1}$ and $F_{avg,dir2}$ respectively for direction 1 and direction 2. The 16 values of $F_{avg,dir1}$ allow us to generate a contour plot, shown in Figure 6.14(a), with θ and H/l being the two variables. Liner interpolation was used to smoothen the contour. Similar contours are given in Figure 6.14(b) for $F_{avg,dir2}$ and in Figure 6.14(c) for the ratio $F_{avg,dir2}/F_{avg,dir1}$, the latter being an indicator for directional adhesion.

Upon examining Figure 6.14(a), $F_{avg,dir1}$ varies in the range of 2.8 to 5.2, and is found to be sensitive to θ but insensitive to H/l. In Figure 6.14(b), $F_{avg,dir2}$ varies in the range of 9.0 to 36.0, and is found to be sensitive to both H/l and θ, i.e., it increases with increasing θ or decreasing H/l. Besides, the dependence of $F_{avg,dir2}$ on H/l is stronger for taller teeth (larger θ). Because $F_{avg,dir1}$ and $F_{avg,dir2}$ show different sensitivities to θ and H/l, it is possible to tune directional adhesion by modulating the two parameters. As can be seen in Figure 6.14(c), a strong directional adhesion, i.e., large $F_{avg,dir2}/F_{avg,dir1}$ requires a combinations of higher θ and lower H/l. One can also change $F_{avg,dir2}$ while maintaining $F_{avg,dir1}$ by keeping θ constant and varying H/l.

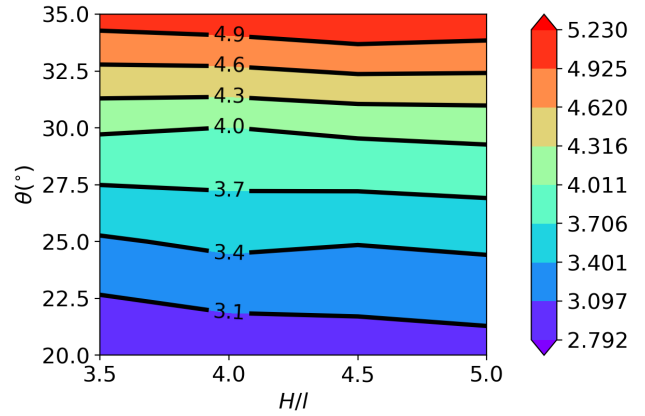

(a)

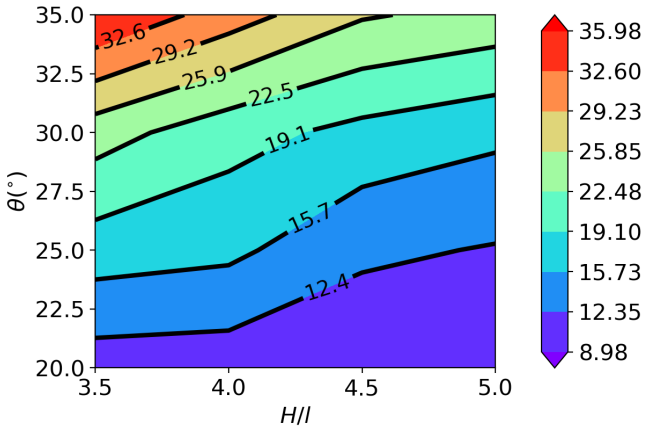

(b)

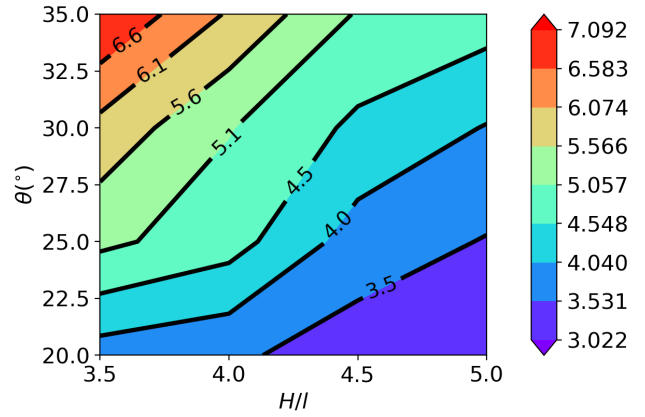

(c)

Figure 6.14: Contour plots for (a) the average value of adhesion enhancement factor along direction 1, $F_{avg,dir1}$ (b)corresponding value along direction 2, $F_{avg,dir2}$ and (c) $F_{avg,dir2}/F_{avg,dir1}$. Each contour plot is generated with θ and H/l being the two variables.

Chapter 7

Conclusions and Future Work

In this work, the adhesion in patterned complementary interfaces is studied by FEA. First, two types of symmetric interface, with rippled and rectangular patterns respectively, are examined under pulling for direct comparison with literatures. Our results showed good qualitative and quantitative agreement. In addition, the effect of loading conditions are investigated by considering asymmetric peeling of the same models. The application of asymmetric peeling condition is found to have profound effect on adhesion enhancement, such as changing the periodicity of $G_{pattern}/G_{flat}$ curve and the magnitude of the adhesion enhancement factor.

Next, the adhesion in an asymmetric interface containing right triangles is studied. Different crack separation directions are examined under three types of loading conditions, including symmetric peeling, asymmetric peeling and pulling. Enhanced adhesion is observed along all directions under all loading conditions. Under pulling, the adhesion enhancement does not depend on the direction of interface separation, and enhancement is mainly due to crack trapping near kinks. Observations for models under peeling are quite different. The adhesion enhancement factor obtained by propagating the crack along opposite directions can differ by as much as two orders of magnitude, suggesting strong directional adhesion. Local deformation of the triangular teeth on the interface is responsible for the remarkable directional adhesion under peeling which is significant along one direction but insignificant along the other. Such local deformation is also insignificant along both directions

under pulling.

Furthermore, the effects of three non-dimensional parameters on the adhesion enhancement are systematically investigated H/l, h/l and s/L, which respectively represents the relative size of the bulk sample with respect to the pattern, the influence of angle θ and the "density" of the triangles on the interface. Increases in H/l increase the volume fraction of the bulk sample such that the effect of the local deformation of the triangular teeth becomes weaker, leading to weaker directional adhesion. Increases in θ reduce the dominant contribution in crack propagation in directions 1 and 2, respectively by peeling the upper and lower parts. As a result, adhesion enhancement factors in both peeling directions and directional adhesion all increase with increasing θ. Decreases in s/L result in the deformation of lower part being promoted while that in the upper part being suppressed. Along peeling direction 2 this can lead to less "crack trapping" and promotion to crack propagation and consequently smaller adhesion enhancement. Along direction 1 the lost and promoted contributions to crack propagation due to the different deformations of the two parts compensate each other. Thus, the dependence of the adhesion enhancement factor on s/L is much smaller. Such parametric studies can be used to guide the design of interface with desired adhesion and directional adhesion.

Future work could include investigating triangles that do not have a 90° angle. Such patterns may reduce the probability of mismatching between the top and bottom surfaces in real applications. A cohesive zone model may be implemented on the interface to see the natural propagation of the crack, instead of mimicking the process by gradually releasing the tied nodes. The cohesive zone could also take into account the preexisting defects or cracks on interface due to mismatching of the two patterned surfaces. Finally, it would be interesting to fabricate such interfaces for practical use.

References

[1] G. de Mestral, "Velvet type fabric and method of producing the same," U.S. Patent 2 717 437, Sep. 13, 1955. 1

[2] A. L. Fry, "Repositionable pressure-sensitive adhesive sheet material," U.S. Patent 5 194 299, Mar. 16, 1993. 1

[3] S. Kim, M. Spenko, S. Trujillo, B. Heyneman, D. Santos, and M. R. Cutkosky, "Smooth vertical surface climbing with directional adhesion," *IEEE Transactions on Robotics*, vol. 24, no. 1, pp. 65–74, Feb. 2008. 1, 5

[4] S. Wang, M. Li, J. Wu, D.-H. Kim, N. Lu, Y. Su, Z. Kang, Y. Huang, and J. A. Rogers, "Mechanics of Epidermal Electronics," *Journal of Applied Mechanics*, vol. 79, no. 3, p. 031 022, 2012. DOI: 10.1115/1.4005963. 1

[5] R. C. Webb, A. P. Bonifas, A. Behnaz, Y. Zhang, K. J. Yu, H. Cheng, M. Shi, Z. Bian, Z. Liu, Y. S. Kim, W. H. Yeo, J. S. Park, J. Song, Y. Li, Y. Huang, A. M. Gorbach, and J. A. Rogers, "Ultrathin conformal devices for precise and continuous thermal characterization of human skin," *Nature Materials*, vol. 12, no. 10, pp. 938–944, 2013. 1

[6] A. Mahdavi, L. Ferreira, C. Sundback, J. W. Nichol, E. P. Chan, D. J. D. Carter, C. J. Bettinger, S. Patanavanich, L. Chignozha, E. Ben-Joseph, A. Galakatos, H. Pryor, I. Pomerantseva, P. T. Masiakos, W. Faquin, A. Zumbuehl, S. Hong, J. Borenstein, J. Vacanti, R. Langer, and J. M. Karp, "A biodegradable and biocompatible gecko-inspired tissue adhesive," *Proceedings of the National Academy of Sciences*, vol. 105, no. 7, pp. 2307–2312, 2008. 1

[7] H. Lee, B. P. Lee, and P. B. Messersmith, "A reversible wet/dry adhesive inspired by mussels and geckos," *Nature*, vol. 448, no. 7151, pp. 338–341, 2007. 1

[8] C. Creton, "P ressure-Sensitive Adhesives : An," no. June 2003, pp. 434–439, 2018. 1

[9] M. Sitti and R. S. Fearing, "Synthetic gecko foot-hair micro/nano-structures as dry adhesives," *Journal of Adhesion Science and Technology*, vol. 17, no. 8, pp. 1055–1073, 2003. 1, 2

[10] B. Aksak, M. P. Murphy, and M. Sitti, "Adhesion of biologically inspired vertical and angled polymer microfiber arrays," *Langmuir*, vol. 23, no. 6, pp. 3322–3332, 2007. 1, 2

[11] M. Lamblet, E. Verneuil, T. Vilmin, A. Buguin, P. Silberzan, and L. Léger, "Adhesion enhancement through micropatterning at polydimethylsiloxane-acrylic adhesive interfaces," *Langmuir*, vol. 23, no. 13, pp. 6966–6974, 2007. 1, 3

[12] C. Poulard, F. Restagno, R. Weil, and L. Léger, "Mechanical tuning of adhesion through micro-patterning of elastic surfaces," *Soft Matter*, vol. 7, no. 6, pp. 2543–2551, 2011. 1, 3

[13] V. Shilpi, K. Krishnacharya, Y. Shu, H. Chung-Yuen, and J. Anand, "Adhesion selectivity using rippled surfaces," *Advanced Functional Materials*, vol. 21, no. 3, pp. 547–555, 1, 4, 5, 22, 30, 33, 34, 36

[14] A. K. Singh, Y. Bai, N. Nadermann, A. Jagota, and C.-Y. Hui, "Adhesion of microchannel-based complementary surfaces," *Langmuir*, vol. 28, no. 9, pp. 4213–4222, 2012, PMID: 22316277. 1, 4, 5, 22, 30, 39, 40, 42

[15] K. Autumn, Y. A. Liang, S. T. Hsieh, W. Zesch, W. P. Chan, T. W. Kenny, R. Fearing, and R. J. Full, "Adhesive force of a single gecko foot-hair," *Nature*, vol. 405, no. 6787, pp. 681–685, 2000. 1

[16] K. Autumn, M. Sitti, Y. A. Liang, A. M. Peattie, W. R. Hansen, S. Sponberg, T. W. Kenny, R. Fearing, J. N. Israelachvili, and R. J. Full, "Evidence for van der waals adhesion in gecko setae," *Proceedings of the National Academy of Sciences*, vol. 99, no. 19, pp. 12 252–12 256, 2002. 1

[17] A. Jagota and S. J. Bennison, "Mechanics of adhesion through a fibrillar microstructure," *Integrative and Comparative Biology*, vol. 42, no. 6, pp. 1140–1145, 2002. 2

[18] C. Y. Hui, N. J. Glassmaker, T. Tang, and A. Jagota, "Design of biomimetic fibrillar interfaces: 2. mechanics of enhanced adhesion," *Journal of the Royal Society Interface*, vol. 1, no. 1, pp. 35–48, 2004. 2

[19] A. Majumder, A. Sharma, and A. Ghatak, "Bio-inspired adhesion and adhesives: Controlling adhesion by micro-nano structuring of soft surfaces," *Microfluidics and Microfabrication*, pp. 283–307, 2010. 2

[20] K. L. Johnson, K. Kendall, and A. D. Roberts, "Surface energy and the contact of elastic solids," *Proceedings of the Royal Society of London A: Mathematical, Physical and Engineering Sciences*, pp. 301–313, 1971. 2

[21] C. Greiner, A. D. Campo, and E. Arzt, "Adhesion of bioinspired micropatterned surfaces: Effects of pillar radius, aspect ratio, and preload," *Langmuir*, vol. 23, no. 7, pp. 3495–502, 2007. 2

[22] Y. Zhao, T. Tong, L. Delzeit, A. Kashani, M. Meyyappan, and A. Majumdar, "Interfacial energy and strength of multiwalled-carbon-nanotube-based dry adhesive," *Journal of Vacuum Science and Technology B*, vol. 24, no. 1, pp. 331–335, 2006. 2

[23] A. del Campo, C. Greiner, and E. Arzt, "Contact shape controls adhesion of bioinspired fibrillar surfaces," *Langmuir*, vol. 23, no. 20, pp. 10 235–43, 2007. 3

[24] N. J. Glassmaker, A. Jagota, C.-Y. Hui, W. L. Noderer, and M. K. Chaudhury, "Biologically inspired crack trapping for enhanced adhesion.," *Proceedings of the National Academy of Sciences of the United States of America*, vol. 104, no. 26, pp. 10 786–10 791, 2007. 3, 4, 16

[25] M. P. Murphy, B. Aksak, and M. Sitti, "Gecko-inspired directional and controllable adhesion," *Small*, vol. 5, no. 2, pp. 170–175, 2009. 5

[26] T. Anderson, *Fracture Mechanics: Fundamentals and Applications*. USA: Taylor and Francis Group, 2005. 7, 10, 12, 15

[27] "Vi. the phenomena of rupture and flow in solids," *Philosophical Transactions of the Royal Society of London A: Mathematical, Physical and Engineering Sciences*, vol. 221, no. 582-593, pp. 163–198, 1921. 11

[28] "Measurement of nonlinear mechanical properties of pdms elastomer," *Microelectronic Engineering*, vol. 88, no. 8, pp. 1982–1985, 2011, Proceedings of the 36th International Conference on Micro- and Nano-Engineering (MNE). 24

[29] D. Systèmes. (2014). Contact constraint enforcement methods in abaqus/standard. 25

Appendix A

MPC User Subroutine

```
      SUBROUTINE MPC(UE,A,JDOF,MDOF,N,JTYPE,X,U,UINIT,MAXDOF,LMPC,
     * KSTEP,KINC,TIME,NT,NF,TEMP,FIELD,LTRAN,TRAN)
C
      INCLUDE 'ABA_PARAM.INC'
C
      DIMENSION UE(MDOF),A(MDOF,MDOF,N),JDOF(MDOF,N),X(6,N),
     * U(MAXDOF,N),UINIT(MAXDOF,N),TIME(2),TEMP(NT,N),
     * FIELD(NF,NT,N),LTRAN(N),TRAN(3,3,N)
C
      IF (KSTEP.GE.(JTYPE+40)) THEN
        LMPC=0
      ELSE
        LMPC=1
      END IF
C
        UE(1) = U(1,2)
        UE(2) = U(2,2)

C
        A(1,1,1) =  1.
        A(2,2,1) =  1.
        A(1,1,2) = -1
        A(2,2,2) = -1.


C
        JDOF(1,1) = 1
        JDOF(2,1) = 2
        JDOF(1,2) = 1
        JDOF(2,2) = 2

C
      RETURN
      END
```

Appendix B

Effect of Applied Displacement on Adhesion Enhancement

Throughout the thesis, the constant displacement applied on the models to evaluate G is $\delta_0 = 1\mu m$. To examine the influence of other δ_0 values, simulations are performed for symmetric peeling of the model in Figure 5.1 with $\delta_0 = 2\mu m$. Results for the adhesion enhancement are compared in Figure B.1 for the two different δ_0 values. Clearly, for both peeling directions, the qualitative behaviours of F remain the same regardless of the δ_0 values.

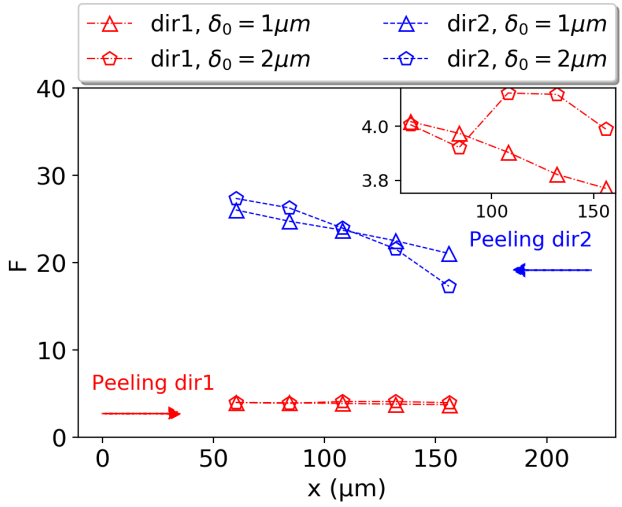

Figure B.1: Adhesion enhancement factors under symmetric peeling for different δ_0 values